2007-11-14

Numerical Study of Fully Developed Laminar and Turbulent Flow Through Microchannels with Longitudinal Microstructures

Kevin B. Jeffs
Brigham Young University - Provo

NUMERICAL STUDY OF FULLY DEVELOPED LAMINAR AND TURBULENT FLOW THROUGH MICROCHANNELS WITH LONGITUDINAL MICROSTRUCTURES

by

Kevin B. Jeffs

A thesis submitted to the faculty of

Brigham Young University

in partial fulfillment of the requirements for the degree of

Master of Science

Department of Mechanical Engineering

Brigham Young University

December 2007

BRIGHAM YOUNG UNIVERSITY

GRADUATE COMMITTEE APPROVAL

of a thesis submitted by

Kevin B. Jeffs

This thesis has been read by each member of the following graduate committee and by majority vote has been found to be satisfactory.

Date	R. Daniel Maynes
Date	Brent W. Webb
Date	Brian D. Jensen

BRIGHAM YOUNG UNIVERSITY

As chair of the candidate's graduate committee, I have read the thesis of Kevin B. Jeffs in its final form and have found that (1) its format, citations, and bibliographical style are consistent and acceptable and fulfill university and department style requirements; (2) its illustrative materials including figures, tables, and charts are in place; and (3) the final manuscript is satisfactory to the graduate committee and is ready for submission to the university library.

Date

R. Daniel Maynes
Chair, Graduate Committee

Accepted for the Department

Matthew R. Jones
Graduate Coordinator

Accepted for the College

Alan R. Parkinson
Dean, Ira A. Fulton College of Engineering and Technology

ABSTRACT

NUMERICAL STUDY OF FULLY DEVELOPED LAMINAR AND TURBULENT FLOW THROUGH MICROCHANNELS WITH LONGITUDINAL MICROSTRUCTURES

Kevin B. Jeffs

Department of Mechanical Engineering

Master of Science

Due to the increase of application in a number of emerging technologies, a growing amount of research has focused on the reduction of drag in microfluidic transport. A novel approach reported in the recent literature is to fabricate micro-ribs and cavities in the channel wall that are then treated with a hydrophobic coating. Such surfaces have been termed super- or ultrahydrophobic and the contact area between the flowing liquid and the solid wall is greatly reduced. Further, due to the scale of the micropatterned structures, the liquid is unable to wet the cavity and a liquid meniscus is formed between ribs. This creates a liquid-vapor interface at the cavity regions and renders surfaces with alternating regions of no-slip and of reduced shear on the microscale. This thesis reports the numerical study of hydrodynamically fully-developed laminar and turbulent flows through a parallel plate channel with walls exhibiting micro-

ribs and cavities oriented parallel to the flow direction, where fully developed turbulent flow is considered in a time-averaged sense. Three laminar flow models are implemented to investigate the liquid-vapor interface and to account for the effects of the vapor motion in the cavity regions. For each of the laminar flow models, the liquid-vapor interface was idealized as a flat interface. As a benchmark for following laminar flow models, the first model considers the case of a vanishing shear stress at the interface between the liquid and vapor domains. Effects of the vapor motion in the cavity are then accounted for in a one-dimensional cavity model where the vapor velocity is considered to be dependent on the wall normal coordinate only, followed by a two-dimensional cavity model that accounts for the vapor velocity's dependence on the transverse coordinate as well. The vapor cavity is modeled analytically and is coupled to the liquid domain by equating the fluid velocities and shear stresses at the liquid-vapor interface. In the turbulent flow model the liquid-vapor interface is idealized as a flat interface with a zero shear stress boundary condition. In general the numerical predictions show a reduction in the total frictional resistance as the cavity width is increased relative to the channel width, the channel height-to-width aspect ratio is decreased, and the vapor cavity depth is increased. The frictional resistance is also reduced with increased Reynolds number in the turbulent flow case. In the range of parameters examined for each fluid flow regime, reductions in drag as high as 91% and 90% are reported for the laminar flow and turbulent flow models, respectively. Under similar conditions however, the turbulent flow results indicate a greater reduction in flow resistance than for the laminar flow scenario. Based on an analysis of the obtained data, analytical expressions are proposed for both laminar and turbulent flow which facilitates the prediction of the frictional resistance.

ACKNOWLEDGMENTS

To my wife Tera, who has been a constant support and strength through all of life's adventures. Thanks also to Professor Maynes and Professor Webb who have given me much assistance and guidance throughout my educational pursuits.

TABLE OF CONTENTS

LIST OF TABLES

LIST OF FIGURES

1 Introduction

In fluid dynamic applications drag reduction is often a primary objective and concern. Even a small reduction in the viscous drag can have significant benefits, such as increasing performance and reducing operation costs. In some applications, drag reduction may even facilitate advancements in technology. Such is the case as advancing technologies look to utilize fluid motion on the microscale. Application such as "Lab on a Chip" or the use of microscaled heat exchangers, etc. [1-2] could be facilitated by implementing a method of reducing the significant friction resistance associated with microscale fluid flow. Although the topic discussed has application in both internal and external flow scenarios, the focus of the current study is on an internal flow application. Therefore, further discussion will focus primarily on the limiting case of confined flows.

1.1 Internal Flow

In confined flow applications the pressure required to induce fluid motion is inversely proportional to the diameter raised to the third or forth power, depending on the geometry. For a channel hydraulic diameter of order microns, this driving pressure can becomes excessive, making it very difficult to develop and produce such micro-fluidic devices [3-8]. If one could reduce the resistance exerted against the fluid at the solid boundary, a decrease in the required driving pressure could be obtained. The total

frictional resistance is equivalent to the integral of the product of the liquid-solid contact area and the local shear stress exerted by the solid boundary on the fluid. Further, the local shear stress is the product of the local viscosity and the velocity gradient of the fluid at the boundary. If one could influence one or more of these factors that contribute to the total frictional resistance (the liquid-solid contact area, the local viscosity, and/or the velocity gradient), a significant reduction in the drag and thus the driving pressure could be obtained. In recent literature a method of reducing the drag has been presented that successfully minimizes the liquid-solid contact area at the boundaries, thus achieving significant drag reduction in microfluidic flows. This method is described in detail in the following section.

1.2 Ultrahydrophobic Surfaces

A novel approach to eliminating frictional resistance reported in the recent literature looks to utilize the same principle that causes water droplets to simply roll off a lotus leaf and inhibits them from 'wetting' the surface of the leaf. This is done by fabricating micro-structures on the walls of a confined liquid flow.

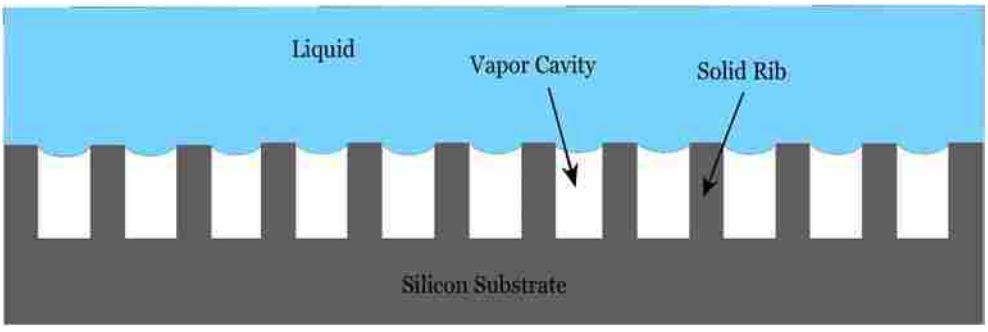

Figure 1-1 Schematic of alternating ribs and cavities

These structured surfaces consist of evenly spaced features, such as micro-ribs or posts, which are separated by cavity regions and are treated with a hydrophobic coating, see Figure 1-1. The hydrophobic coating alters the surface chemistry of the solid boundary and reduces the ability of the liquid water to 'wet' the surface. The degree to which a liquid 'wets' a surface is measured by the contact angle of a discrete liquid droplet when placed on a solid surface as shown in Figure 1-2, where θ is represents the contact angle.

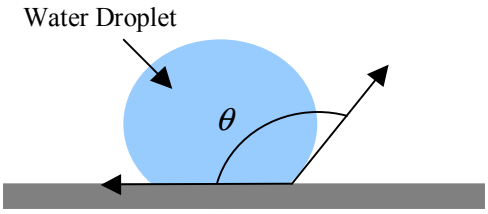

Figure 1-2 Illustration of the contact angle for a discrete water droplet

The hydrophobic coating attempts to repel the liquid and causes the contact angle of a water droplet to increase. With an increased contact angle the contact area between the liquid droplet and the solid is decreased and thus the water droplet is less inhibited in its movement across the surface. Further, the hydrophobic coating prevents the liquid from penetrating the cavity regions as long as the structures are spaced close enough together. Penetration of the liquid into the cavity is dependent on what is known as the Laplace pressure and is defined as

$$P_L = \frac{4\sigma\cos(\pi-\theta)}{w_c} \qquad \textbf{(1-1)}$$

where σ is the surface tension of the liquid, and w_c distance between the micro-structures. Calculating Equation 1-1 for a given surface feature configuration provides a maximum allowable pressure difference between the liquid and the vapor that cannot be exceeded without the liquid entering the cavity. Examination of this expression shows that as the spacing between structures increases, the pressure difference required for the liquid to penetrate the cavities decreases. Therefore a larger cavity width will wet at a much smaller pressure difference. In addition to the liquid being unable to wet the inside of the cavity, the surface tension of the liquid causes a meniscus to be formed suspended between the micro-features as illustrated in Figure 1-1. In this manner, the surface contact area between the flowing liquid and the solid wall is significantly reduced.

As long as the pressure difference between the liquid and the vapor in the cavities remains sufficiently low, this effect is maintained and the typical liquid-solid boundary is replaced above the cavity with a liquid-vapor interface. Further, at the liquid-vapor interface the resistance to liquid motion is much smaller than that existing at the liquid-solid interface due to the much smaller viscosity of the vapor. The result is walls with alternating no-slip and nearly shear-free regions on the micro-scale. Such surfaces are commonly referred to in the literature as super- or ultrahydrophobic. Figure 1-3 is an image of an ultrahydrophobic surface taken with an electron scanning microscope by Woolford et al. [30]. The presented surface consists of alternating ribs and cavities and has been cut to better illustrate the geometry of the structures, since the cavity regions are typically open only at their upper boundary. The micro-structures on this surface were cut into the silicon substrate by Deep Reactive Ion Etching (DRIE). After fabrication the surfaces were spin-coated with a mixture of PEL1604A and MQ000 FluorPEL

hydrophobic solutions produced by Cynotonix. In this specific example the cavity is approximately 20 μm deep and 30 μm wide, and the ribs are 10 μm wide. Ultrahydophobic surfaces such as this one have been reported in recent literature to significantly reduce the drag.

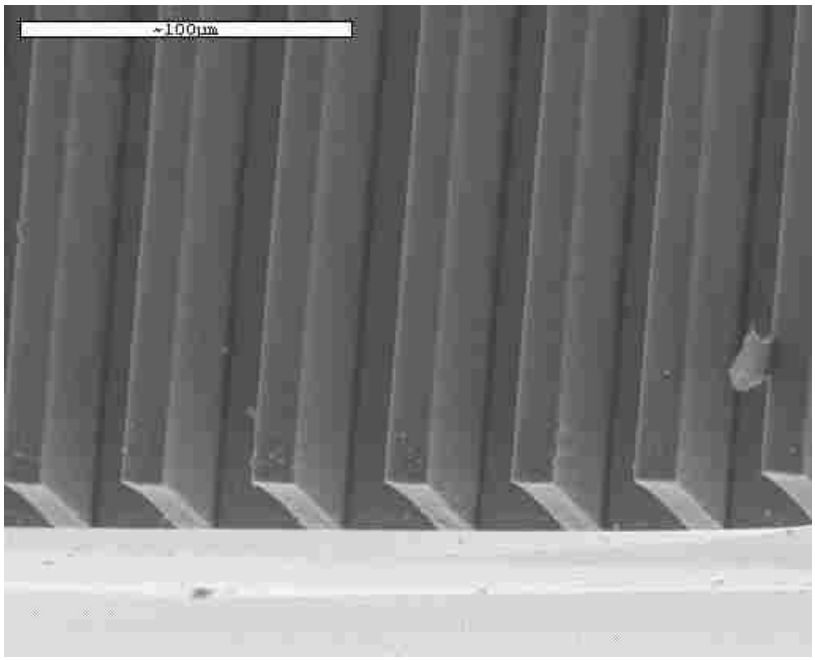

Figure 1-3 Electron scanning microscope image of a ultrahydrophobic surface

The focus of the presented work is to examine through numerical modeling the physics of fully-developed laminar and turbulent flow through microchannels with ultrahydrophobic walls. The ultrahydrophobic walls studied consist of alternating, rectangular ribs and cavities as illustrated in Figure 1-3, with the liquid flowing parallel to the structures. The potential reduction in the total frictional resistance is predicted as a function of the cavity geometry and the channel dimensions, and compared to classical

no-slip channel flow solutions. Further, the effect of the ultrahydrophobic surfaces on the liquid velocity and shear stress in the near wall region is also examined.

1.3 Division and Topics of the Remaining Chapters

In the proceeding chapter a detailed review of the previous research is presented. Chapter 2 presents a detailed literature review for three different areas of work that are relevant to the current study of ultrahydrophobic surfaces: discrete liquid droplets, fully-developed laminar flow, and finally turbulent flow over ultrahydrophobic surfaces. Chapter 3 provides a full description and breakdown of the developed analytical expressions and the numerical models used in the current study. The computational domain is introduced and the boundary conditions and the varied relevant dimensionless parameters are defined. Additionally, details of how the three laminar flow models and the turbulent flow model were conducted are presented. Contained in Chapter 4 are the results to the three laminar flow models in addition to the parametric studies associated with each model. Results are shown to illustrate the potential reduction in the total friction resistance and its dependence on the relevant dimensionless parameters. Results are also presented to illustrate the effect of ultrahydrophobic surfaces on the flow dynamics, particularly in the near wall region. Chapter 5 continues with a presentation of the turbulent flow model predictions. Results are shown to quantify the potential reduction of frictional drag in the turbulent flow regime. An examination of the turbulent liquid flow dynamics near the ultrahydrophobic surface is also presented and discussed. The thesis then closes with Chapter 6, which consists of a summary of the important results and the conclusions drawn from the entire study.

2 Previous Work

An increasing amount of research has been conducted to explore the physics and the potential reduction in frictional resistance associated with the application of ultrahydrophobic surfaces. Previous research ranges from droplet motion on such surfaces to continuous laminar flow through micro-channels; and it has recently extended to the turbulent flow regime. These previous investigations have shown that significant reductions in the measured flow resistance are possible and demonstrate a potential breakthrough for the application of microfluidic technologies. This chapter will examine the relevant contributions that have recently been made in the study of ultrahydrophobic surfaces.

2.1 Droplets

Several researchers have investigated the dynamics of discrete liquid droplets on ultrahydrophobic surfaces [9-16]. In these studies, the droplet's contact angle is determined when placed on an ultrahydrophobic surface and is compared to the measured contact angle when placed on a non-treated surface. The contact angle is measured as shown in Figure 1-2 and is a direct indication of the degree of the hydrophobic or hydrophilic characteristics of the surface. Typical hydrophilic surfaces exhibit water droplet contact angles of approximately 10-30°. Onda et al. [9] measured contact angles

of discrete water droplets on a fractal surface. A fractal surface is a surface that has been treated so that a random degree of surface roughness is formed. For surfaces where a hydrophobic material was used to create the fractal surface, contact angles as large as 174° are reported. Chen et al. [10] reports contact angles for discrete water droplets measured on ultrahydrophobic surfaces consisting of various micro-post configurations and hydrophobic treatments. Contact angles ranging from 140° to 177° were measured.

Water droplet research has also extended to measuring the enhanced droplet motion on ultrahydrophobic surfaces. Miwa et al. [11] conducted a study where the water droplet contact angle and sliding angle were measured using ultrahydrophobic surfaces with varying degrees of non-uniform surface roughness. The sliding angle was measured by placing a discrete water droplet of a specified volume on an ultrahydrophobic surface and measuring the angle at which droplet motion is induced. Therefore a low sliding angle would represent low frictional resistance. Results indicate that surface structures that are able to trap the air produce lower sliding angles. Similar studies have also been conducted with uniformly structured ultrahydrophobic surfaces. In a study performed by Kim et al. [12] the contact angle and the reduction of flow resistance is measured for discrete water droplets on flat and inclined ultrahydrophobic surfaces. Several different surface configurations were used; flat surface, non-structured surface, surfaces with rectangular micro-ribs oriented both parallel and transverse to droplet motion, surfaces with micro-posts, and finally ones with what is termed as nano-posts. Contact angles were measured on each surface to serve as a reference and are reported to be as high as 175° for the nano-post configuration. The reduction in the flow resistance associated with each microstructure configuration was quantified by measuring

the droplet sliding angle on the structured surface and comparing it to the measured sliding angle when placed on the smooth, non-structured surface. This was done both with open surfaces and confined surfaces where the droplet was placed into a microchannel consisting of two ultrahydrophobic surfaces spaced 1μm apart. Flow resistance is reported to have been reduced by over 99% for the open surface case and over 95% for the microchannel cases.

An additional study performed by Yoshimitsu et al. [13] (a continuation of the Miwa et al. report) looked to examine the dependence on surface structure with sliding behavior. In this study various ultrahydrophobic surfaces were prepared with uniform micro-rib and post structures and were used to examine the sliding behavior of discrete water droplets. It is reported in this study that the hydrophobic tendencies of the surface increased with increased post height. It was also shown that for water droplet motion it is more important to design a surface where the liquid droplet is continuously in contact with the solid structure than to simply increase the spacing between structures. This same conclusion is made in a study performed by Oner et al. [14], where water droplet motion was measured on ultrahydrophobic surfaces consisting of micro-posts with various cross sectional shapes.

Although these studies have provided an understanding of the effect ultrahydrophobic surfaces have on discrete liquid droplets, they do little to indicate the potential reduction in frictional resistance that such surfaces could provide in continuous fluid flow applications.

2.2 Laminar Flow

An increasing amount of research has been conducted to quantify the reduction in drag in pipes and channels with ultrahydrophobic walls for a continuous, steady, laminar flow [19-35]. Watanabe et al. [20] examined flow through a macro-scale pipe (D = 16 mm) with non-uniform rough walls which were treated with a hydrophobic coating. Drag reductions of up to 14% were measured when compared to the case where there was no hydrophobic coating and the water was allowed to wet the pipe wall. In a study conducted by Yong-Sheng et al. [21], the drag reducing effect of hydrophobic materials is explored by measuring the laminar boundary layer flow over flat plates. Plates with different wetting and roughness properties were explored. It was observed that the hydrophobic properties of the surfaces could be attributed to the existence of attached air bubbles that did not appear in flows over hydrophilic surfaces. The conclusion is made that the drag reduction over hydrophobic surfaces is due to the apparent slip of the liquid as it flows over the bubbles.

Ou et al. [22] conducted experiments in which the pressure drop was measured as a function of flow rate through a rectangular channel flow with hydraulic diameters ranging from 152 to 508 μm, with a single ultrahydrophobic surface. Surfaces that exhibited both micro-rib and post configurations were tested. When compared to classical laminar channel flow, pressure drop reductions as high as 40% were observed. In a later publication, Ou et al. [23] reported PIV measurements for a micro-scale channel flow with ultrahydrophobic surfaces consisting of micro-ribs oriented longitudinally to the streamwise direction. The PIV data clearly illustrate that the regions of reduced shear at the liquid-vapor interface are responsible for the measured reduction in pressure drop,

revealing an enhanced liquid velocity at the liquid-vapor interface. In a more recent publication by Chang-Hwan et al. [24], a study of laminar flow through a 'nanograted' ultrahydrophobic microchannel is presented. What they term as 'nanograted' is essentially micro-ribs that are brought to a point at the liquid-solid boundary. In this study, the structures were oriented both longitudinally and transversely to the fluid flow direction. The results show that the slip length increases as the micro-structure spacing increases and that the reduction in pressure drop decreases as the channel height is increased. Further, the observed flow enhancement was found to be more significant for the longitudinally oriented 'nanograte.'

An analytical study was performed by Philip [25] for creeping viscous flow through a two dimensional channel with surfaces exhibiting alternating section of no-slip and no-shear boundary conditions. One case consisted of alternating strips (which could be represented as rib and cavity microstructures on an ultrahydrophobic surface) oriented parallel to the flow direction. This work demonstrates an increase in the effective slip-length with increasing relative cavity width. The effective slip-length refers to the apparent macro-scale slip that exists at the surface and is defined as the wall-normal distance where the streamwise velocity would vanish based on the gradient of the local velocity distribution. Lauga and Stone [26] analytically explored circular pipe flow with alternating regions of no-slip and no-shear, oriented both longitudinal and transverse to the flow direction, with similar results to those of Philip. The analysis shows a decrease in the overall flow resistance in both rib orientations, although it was found to be greater for the longitudinally oriented ribs. Another analytical study conducted by Sbragaglia et al. [27] examines the effects of the liquid meniscus that is formed in between the

rectangular microstructures of an ultrahydrophobic surface. For this study the rectangular microstructures were oriented parallel to the flow direction. It is shown that the flow rate is increased as the meniscus expands into the cavity region while the slip length is decreased.

Significant flow enhancement is reported in a numerical study performed by Salamon et al. [28] for three-dimensional fluid flow through microchannels with ultrahydrophobic walls. In this study a micropost configuration was used in the construction of the ultrahydrophobic surface. The reduction in frictional drag is quantified by calculating the flow enhancement, which in this study is defined as the percent difference between the flow rate for a no-slip channel and the flow rate for the ultrahydrophobic channel for the same pressure drop. The flow enhancement was observed to increase when the relative cavity size was increased, either by increasing the post spacing or decreasing the post size. Flow enhancements as high as 175% are reported for a no-shear to no-slip ratio of 98%. Although not identified, the researchers recognize that another parameter is required in addition to the no-shear to no-slip ratio to completely illustrate the flow enhancement dependency on the surface configuration. Davies et al. [29] conducted a numerical study for non-creeping channel flow with rectangular ribs and cavities oriented perpendicular to the streamwise direction. Two models for the vapor cavity where implemented; these include a zero shear stress approximation at the liquid-vapor interface, and a coupled cavity model where the liquid and vapor velocity and shear stress are matched at the liquid-vapor interface. This study also reports significant reduction in the frictional resistance. This reduction was found to increase with increased cavity-to-rib length ratio and for decreased hydraulic diameters.

Further, the cavity depth was observed to have a significant influence on the predicted frictional resistance. This dependence on the cavity depth was seen to vanish once the cavity depth was increased to more than 25% of its width. Results also show that the slip length and the predicted reduction in frictional resistance exhibit a dependence on the Reynolds number.

Predictions obtained in the current work for laminar flow show similar trends to those reported in the previous work reported above. Further discussion of the results will be presented in later chapters.

2.3 Turbulent Flow

All of the previous work focusing on the laminar flow regime has shown that significant reductions in the frictional resistance are possible for microscale channel and pipe flows with ultrahydrophobic walls. A minimal amount of research has been conducted on turbulent flow over hydrophobic surfaces without microstructures [43-45]. Min et al. [43] performed a direct numerical simulation of a turbulent channel flow with hydrophobic walls. The hydrophobic condition at the walls was modeled with a slip condition where the slip length was specified. In this study the research examined three different cases: streamwise slip, spanwise slip, and a combination of both streamwise and spanwise slip. Results show that streamwise slip does contribute to frictional drag reduction; however, only for slip lengths higher than 0.2 were the reductions noticeable. It is also concluded that the reduction in drag is a direct effect of the slip velocity at the surface. More recently, Fukagata et al. [44] conducted an analytical analysis based on the results of Min et al. for hydrophobic walls. The focus of this study was to present a

theoretical prediction of the drag reduction rate achieved with the use of a slip boundary condition at the surface in the same three slip orientations presented by Min et al. The resulting expressions relate the drag reduction and the slip length, and are shown to match the Min data well.

Beyond the mentioned studies of turbulent flow over hydrophobic surfaces, very little attention has been given to the characterization of frictional drag reduction for the turbulent flow regime in ultrahydrophobic channels. Research conducted by Henoch et al. [45] has observed laminar to turbulent flow transition in a macroscale water tunnel with a single ultrahydrophobic surface. In their work two surface pattern configurations were used for their ultrahydrophobic test surface; these patterns include what has been termed 'nanograss' and 'nanobricks.' Although reference is made to further research that will more fully examine the effect of ultrahydrophobic surface on turbulent flow structures, a reduction in the frictional drag is reported to have been observed but is not quantified.

At this point in time no further research has been reported in the literature for turbulent flow through ultrahydrophobic surfaced channels. The current work looks to rectify this gap in the study of microfluidic drag reduction.

2.4 Contribution of Current Work

In light of the current available research it has become apparent that there are still holes in the understanding of continuous fluid flow through ultrahydrophobic microchannels. In summary, very little has been done to examine the effects of the liquid meniscus that is formed between solid structures. Also, the effects of the air or vapor

motion in the cavity region as well as the cavity geometry have not been considered in any of the previous studies other than that presented by Davies et al. [29] for a transverse orientation of the ribs and cavities. And finally, very little has been done to extend the study of continuous flow through ultrahydrophobic microchannels in the turbulent flow regime.

The focus of the presented work is to examine the impact and physics of fully-developed laminar and turbulent flow through microchannels with ultrahydrophobic walls, where the fully developed turbulent flow is considered in a time-average sense. Several numerical models have been employed to characterize the reduction of frictional resistance for laminar and turbulent flow through a rectangular channel with ultrahydrophobic walls consisting of alternating micro-ribs and cavities oriented parallel to the streamwise direction. These models include a study of the liquid meniscus effect for continuous laminar flow, as well as coupled vapor cavity models where the full effects of the vapor cavity on the frictional drag are studied in detail. The reduction of the total frictional resistance is quantified as a function of specific dimensionless parameters that are based on the micro-structure geometry, and will be fully discussed in later chapters. Additionally, analytical expressions are also developed based on the physics observed from both the laminar and turbulent flow predictions which successfully predict the total frictional resistance as based on the relevant parameters.

3 Methodology

3.1 Laminar Flow Models

Consider continuous, steady, fully developed laminar flow through a rectangular microchannel with ultrahydrophobic top and bottom walls. The microstructures on the ultrahydrophobic surfaces consist of alternating rectangular ribs and cavities oriented longitudinal, or parallel to the streamwise direction. Referring to Figure 1-1 and Figure 1-3, the fluid flow direction is perpendicular to, or into the image. The working fluid in consideration is liquid water and the fluid properties are considered to be constant. The spacing between ribs is small enough so that the pressure difference between the liquid and the vapor does not exceed the Laplace pressure (Equation 1-1), and therefore the liquid does not enter the cavity regions. As the liquid passes over the structured surface, and is unable to 'wet' the cavity, a meniscus is formed and is suspended between the ribs. For the laminar flow models implemented in this study, the liquid-vapor interface at the cavity regions is considered in an ideal manner, as a flat interface. In actuality, this liquid meniscus continuously changes as the static pressure of the fluid diminishes in the flow direction. The influence of this meniscus was explored and will be addressed in more detail in a later chapter. Further, the microchannel is modeled as infinite parallel plates since the channel width is much larger than the channel height and the effects of the side

walls can be neglected. For the given scenario, the classical Navier-Stokes equations are implemented. For a two-dimensional, incompressible laminar flow with no body forces, the dimensional continuity equation and momentum equation in the streamwise direction (x-direction) can be written as follows.

$$\frac{\partial u_l}{\partial x} + \frac{\partial v_l}{\partial y} = 0 \tag{3-1}$$

$$\rho_l \left(\frac{\partial u_l}{\partial t} + u \frac{\partial u_l}{\partial x} + v \frac{\partial u_l}{\partial y} \right) = -\left(\frac{\partial P}{\partial x} \right)_l + \mu_l \left(\frac{\partial^2 u_l}{\partial x^2} + \frac{\partial^2 u_l}{\partial y^2} + \frac{\partial^2 u_l}{\partial z^2} \right) \tag{3-2}$$

In the above expression, u_l is the liquid streamwise velocity component, v_l is the wall-normal velocity component, ρ_l is the liquid density, μ_l is the liquid viscosity, P is the static pressure, t is the time dimension, x is the streamwise coordinate, and y is the wall-normal coordinate. It can be seen in Equations 3-1 and 3-2 that since the fluid flow is considered two-dimensional, the velocity component in the transverse direction is neglected. It is also assumed in the current study that the liquid flow is steady and fully-developed, allowing for further reduction by eliminating the unsteady term and the streamwise velocity gradients. Further, elimination of the streamwise velocity gradient in Equation 3-1 reveals that the wall-normal velocity must be a constant. Since $v = 0$ at the liquid-solid boundaries, it therefore must be zero everywhere and can also be removed from the governing equations. With these reductions and by moving the pressure gradient to the opposite side of the equality, Equation 3-2 can be written as follows.

$$\left(\frac{\partial P}{\partial x}\right)_l = \mu\left(\frac{\partial^2 u_l}{\partial y^2} + \frac{\partial^2 u_l}{\partial z^2}\right) \tag{3-3}$$

The above expression can be normalized by dividing the wall-normal and transverse coordinates by the hydraulic diameter, $Y = y/D_h$ and $Z = z/D_h$, respectively. The hydraulic diameter is defined as $D_h = 4A_c/P_w$ where A_c is the channel cross sectional area and P_w is the nominal liquid perimeter. For parallel-plate channel flow where the channel width goes to infinity, the hydraulic diameter can be reduced to $D_h = 4H$, where H is half the channel height. Normalization of the streamwise velocity is accomplished with the pressure gradient, liquid viscosity and the hydraulic diameter, $U_l = u_l\mu_l/\left(D_h^2\left(dP/dx\right)_l\right)$. Therefore the nondimensional x-momentum equation can be reduced to Poisson's equation as shown.

$$1 = \left(\frac{\partial^2 U_l}{\partial Y^2} + \frac{\partial^2 U_l}{\partial Z^2}\right) \tag{3-4}$$

In the above equation, U_l is the normalized x-velocity of the liquid, and Y and Z are the normalized wall-normal coordinate and the normalized transverse coordinate, respectively.

For the given scenario, a two-dimensional liquid computational domain can be confined to a small repeating section consisting of a single rib and cavity and limited to half the total channel height due to symmetry conditions, as shown in Figure 3-1. The nondimensional liquid domain extends from $0 \le Y \le H/D_h$, where $H/D_h = 1/4$, and from 0

$\leq Z \leq W_m$. W_m represents the nondimensional width of the repeating module, $W_m = W_c + W_r = w/D_h$, where w is the total dimensional width of the cavity and rib sections, $w = w_c + w_r$.

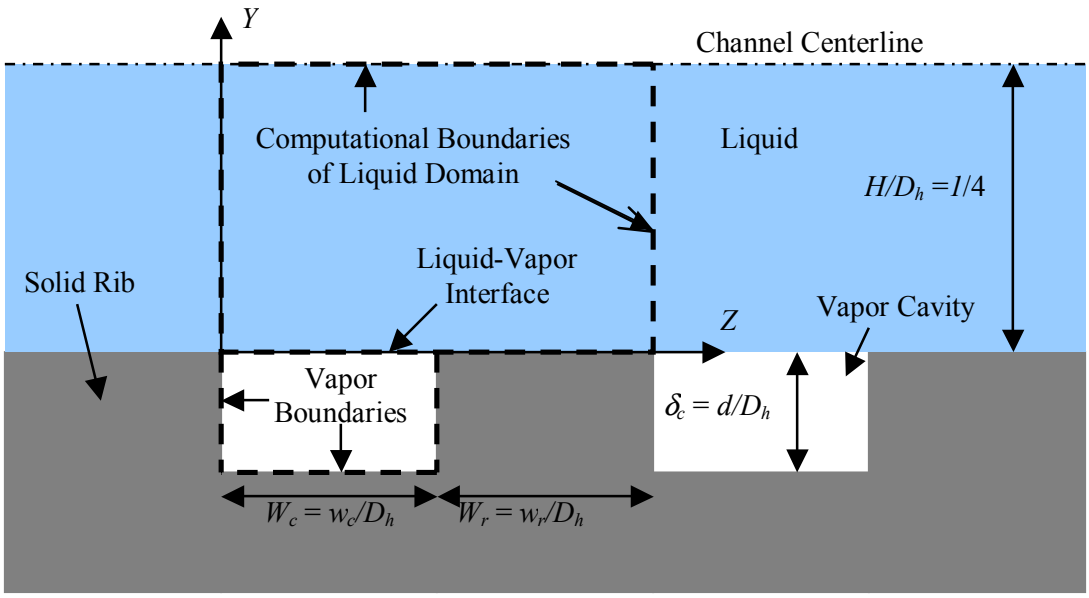

Figure 3-1 Schematic of computational domain

In solving Equation 3-4 for the liquid domain the boundary conditions were set as follows. At the channel centerline, Y = 1/4 and for $0 \leq Z \leq W_m$, a symmetry condition was applied, meaning the normal velocity gradient was set to zero, $\partial U/\partial Y = 0$. Since the computational domain consists of a repeating section, a periodic boundary condition was implemented at $Z = 0$ and $Z = W_m$ for $0 \leq Y \leq 1/4$, requiring the liquid velocity to be equal at identical vertical locations along both sides of the domain. Additionally, the classical no-slip boundary condition was enforced at the rib, for $W_c \leq Z \leq W_r$ at $Y = 0$. For the region above the cavity, $0 \leq Z \leq W_c$ and $Y = 0$, three different boundary

conditions, and thus three different models, where utilized in the current study. These boundary conditions can be classified into two different types. The first model makes the assumption that there is zero shear stress at the liquid-vapor interface located over the vapor cavity. The other two models, with increasing accuracy, look to model the influence of the vapor motion and the cavity geometry. Further discussion of the liquid-vapor interface boundary will be reserved for later sections where each model is explained in more detail.

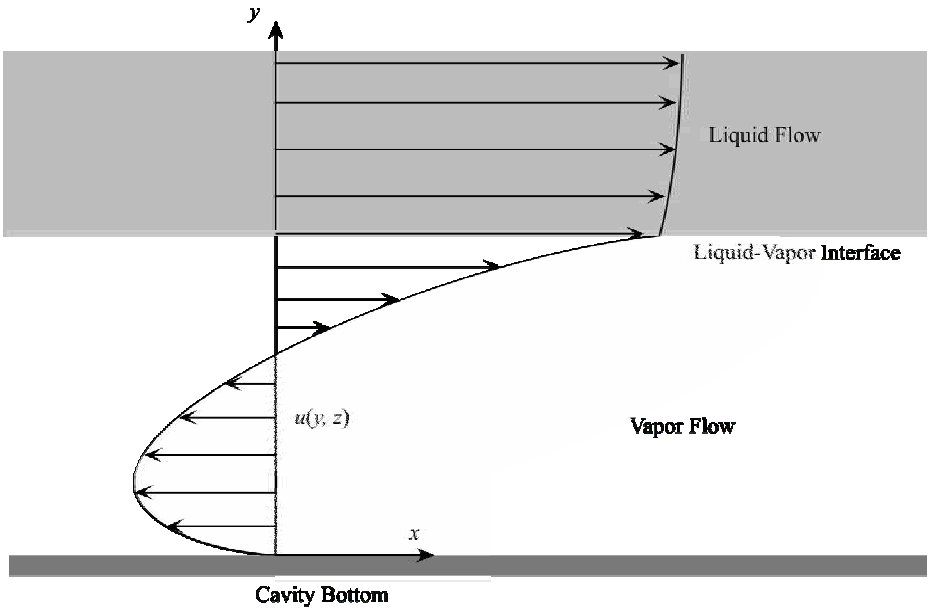

Figure 3-2 Illustration of the recirculation of the vapor flow in the cavity region that is induced by the interfacial liquid velocity

Although the zero shear stress model is a good initial approximation of the ultrahydrophobic surfaces, it is possible to create a model that more fully predicts the true physics of the flow. In reality the calculated frictional resistance is dependent upon the flow conditions and geometry of the vapor cavity. As the liquid passes over the cavity,

momentum is transferred to the vapor through viscous diffusion, thus inducing motion. In other words, the liquid will pull the vapor as it moves downstream as shown in Figure 3-2. Since the vapor cavity is presented to be capped at the entrance and the exit of the microchannel, a circulation cell is induced in the cavity. To facilitate the computation of the vapor domain, the vapor motion is assumed to be a steady, fully-developed laminar flow. By fully-developed it is to be understood that the cavity is much longer than the cavity height, allowing the end effects to be neglected. With negligible end effects, it can therefore be assumed that the two-dimensional vapor velocity profile is the same for the entire length of the channel.

The nondimensional vapor domain extends from $0 \le Y \le -\delta$ and from $0 \le Z \le W_c$ as illustrated in Figure 3-1. The nondimensional cavity depth is represented by $\delta = d/D_h$, where d is the dimensional cavity depth. The classical Navier-Stokes equations can also be applied to obtain a solution in the vapor domain. Likewise, the same simplifications used to reduce Equation 3-2 to Equation 3-4 can be applied to the vapor cavity. Therefore, the nondimensional momentum equation in the x-direction is also reduced to Poisson's equation as follows.

$$\left(\frac{(dP/dx)_v}{(dP/dx)_l}\right)\left(\frac{\mu_l}{\mu_v}\right) = \left(\frac{\partial^2 U_v}{\partial Y^2} + \frac{\partial^2 U_v}{\partial Z^2}\right) \qquad \textbf{(3-5)}$$

In the above expression, U_v is the dimensionless streamwise vapor velocity defined as $U_v = u_v \mu_l / \left(D_h^2 (dP/dx)_l\right)$, μ_v represents the vapor viscosity, and $(dP/dx)_v$ is the streamwise vapor pressure gradient. Due to the motion of the liquid-vapor interface

induced by the liquid motion, a pressure gradient develops in the vapor that acts to oppose the fluid flow at the interface. This pressure gradient is dependent on the magnitude of the spatially varying velocity at the liquid-vapor interface and cavity geometric parameters, as well as the viscosities of both the liquid and vapor phases. The streamwise pressure gradients in the liquid and vapor phases are unequal due to the existence of the liquid-vapor interface. The viscosity of the vapor was assumed to constant and be that of air at standard conditions in all laminar flow models implemented in the current study. The vapor cavity was modeled using two different methods, both of which will be examined in more detail in upcoming sections.

For the laminar flow models, three significant nondimensional parameters were varied. These consist of the relative module width, $W_m = w/D_h$, the cavity fraction, $F_c = w_c/w = W_c/W_m$, which provides the fraction of the channel wall that is occupied by the vapor cavity, and finally the relative cavity depth, $\delta_c = d/D_h$. The relative module width was varied from 0.1 - 1, and the cavity fraction from 0 - 0.97. The range of relative cavity depth values examined in the current study differs for each model and will be specified in future sections. The relative cavity depth is obviously not relevant to the initial zero shear stress model however, since the model consists only of the liquid domain.

Conducting an integral momentum analysis in the streamwise direction on the computational liquid domain shows that the induced pressure gradient must be balanced by the wall shear stress when the flow is fully developed. That is to say

$$(P_{inlet} - P_{outlet})A_c - \bar{\tau}_w A_s = \cancel{\frac{\partial}{\partial t}\int_{CV} \rho U dV} + \cancel{\int_{CS} \rho U (U \cdot \hat{n}) dA} \qquad \text{(3-6)}$$

0 (steady) 0 (fully-developed)

where $\bar{\tau}_w$ is the average wall shear stress, A_s and A_c are the channel wall surface area and the channel cross sectional area, respectively, and P_{inlet} and P_{outlet} are the static pressures at the channel inlet and outlet. The surface area is defined as the product of the channel width and the channel length, $A_s = WL$, and the cross-sectional area is the product of the channel height and width, $A_c = WH$. Substituting these definitions into Equation 3-6 and rearranging terms yields

$$\bar{\tau}_w = -\frac{\Delta P}{L} H \,. \qquad \text{(3-7)}$$

Recalling that the hydraulic diameter is defined as $D_h = 4H$, the average wall shear stress can then be expressed as follows.

$$\bar{\tau}_w = -\left(\frac{dP}{dx}\right)_l \left(\frac{D_h}{4}\right) \qquad \text{(3-8)}$$

The average normalized shear stress, defined as $\overline{T}_w = \bar{\tau}_w / \left(D_h (dP/dx)_l\right)$, is therefore equal to -1/4 for all the laminar flow models presented here.

To quantify the reduction of frictional resistance produced by using ultrahydrophobic walls, it is convenient to calculate the Darcy friction factor-Reynolds

number product, *fRe*, where the Reynolds number is based on the hydraulic diameter. One can then compare the predicted value to that calculated for a classical parallel plate channel flow, *fRe* = 96. Any reduction from this value, therefore, represents a reduction in the total frictional resistance. The Darcy friction factor can be expressed in the following manner.

$$f = \frac{2D_h}{\rho \bar{u}_l}\left(\frac{dP}{dx}\right)_l \tag{3-9}$$

Using Equation 3-8 to replace the pressure gradient in the above expression, and multiplying by the Reynolds number yields

$$f\,\mathrm{Re} = 8\frac{\overline{T}_w}{\overline{U}_l} \tag{3-10}$$

In this expression, $\overline{U}_l$ represents the average normalized liquid velocity. Further, since $\overline{T}_w = -1/4$ the friction factor-Reynolds number product can be calculated simply as $f\,\mathrm{Re} = 2/\overline{U}_l$ for each of the laminar flow models implemented in this study. This illustrates that the predicted reduction in the frictional resistance is a direct result of the enhanced liquid velocity induced by the regions of reduced shear stress.

As discussed previously, the no-slip condition is satisfied at the liquid-solid interface, however at the liquid-vapor interface a non-zero, spatially varying velocity exits. Therefore, on a macroscopic level the liquid exhibits a slip velocity at the channel

walls. Davies et al. [29] developed a relation between the slip length, λ, and the friction factor-Reynolds number product.

$$\frac{\lambda}{w} W_m = \frac{8}{f\,\mathrm{Re}} - \frac{1}{12} \tag{3-11}$$

This expression allows for the conversion from one measure to the other. Lauga and Stone [26] have analytically examined fully developed laminar flow through a parallel plate channel where $Re \rightarrow 0$ and $K_n \rightarrow 0$, with zero shear stress at the liquid-vapor interface. This study shows that the fluid slip can be expressed as follows.

$$\frac{\lambda}{w} = \frac{1}{\pi} \ln\left(\frac{1}{\cos(F_c \pi / 2)} \right) \tag{3-12}$$

By combining Equations 3-11 and 3-12 one can then develop an expression for *fRe* in terms of the relevant dimensionless parameters used in the presented study. Simplification yields the follow.

$$f\,\mathrm{Re}_{ZS} = \frac{8}{\left[\frac{1}{\pi} \ln\left(\frac{1}{\cos(F_c \pi / 2)} \right) W_m + \frac{1}{12} \right]} \tag{3-13}$$

The above expression indicates that the *fRe* predictions can be quantified by a single curve for the limited case where the vapor cavity is neglected and the liquid-vapor

interface is modeled as a zero shear stress boundary. As an exact solution, Equation 3-13 provides a benchmark for the laminar flow models.

3.1.1 Zero Shear Stress Model

The initial laminar flow model implemented in the current study is confined simply to the nondimensional liquid domain, as shown in Figure 3-1. The conditions at the boundaries of the liquid domain are maintained as defined in the previous section. At the channel centerline, $Y = 1/4$ and for $0 \leq Z \leq W_m$, a symmetry condition was applied, $\partial U/\partial Y = 0$. A periodic boundary condition was implemented at $Z = 0$ and $Z = W_m$ for $0 \leq Y \leq 1/4$, requiring the liquid velocity to be equal at identical locations along both sides of the domain. Additionally, the classical no-slip boundary condition was enforced at the rib, for $W_c \leq Z \leq W_r$ at $Y = 0$. For the region above the cavity, $0 \leq Z \leq W_c$ and $Y = 0$, where the liquid-vapor interface exists, a zero shear stress assumption is made. Since the vapor viscosity is much smaller than that of the liquid, it can be argued that the vapor exerts negligible resistance to the liquid motion. Although this assumption is recognized as an idealization of what is actually occurring physically, the model still provides a good estimate of the potential reduction of frictional resistance. Since an exact solution exists for this limiting case (Equation 3-13), the zero shear stress model becomes a benchmark and a validation for the numerical approach presented.

The liquid computational domain was discretized with node clustering at the regions where high velocity gradients are expected, primarily in the transverse direction at the rib edges were the boundary condition transitions to that of no-slip to no-shear, and in the wall normal direction near the liquid-vapor and liquid-solid interfaces. The

commercial software package Fluent™ was implemented to solve the governing equations. A heat transfer analogy was used to obtain a solution to the liquid domain since Fluent™ is not capable of solving the two-dimensional momentum equation for the scenario where the fluid streamwise direction is perpendicular to the two-dimensional plane. This solution approach was facilitated by the fact that the nondimensional momentum equation in the x-direction (Equation 3-4) is in the form of Poisson's equation, as stated in the previous section. Fluent™ was therefore set to solve a scalar diffusion equation with a single source and with boundary conditions consisting of a specified value of the scalar and its wall-normal gradient as opposed to those of the velocity and the shear stress, respectively. The wall-normal scalar gradient was set to zero at the channel centerline, and the scalar magnitudes were set to be equivalent at equal wall-normal positions on the periodic side boundaries. Further, the magnitude of the scalar was assigned to zero at the liquid-solid interface to model the classical no-slip condition at the rib, and a vanishing gradient was employed at the liquid-vapor interface to model the zero shear stress condition.

For a grid-independent solution, a grid of approximately 30,000 nodes was implemented. Additionally, each case was allowed to run until the nondimensional shear stress was within 0.01% of the value of -1/4 and the average nondimensional velocity had ceased to change by more than 0.005%. Predicted fRe values were calculated using Equation 3-10 and compared to the classical parallel plate value of 96 as well as to the exact solution, Equation 3-13.

3.1.2 Liquid Meniscus Study

In the laminar flow models, the liquid vapor interface is represented ideally as a flat interface between the ribs. In reality, as discussed previously, the liquid forms a meniscus suspended between the ribs which slightly penetrates the cavity region. A parametric study was conducted in conjunction to the zero shear stress model with the purpose of determining the significance of the meniscus shape at liquid-vapor interface. A two-dimensional liquid computational domain was created consisting of a meniscus at the cavity region as illustrated in Figure 3-3. In order to determine the influence of only the meniscus shape, the liquid-vapor boundary was modeled as having a zero shear stress. All other boundary conditions were maintained as defined for the laminar flow models. The relative meniscus depth, $\xi = d_m / D_h$, where d_m is the maximum dimensional meniscus depth, was varied within the range of 0.0-0.1. However, the relative module width was maintained at a value of 1.0 and the cavity fraction at a value of 0.87. It is important to note that the meniscus depth was arbitrarily assigned and not solved for.

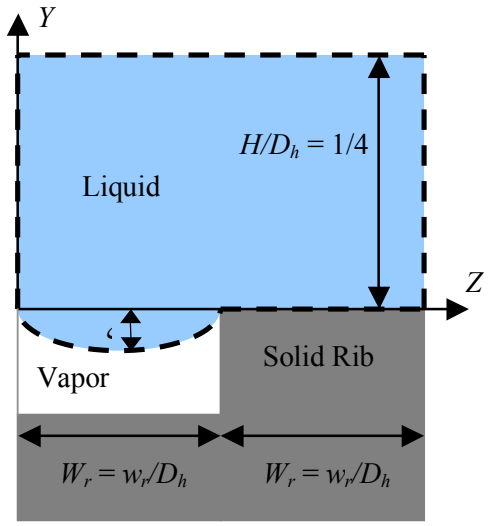

Figure 3-3 Computational domain implemented in the meniscus study

For a grid-independent solution, a grid of approximately 30,000 nodes was implemented. Convergence was monitored in similar manner as was done in the zero shear model with the exception that with the meniscus included, the average nondimensional shear stress is not equal to -1/4. This is a direct result of the increased surface area created by the inclusion of the meniscus. Each case, therefore, was allowed to run until the nondimensional shear and the average nondimensional velocity had ceased to change by more than 0.005%. Each case in the meniscus study was initialized using the solution obtained for the zero shear stress model for the same relative module width and cavity fraction values.

3.1.3 One-Dimensional Cavity Model

For the zero shear stress model the assumption was made that the vapor exerts a negligible amount of resistance to the liquid flow. In reality however, a finite friction exists since the fluids are of differing viscosities. Although this may be small in comparison to that experienced at the liquid-solid boundary, the purpose of the cavity models is to more closely represent the true physics of the flow by accounting for the influence of the vapor cavity. As with the other laminar flow models, at the channel centerline, $Y = 1/4$ and for $0 \le Z \le W_m$, a symmetry condition was applied, $\partial U/\partial Y = 0$, and a periodic boundary condition was implemented at $Z = 0$ and $Z = W_m$ for $0 \le Y \le 1/4$. Additionally, the classical no-slip boundary condition was enforced at the rib, for $W_c \le Z \le W_r$ at $Y = 0$ (see Figure 3-1). At the cavity, $0 \le Z \le W_c$ and $Y = 0$, the influence of the vapor is accounted for by using a one-dimensional cavity velocity model. In this model,

the assumption is made that the influence of the cavities side walls is negligible and that the vapor velocity in the cavity is only a function of the wall-normal coordinate (*y*-direction). This allows for the vapor cavity to be modeled as an infinitely wide, lid-driven cavity as shown in Figure 3-4.

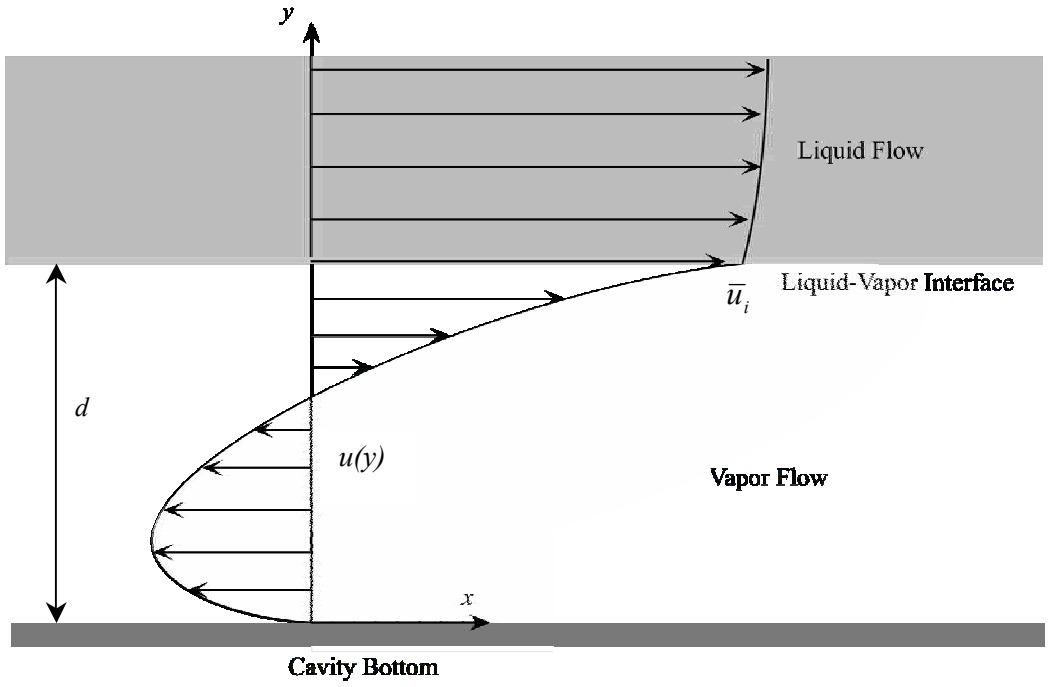

Figure 3-4 Schematic of the vapor cavity as a one-dimensional lid driven cavity

Applying Equation 3-3 to the one-dimensional lid-driven cavity one can obtain an expression for the vapor velocity as a function of the wall-normal coordinate. Eliminating the dependence on the transverse coordinate, Equation 3-3 is reduced to

$$\left(\frac{\partial P}{\partial x}\right)_v = \frac{\partial^2 u_v}{\partial y^2} \tag{3-14}$$

where u_v is the vapor velocity, y is the wall normal coordinate measured from the bottom surface of the vapor cavity, and $(dP/dx)_v$ is the streamwise vapor pressure gradient. Integrating Equation 3-14 twice and simplifying the resulting expression reveals an expression for the dimensional vapor velocity as a function of the wall normal coordinate.

$$u_v(y) = \frac{1}{2\mu_v}\left(\frac{dP}{dx}\right)_v \left(y^2 - yd\right) + \frac{\overline{u}_i}{d} y \tag{3-15}$$

In the equation above, d is the dimensional cavity depth and the interface velocity at the liquid-vapor interface is represented as $\overline{u}_i$ (see Figure 3-4). For the one-dimensional cavity model, the average interfacial velocity is assumed to be a constant value and is obtained by averaging the liquid velocity at the liquid-vapor interface in the transverse coordinate, for $0 \le Z \le W_c$ and $Y = 0$. Additionally, because of the convection cell in the vapor cavity, the average vapor velocity in the cavity must equal zero to satisfy conservation of mass, as shown in the following expression.

$$\overline{u} = \frac{1}{d}\int_0^d u_v(y)dy = 0 \tag{3-16}$$

The vapor pressure gradient can then be obtained by substituting Equation 3-15 into Equation 3-16 and integrating.

$$(dP/dx)_v = \frac{6\overline{u}_i\mu_v}{d^2} \tag{3-17}$$

Substitution of the vapor pressure gradient into Equation 3-15 and subsequent simplification provides an expression for the vapor velocity as a function of the wall-normal coordinate, the cavity depth, and the average interfacial velocity.

$$u_v(y) = \overline{u}_i\left(3\frac{y^2}{d^2} - 2\frac{y}{d}\right) \tag{3-18}$$

Using Equation 3-18, one can then solve for the dimensional shear stress at the liquid-vapor interface, $\overline{\tau}_c = \mu_v\left(du/dy\right)_{y=0} = 4\overline{u}_i\mu_v/d$. Normalization of the average interface shear stress yields

$$\overline{T}_c = 8\overline{U}_v\left(\frac{H}{d}\right)\left(\frac{\mu_v}{\mu_l}\right) = 2\overline{U}_l\left(\frac{1}{\delta_c}\right)\left(\frac{\mu_v}{\mu_l}\right) \tag{3-19}$$

where the nondimensional shear stress is defined as $T_c = \tau_c/\left(D_h\left(dP/dx\right)_l\right)$ and the nondimensional interface velocity as $\overline{U}_i = \overline{u}_i\mu_l/\left(D_h^2\left(dP/dx\right)_l\right)$. This simple analysis reveals that the shear stress at the interface is dependent on both the cavity depth and the viscosity ratio between the two fluids, as one would expect. This one-dimensional cavity model can then be coupled to the solution to the liquid domain by setting the normalized average vapor velocity and interface shear stress equal to that of the liquid. Thus the average normalized shear stress can be calculated using Equation 3-19 and be applied as the boundary condition at the liquid-vapor interface. This allows for a simple model that

will model to a first-order the impeding viscous resistance of the vapor against the liquid and for the depth of the cavity.

The one-dimensional cavity model was employed for the relative module widths values of W_m = 0.1 and 1.0 and for cavity fractions of F_c = 0.94 and 0.97. Additionally, the relative cavity depth (δ_c) was maintained at a value of 0.1 for each of the cases. A cavity depth study was then conducted where the relative cavity depth was varied from δ_c = 0.006-0.1, for W_m = 0.1 and 1, and F_c = 0.94 and 0.97.

The liquid computational domain was discretized with node clustering carried out in the same manner as for the zero shear stress model. Since this model considers the streamwise direction to be perpendicular to the two-dimensional liquid domain, the same scalar diffusion analogy solution technique used in Fluent™ for the zero shear stress model was employed for the one-dimensional cavity model. Further, all boundary conditions remain as defined for the zero shear stress model with the exception of the vapor cavity region, $0 \leq Z \leq W_c$ and $Y = 0$. As discussed in the previous paragraph, Equation 3-12 is used to calculate the interfacial shear stress, which is in turn applied as a specified wall shear stress boundary condition at the cavity region. Due to the fact that the interfacial shear stress and velocity are interdependent, this becomes a dynamic boundary condition. To accomplish this, a User Defined Function (UDF) was coded to supplement Fluent™ (see Appendix A for UDF code). Initially, a solution is obtained using Fluent™ for the liquid domain by using the initial zero shear stress approximation. Subsequently, the UDF uses the interfacial liquid velocity at the cavity to calculate the average shear stress at the interface. And finally, the calculated shear stress is applied to

the cavity region and replaces the previous shear stress value, and the liquid domain is recomputed based on the updated boundary condition.

For grid independent solutions, the same grid used in the zero shear stress model of approximately 30,000 nodes was implemented. Additionally, the identical convergence criteria were also found to be appropriate for the one-dimensional cavity model. Each case was allowed to run until the nondimensional shear stress was within 0.01% of the value of -1/4 and the average nondimensional velocity had ceased to change by more than 0.005%. Each one-dimensional cavity model case was initialized using the solution obtained for the zero shear stress model for the same relative module width and cavity fraction values.

3.1.4 Two-Dimensional Cavity Model

The application of the one-dimensional cavity model revealed that the vapor cavity has a significant influence on the total frictional resistance. For added rigor, a two-dimensional cavity model was implemented to account for velocity gradients in the transverse coordinate (z-direction) in addition to the wall normal coordinate (y-direction). As defined in the one-dimensional cavity model, it is assumed that the cavity end effects are negligible and the flow can be modeled as a steady, fully developed laminar flow. To obtain a solution for the vapor cavity, all of the conditions at the boundaries of the liquid domain are maintained as defined for the one-dimensional cavity model, except that of the cavity region, $0 \le Z \le W_c$ and $Y = 0$. At the channel centerline, $Y = 1/4$ and for $0 \le Z \le W_m$, a symmetry condition was applied, $\partial U/\partial Y = 0$, and a periodic boundary condition was implemented at $Z = 0$ and $Z = W_m$ for $0 \le Y \le 1/4$. Additionally, the classical no-slip

boundary condition was enforced at the rib, for $W_c \le Z \le W_r$ at $Y = 0$. To model the vapor cavity, Equation 3-5 was solved analytically using a separation of variable technique. No-slip boundary conditions were applied to the cavity walls, for $0 \le \hat{Y} \le -\delta_c$ at both $Z =$ 0 and W_c, and for $0 \le Z \le W_c$ at $\hat{Y} = 0$. Where $\hat{Y} = Y + \delta_c$ and is measured from the bottom of the vapor cavity ($Y = -\delta_c$), as shown in Figure 3-5. At the liquid-vapor interface, $0 \le Z \le W_c$ at $\hat{Y} = \delta_c$, the analytical vapor cavity solution is coupled to the liquid domain by equating the interfacial fluid velocities. In other words, the boundary condition is set as a spatially dependent velocity profile, $\overline{u}_i(Z)$.

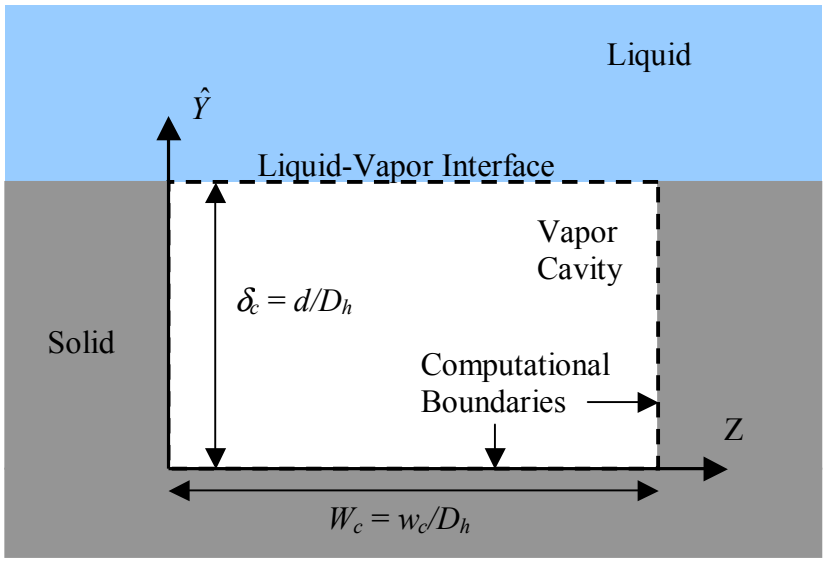

Figure 3-5 Vapor cavity computational domain for analytical solution to Equation 3-5

The analytical solution to Equation 3-5 is in the form of a two-dimensional velocity distribution for the cavity as a function of the unknown interface velocity, u_i, and the unknown vapor-liquid pressure ratio, $(dP/dx)_v/(dP/dx)_l$. In nondimensional form

the vapor velocity in the cavity is as follows. Refer to Appendix B for a more detailed derivation.

$$U_v\left(Z,\hat{Y}\right)=\frac{2}{W_c}\sum_{n=1}^{\infty}a_n\sin\left(n\pi Z/W_c\right)\sinh\left(n\pi\hat{Y}/W_c\right)-$$

$$\frac{4}{\pi^4}\frac{\mu_l}{\mu_v}\frac{\left(dP/dx\right)_v}{\left(dP/dx\right)_l}\sum_{n=1}^{\infty}\sum_{m=1}^{\infty}\frac{A_{nm}}{B_{nm}}\sin\left(n\pi Z/W_c\right)\sin\left(m\pi\hat{Y}/\delta_c\right) \quad \textbf{(3-20)}$$

The coefficients a_n, A_{nm}, and B_{nm} are defined as follows.

$$a_n=\frac{\int_0^{W_c}U_i\left(Z\right)\sin\left(n\pi Z/W_c\right)dz}{\sinh\left(n\pi\delta_c/W_c\right)} \quad \textbf{(3-21)}$$

$$A_{nm}=\frac{\left(\cos\left(n\pi\right)-1\right)\left(\cos\left(m\pi\right)-1\right)}{nm} \quad \textbf{(3-22)}$$

$$B_{nm}=\frac{n^2}{W_c^2}+\frac{m^2}{\delta_c^2} \quad \textbf{(3-23)}$$

As in the one-dimensional cavity model, the average velocity in the vapor cavity must be equal to zero in order to satisfy conservation of mass. One can then employ the same technique to solve for the unknown vapor-liquid pressure gradient ratio. The average velocity can be written as shown.

$$\overline{U}\left(Z,\hat{Y}\right)=\int_0^{W_c}\int_0^{\delta_c}U\left(Z,\hat{Y}\right)dZd\,\hat{Y} \tag{3-24}$$

Performing the integration and simplifying where appropriate yields the following expression for the pressure gradient ratio.

$$\frac{\left(dP/dx\right)_v}{\left(dP/dx\right)_l}=-\left(\frac{\pi^4}{2\delta_c}\frac{\mu_v}{\mu_l}\right)\Phi \tag{3-25}$$

In this relation, Φ represents

$$\Phi=\frac{\sum_{n=1}^{\infty}\frac{a_n}{n^2}\left(\cos\left(n\pi\right)-1\right)\left(\cosh\left(n\pi\delta_c/W_c\right)-1\right)}{\sum_{n=1}^{\infty}\sum_{m=1}^{\infty}\frac{A_{nm}^2}{B_{nm}}} \tag{3-26}$$

Substituting Equations 3-25 and 3-26 into Equation 3-20 the two-dimensional normalized vapor velocity becomes

$$U_v\left(Z,\hat{Y}\right)=\frac{2}{W_c}\sum_{n=1}^{\infty}a_n\sin\left(n\pi Z/W_c\right)\sinh\left(n\pi\hat{Y}/W_c\right)+$$

$$\frac{2\Phi}{\delta_c}\sum_{n=1}^{\infty}\sum_{m=1}^{\infty}\frac{A_{nm}}{B_{nm}}\sin\left(n\pi Z/W_c\right)\sin\left(m\pi\hat{Y}/\delta_c\right) \tag{3-27}$$

In this form, the vapor velocity in the cavity can be determined based on the relevant dimensionless parameters and the unknown interface velocity (through the coefficient a_n). Additionally, the nondimensional shear stress at the liquid-vapor interface can calculated using the same definition of the dimensionless shear stress as employed in the one-dimensional cavity model. Doing so yields the follow expression.

$$T_c(Z) = \frac{\mu_v}{\mu_l}\frac{\partial U_i}{\partial \hat{Y}}\bigg|_{\hat{Y}=\delta_c} = \frac{2}{W_c^2}\sum_{n=1}^{\infty} n\pi a_n \sin(n\pi Z/W_c)\cosh(n\pi\delta_c/W_c) + \frac{2\Phi}{\delta_c^2}\sum_{n=1}^{\infty}\sum_{m=1}^{\infty}\frac{A_{nm}}{B_{nm}} m\pi \sin(n\pi Z/W_c)\cos(m\pi) \quad \textbf{(3-28)}$$

It is important to note once again that the above expression is dependent upon the unknown interface velocity. The analytical solution to the vapor cavity is then coupled to the liquid domain by assigning the liquid velocity and shear stress equal to those of the vapor at the interface. This was accomplished by means of a UDF as in the one-dimensional cavity model (see Appendix C for the two-dimensional cavity UDF code). The solution process with the UDF is illustrated in Figure 3-6. Initially, a solution is obtained using Fluent™ for the liquid domain by using the solution to the one-dimensional cavity model as the initial approximation. Subsequently, the liquid interfacial velocity is extracted from the solution by the UDF and is substituted into Equation 3-28 to solve for the shear stress distribution at the interface. Finally, the calculated shear stress distribution is applied as the liquid-vapor interface boundary condition for the liquid domain, and replaces the previous shear stress values. The liquid domain is then recomputed based on the updated boundary condition. The interfacial

boundary condition was updated approximately every 25 iterations until the solution to the liquid domain converged. The same scalar diffusion analogy used in previous laminar flow models was also implemented in the two-dimensional cavity model for the liquid domain.

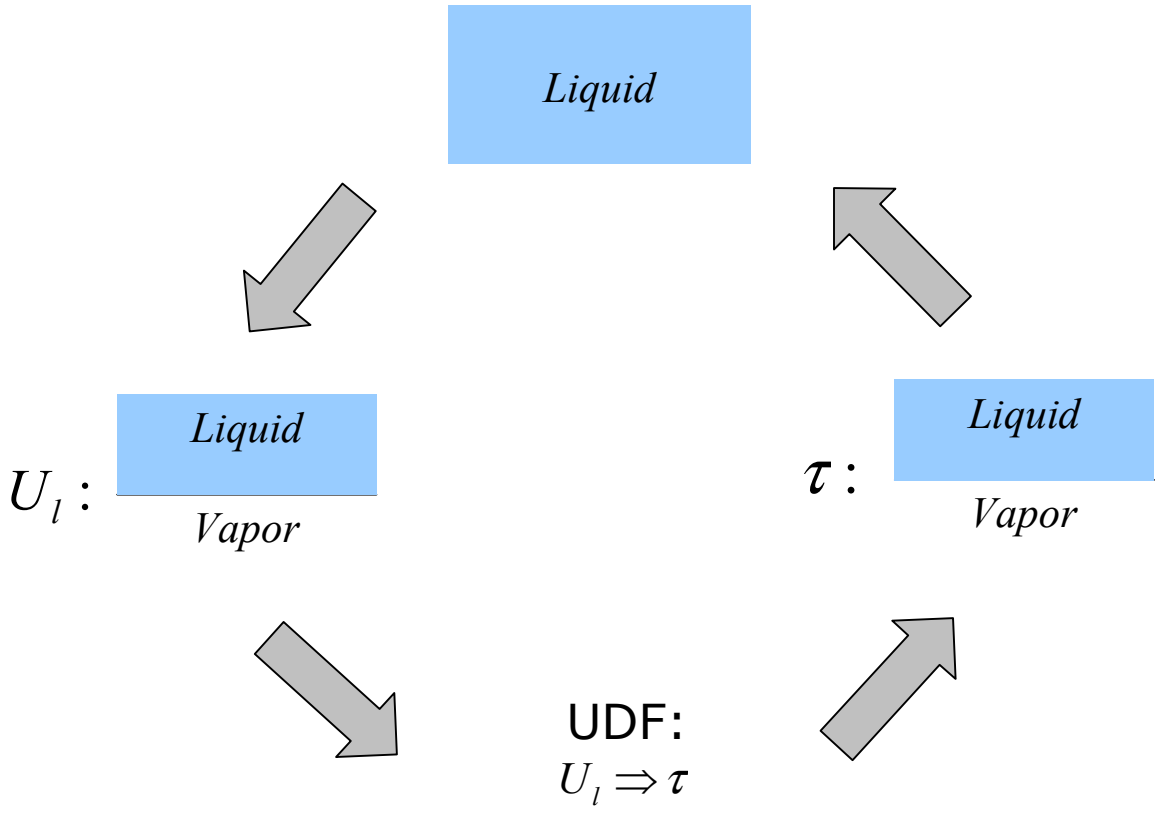

Figure 3-6 Cartoon illustrating a two-dimensional cavity model solution iteration

For grid-independent solutions, the same grid used in the one-dimensional cavity model of approximately 30,000 nodes was implemented. Also, it was found that 200 terms in the summations of Eq. 3-28 were sufficient to obtain unchanging accuracy in the shear stress predictions. For the two-dimensional cavity model all simulations were set with a relative cavity depth of δ_c = 0.1. A parametric cavity depth study was then

performed where the relative cavity depth was varied from 0.0 to 0.7. Additionally, the identical convergence criteria were also found to be appropriate for the two-dimensional cavity model as was used in the one-dimensional cavity model. Each case was allowed to run until the nondimensional shear stress was within 0.01% of the value of -1/4 and the average nondimensional velocity had ceased to change by more than 0.005%. Each two-dimensional cavity model case was initialized using the solution obtained for the one-dimensional cavity model for the same relative module width, cavity fraction, and cavity depth values.

3.2 Turbulent Flow Model

Consider turbulent flow through a three-dimensional rectangular channel with ultrahydrophobic top and bottom walls. The turbulent flow through the channel is considered to be steady and fully developed in a time-averaged sense with constant fluid properties. The width of the channel in consideration is much larger than the channel height, allowing the channel to be modeled as infinitely wide parallel plates. The micro-structures on the top and bottom walls consist of alternating ribs and cavities oriented parallel to the flow direction as in the laminar flow models. For the turbulent flow model the liquid meniscus shape at the cavity is modeled in an ideal manner as a flat interface along the entire length of the cavity.

To obtain a solution to the liquid domain, the Reynolds Averaged Navier-Stokes (RANS) equations are implemented and a k-ω model is employed for closure to the RANS equations. The governing equations in index notation are as follows:

$$\frac{\partial \overline{u}_i}{\partial x_i} = 0 \tag{3-29}$$

$$\rho\left(\frac{\partial \overline{u}_i}{\partial t} + \overline{u}_i \frac{\partial \overline{u}_i}{\partial x_j}\right) = -\frac{d\overline{P}}{dx_i} + \mu\nabla^2 \overline{u}_i - \frac{\partial}{\partial x_j}\left(\rho\overline{u_i' u_j'}\right) \tag{3-30}$$

$$\rho\left(\frac{\partial \kappa}{\partial t} + \overline{u}_i \frac{\partial \kappa}{\partial x_i}\right) = \frac{\partial}{\partial x_j}\left(\Gamma_k \frac{\partial \kappa}{\partial x_j}\right) + G_\kappa - Y_\kappa \tag{3-31}$$

$$\rho\left(\frac{\partial \omega}{\partial t} + \overline{u}_i \frac{\partial \omega}{\partial x_i}\right) = \frac{\partial}{\partial x_j}\left(\Gamma_\omega \frac{\partial \omega}{\partial x_j}\right) + G_\omega - Y_\omega. \tag{3-32}$$

In the above equation, $\overline{u}_i$ is the time averaged velocity, u_i' is the fluctuating velocity component, $\overline{P}$ represents the time averaged pressure, x_i is the spatial coordinate, κ is the kinetic energy, and ω is the dissipation rate of kinetic energy. Γ is the effective diffusivity of κ, and ω, and is defined as

$$\Gamma_\kappa = \mu + \frac{\mu_t}{\sigma_\kappa} \tag{3-33}$$

$$\Gamma_\omega = \mu + \frac{\mu_t}{\sigma_\omega} \tag{3-34}$$

where μ is the liquid viscosity, and μ_t is the turbulent viscosity defined as $\mu_t = \alpha^* \rho\kappa/\omega$. The closure coefficients, σ, are closure coefficients set at σ_κ= 2.0 and σ_ω= 2.0. All coefficients in the current study are in accordance to those determined by Wilcox [50] for boundary layer flow with a pressure gradient. The coefficient α^* is a low-Reynolds-

number correction that works by damping the turbulent viscosity and is defined as follows.

$$\alpha^* = \alpha_\infty^* \left(\frac{\alpha_\circ^* + \mathrm{Re}_t / R_\kappa}{1 + \mathrm{Re}_t / R_\kappa} \right) \tag{3-35}$$

In the above, Re_t is the turbulent Reynolds number, $\mathrm{Re}_t = \rho\kappa/\mu\omega$, and the coefficients are set as follows, R_κ = 6, α_∞^*=1, $\alpha_\circ^* = \beta_i/3$, and $\beta_i = 0.072$. Referring back to Equations 3-31 and 3-32, G and Y represent the generation and dissipation of both κ and ω, respectively. The generation of turbulent kinetic energy and of the dissipation rate of kinetic energy can be expressed, respectively, as

$$G_\kappa = -\rho \overline{u_i' u_j'} \frac{\partial u_j}{\partial x_i} \tag{3-36}$$

$$G_\omega = \alpha \frac{\omega}{\kappa} G_\kappa \tag{3-37}$$

where

$$\alpha = \frac{\alpha_\infty}{\alpha^*} \left(\frac{\alpha_0 + \mathrm{Re}_t / R\omega}{1 + \mathrm{Re}_t / R\omega} \right) \tag{3-38}$$

and $R_\omega = 2.95,\ \alpha_\infty = 0.52,\ \alpha_0 = 1/9$. The dissipation of the turbulent kinetic energy, Y_κ is defined as

$$Y_\kappa = \rho\beta^* f_{\beta^*}\kappa\omega \tag{3-39}$$

where

$$f_{\beta^*} = \begin{cases} 1 & \chi_\kappa \le 0 \\ \dfrac{1+680\chi_\kappa^2}{1+400\chi_\kappa^2} & \chi_\kappa > 0 \end{cases} \tag{3-40}$$

$$\chi_\kappa = \frac{1}{\omega^3}\frac{\partial\kappa}{\partial x_j}\frac{\partial\omega}{\partial x_j}. \tag{3-41}$$

$$\beta^* = \beta_i^*\left[1+\zeta^* F(M_t)\right] \tag{3-42}$$

$$\beta_i^* = \beta_\infty^*\left(\frac{4/15+\left(\mathrm{Re}_t/R_\beta\right)^4}{1+\left(\mathrm{Re}_t/R_\beta\right)^4}\right) \tag{3-43}$$

and, $\zeta^* = 1.5$, $R_\beta = 8$, and $\beta_\infty^* = 0.09$. Further, $F(M_t) = 0$ for an incompressible liquid flow. The dissipation of the turbulent kinetic energy dissipation rate is expressed as

$$Y_\omega = \rho\beta f_\beta \omega^2 \tag{3-44}$$

where

$$\beta = \beta_i \left(1 - \frac{\beta_i^*}{\beta_i} \zeta^* F(M_t) \right) \tag{3-45}$$

$$f_\beta = \frac{1 + 70\chi_\omega}{1 + 80\chi_\omega} \tag{3-46}$$

$$\chi_\omega = \left| \frac{\Omega_{ij}\Omega_{jk}S_{ki}}{(\beta_\infty^* \omega)^3} \right| \tag{3-47}$$

$$\Omega_{ij} = \frac{1}{2}\left(\frac{\partial u_i}{\partial x_j} - \frac{\partial u_j}{\partial x_i} \right) \tag{3-48}$$

$$S_{ij} = \frac{1}{2}\left(\frac{\partial u_j}{\partial x_i} + \frac{\partial u_i}{\partial x_j} \right) \tag{3-49}$$

In the given scenario, the computational domain can be confined to a small, three-dimensional repeatable section consisting of a single rib and cavity that extends the length of the channel and is limited to half the total channel height, as shown in Figure 3-7. It is important to note that the figure shows only a two-dimensional cross-section of the computational domain, which in reality extends perpendicular to the image in the *x*-direction. The liquid domain extends from $0 \le y \le H$, from $0 \le z \le W$, and from $0 \le x \le L$, where H is half the channel height and L is the length of the channel (Figure 3-8). The width of the computational domain is represented as W and is defined as, $W = w_c + w_r$, where w_c is the cavity width and w_r is the width of the solid rib. In solving Equations 3-29 to 3-32 for the liquid domain, the boundary conditions were set as follows. At the channel centerline, for $y = H$, $0 \le z \le W$, and $0 \le x \le L$, a symmetry condition was applied, which is mathematically represented as a zero velocity gradient, $\partial u/\partial y = 0$. Since the computational domain consists of a repeating section a periodic boundary

condition was implemented at $z = 0$ and $z = W$ for $0 \leq y \leq H$ and $0 \leq x \leq L$, requiring the liquid velocity to be equal at identical vertical locations a long both sides of the domain. A periodic condition is also employed at the channel inlet, $x = 0$, and exit, $x = L$, for $0 \leq y \leq H$ and $0 \leq z \leq W$, to allow for a streamwise, time-averaged fully developed flow. Additionally, the classical no-slip boundary condition was enforced at the rib, for $w_c \leq z \leq w_r$ at $Y = 0$ and $0 \leq x \leq L$. For the liquid-vapor interface, $0 \leq z \leq w_c$ and $0 \leq x \leq L$, at $y = 0$ a vanishing shear stress boundary condition was applied.

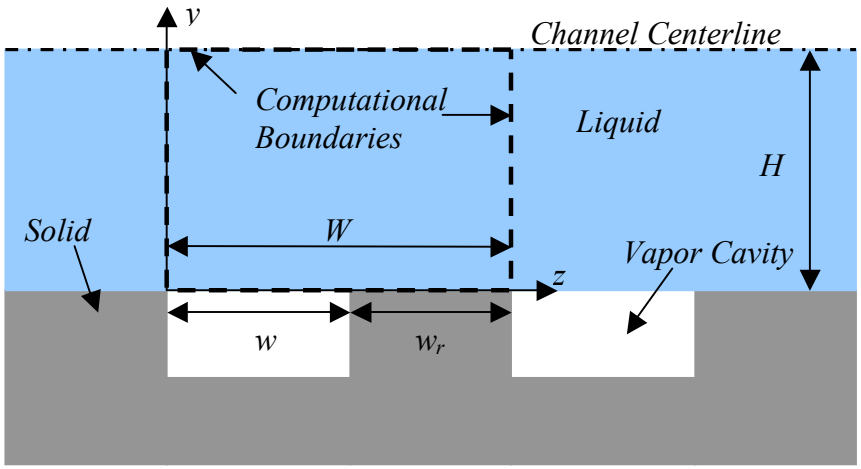

Figure 3-7 Schematic of a two-dimensional cross section of the turbulent flow model computational domain

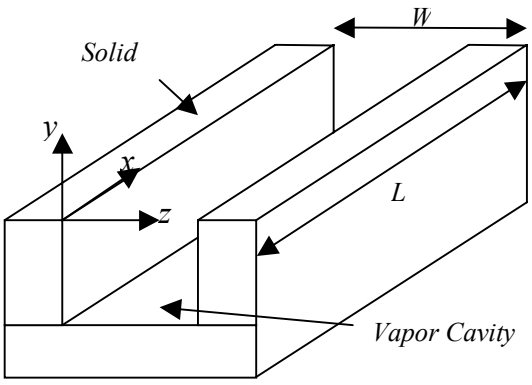

Figure 3-8 Illustration of the defined coordinate system for the three-dimensional turbulent flow model

In the research presented, three important dimensionless parameters exist. These being the relative module width, $W_m = W/D_h$, the relative cavity fraction, $F_c = w_c/W = W_c/W_m$, and the Reynolds number, $\mathrm{Re} = \bar{u}D_h/\nu$. In the numerical analysis, W_m was varied from 0.01-1.0, F_c was varied from 0-0.97, and a Reynolds number range of 2,000-10,000 was explored.

To quantify the global frictional resistance, the Darcy friction factor, *f*, was calculated and compared to values calculated for a full no-slip parallel plates channel. The average Darcy friction factor is defined as

$$f = 4C_f = 8\bar{\tau} \Big/ \left(\rho \bar{u}^2\right) \tag{3-50}$$

where C_f is the average skin friction coefficient and $\bar{\tau}$ is the average shear stress at the liquid-solid boundary of the liquid domain. The average shear stress is computed at the channel wall, including both the liquid-solid interface (rib) and the liquid-vapor interface (cavity). Empirical correlations developed for turbulent flow through smooth rectangular ducts may be used for model validation under conditions of a no-slip boundary everywhere. The often-used expression presented by Blasius [46] for the Darcy friction factor is

$$f = \frac{0.316}{\mathrm{Re}^{1/4}} \tag{3-51}$$

and has stated applicability for the Reynolds number range of $4{,}000 \leq Re \leq 100{,}000$. Although this correlation was developed for flow through a smooth pipe, it can be modified for channel flow using a Reynolds number based on an effective diameter, $D_{eff} = 64D_h/k$, where k is equal to 96 for parallel plate channel flow [47]. Other correlations include those developed by Beavers et al. [48] and Dean [49] as shown:

$$f = \frac{0.5072}{\mathrm{Re}_h^{0.3}} \tag{3-52}$$

$$f = \frac{0.3472}{\mathrm{Re}_h^{1/4}} \tag{3-53}$$

These correlations are recommended for use over the Reynolds number ranges of $5{,}000 \leq Re \leq 30{,}000$ and $12{,}000 \leq Re \leq 1{,}200{,}000$, respectively. Although the recommended Reynolds number range for the Dean correlation is much higher than the Reynolds number range explored in the current study, the calculated values using the correlation are very close to those computed using the other correlations (with a maximum difference of 2.5% when compared to the Blasius formula). Therefore, the Dean correlation is still included in the model validation.

The liquid domain was discretized and the governing equations were integrated at each cell. Only a few cells were created in the streamwise direction since a Reynolds averaged solution method was employed. As in the laminar flow models, the commercial software Fluent™ was employed to solve the fluid domain where a k-ω model was

implemented for closure to the RANS equations. The coefficients relevant to this model were maintained at the default settings set by Fluent™, which are set to match those determined by Wilcox [50] for boundary layer flow as stated previously. Although they were also defined previously, the coefficients are repeated here for convenience.

$$\alpha_\infty^* = 1;\ \alpha_\infty = 0.52;\ \alpha_0 = 1/9;\ \beta_\infty^* = 0.09;\ \beta_i = 0.072;\ R_\beta = 8$$

$$R_\kappa = 6;\ R_\omega = 2.95;\ \zeta^* = 1.5;\ \sigma_\kappa = 2.0;\ \sigma_\omega = 2.0$$

Grid independence was achieved with a grid of nominally 80,000 cells, requiring approximately 100,000 iterations for convergence. The f and C_f values were monitored to ensure their complete convergence. The solution was considered converged when the f and C_f values ceased to change more than 0.01%. Additionally, simulations were set up using an enhanced wall treatment feature in Fluent™ which allows for resolution into the viscous sublayer to approximately $y^+ \sim 1$. As a result, the nearest wall node for each of the simulations is adaptively positioned near a value of $y^+ = 1$ of the liquid domain as recommended in the Fluent™ documentation. To insure compliance to this requirement, each grid was adapted until the nearest node point was within 5% of $y^+ = 1$. A difference of 5% in the y^+ value was seen to influence the f value by less than 1%.

4 Laminar Flow Results

4.1 Zero Shear Stress Model

Figure 4-1 illustrates numerical *fRe* predictions as a function of the cavity fraction. In the figure, each line represents a different value of the relative module width. To facilitate comparison, a line that denotes the classical parallel plate channel value of *fRe* = 96 is included. It can therefore be understood that any deviation from this value signifies a reduction in the total frictional resistance in the channel. As the cavity fraction approaches zero, the *fRe* predictions for each relative module width converge at the classical value of 96. It is also observed that *fRe* decreases with increasing values of the cavity fraction. A larger cavity fraction represents a computational domain with a larger cavity-to-rib ratio, which increases the relative area where the zero shear boundary condition exists. Therefore, the influence of the zero shear stress boundary condition on the liquid flow is larger and a more significant reduction in the frictional resistance is obtained. It can also be deduced from Figure 4-1 that the *fRe* predictions decrease for increasing values of the relative module width. Larger values of the relative module width signify a liquid computational domain that has a smaller height-to-width aspect ratio, meaning the width of the cavity is larger in relation to the channel height. This

condition allows for the influence of the vapor cavity to diffuse through a larger percentage of the liquid domain and thus results in greater reductions in the *fRe* value.

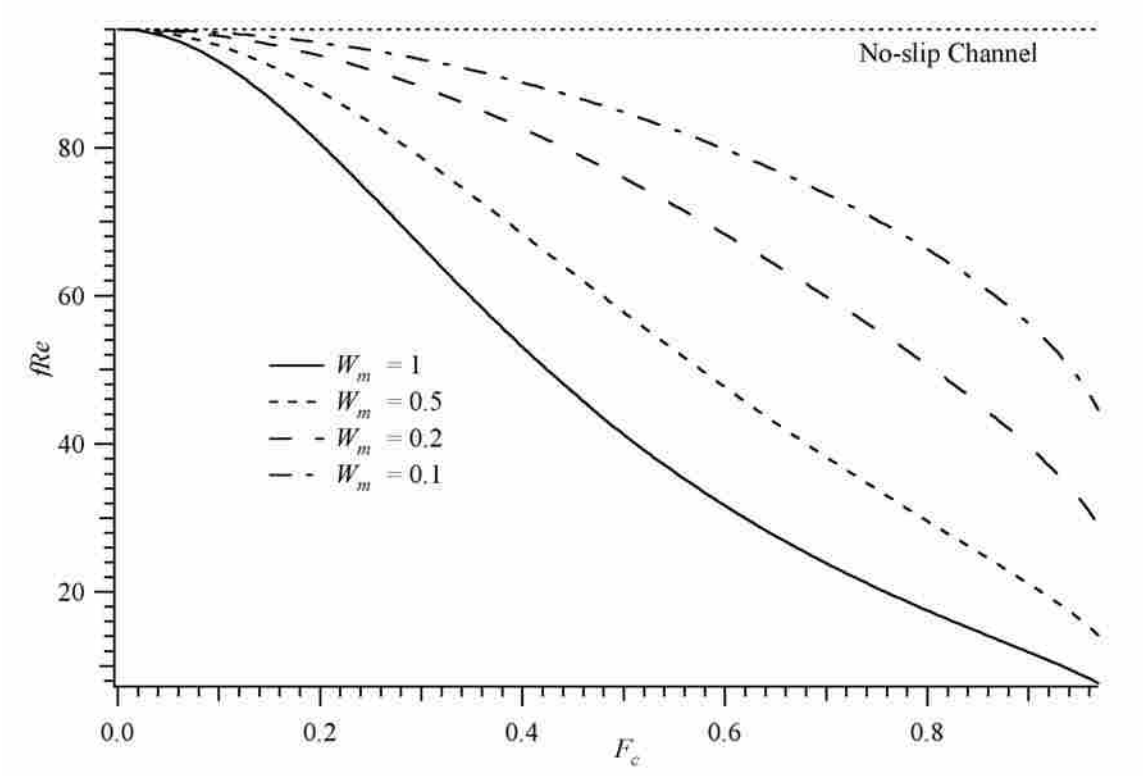

Figure 4-1 Numerical prediction of *fRe* as a function of the cavity fraction, for relative module widths of 0.1, 0.2, 0.5, and 1

Additionally, Figure 4-1 illustrates the magnitude of the reductions in the friction resistance that the use of ultrahydrophobic surfaces enables. For a relative module width of W_m = 1 and a cavity fraction of F_c = 0.97, an unprecedented 92% reduction is observed. Even for a more realistic relative module width value of W_m = 0.1 and a cavity fraction of F_c = 0.97, a 53% reduction is shown to be achievable.

Figure 4-2 contains a comparison between the numerical predictions using the zero shear stress model and the values calculated using the analytical expression developed by

Lauga and Stone [26], Equation 3-12. Shown in the figure are normalized slip length values as a function of the cavity fraction, and includes the numerical predictions for the relative module widths of W_m = 0.2, 0.5, and 1.0. Examination of the presented data shows very good agreement between the predicted values and the exact solution.

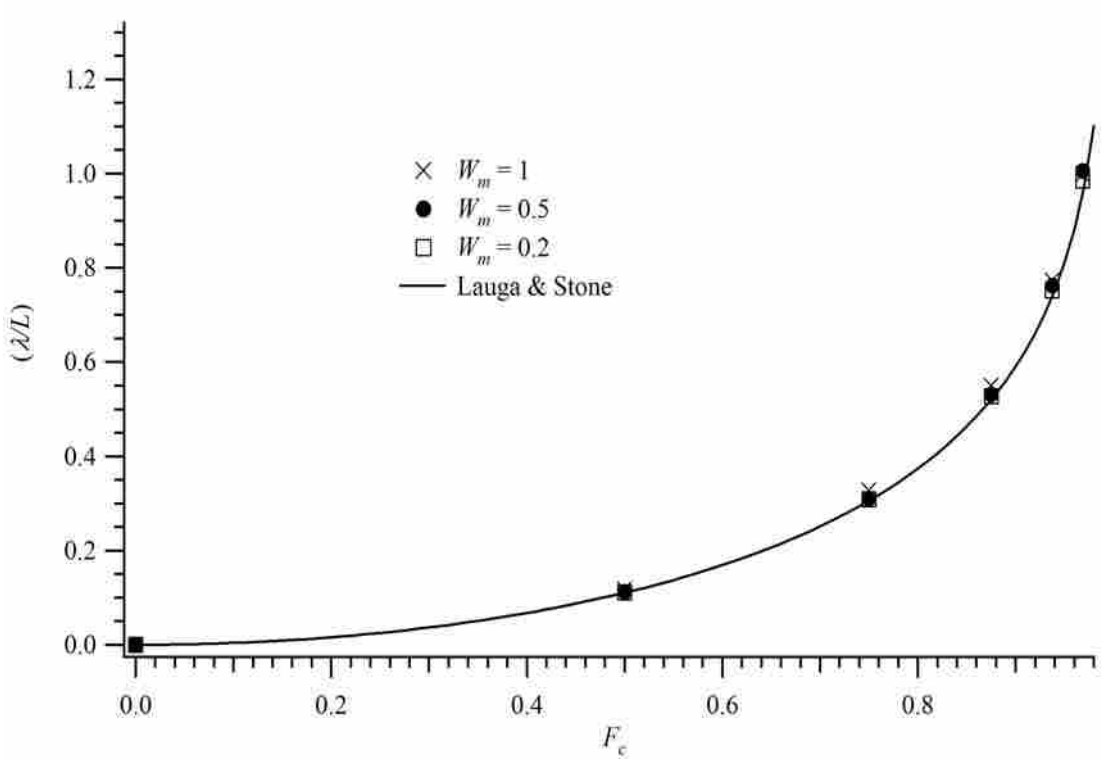

Figure 4-2 Normalized slip length predictions as a function of the cavity fraction for the relative module widths of W_m = 0.2, 0.5, and 1.0 in comparison to the analytical expression developed by Lauga and Stone, Equation 3-12

4.1.1 Liquid Meniscus Model

The liquid meniscus, zero shear model was confined only to a channel with a relative module width of W_m = 1.0 and a cavity fraction of F_c = 0.87. The purpose of this model again is to test the validity of the flat liquid-vapor assumption used in the models. Shown in Table 4-1 are the *fRe* predictions for the nondimensional meniscus depth values

of $\xi = 0.0$, 0.01, 0.05, and 0.1. The value obtained for a meniscus depth of $\xi = 0$ represents the value obtained in the zero shear stress model. As illustrated in the table, *fRe* increases as the depth of the meniscus increases. Since the interfacial boundary condition is that of zero shear stress, the increased surface area does not contribute to the observed increase in frictional resistance. Instead, this increase could be accounted for by considering that the meniscus introduces an uneven boundary over which the liquid is forced to pass. However, it can also be observed from the table that the increase in the frictional resistance due to the presence of the meniscus is insignificant. An increase of only 4% in *fRe* is experienced over the nondimensional meniscus depth range of $\xi = 0 - 0.1$. The nondimensional value of $\xi = 0.1$ represents a meniscus depth that is 40% of the channel height, which is much larger than could be achieved without the liquid wetting the cavity. It is important to note that this approximate model does not account for the added shear stress due to the penetration into the cavity since a zero shear stress boundary is still assumed.

Table 4-1 Predictions of *fRe* as a function of the dimensionless meniscus depth, ξ

ξ	F_c	*fRe*
0.00	0.87	12.77
0.01	0.87	12.76
0.05	0.87	13.11
0.10	0.87	13.29

4.2 One-Dimensional Cavity Model

Figure 4-3 illustrates *fRe* predictions as a function of the cavity fraction for the relative module width values of W_m = 0.25 and 1.0, and a relative cavity depth of δ_c = 0.1. Included in the figure are the friction factor-Reynolds number product calculations for both the zero shear and the one-dimensional cavity models. As can be seen in the figure, the zero shear stress model over-predicts the reduction in the total frictional resistance. This of course is due to the fact that the zero shear model is an idealization of the actual interfacial physics. The cavity model in discussion shows that, albeit small, a non-zero shear stress exists at the liquid-vapor interface. The magnitude of which will be further examined in the discussion of the two-dimensional cavity model.

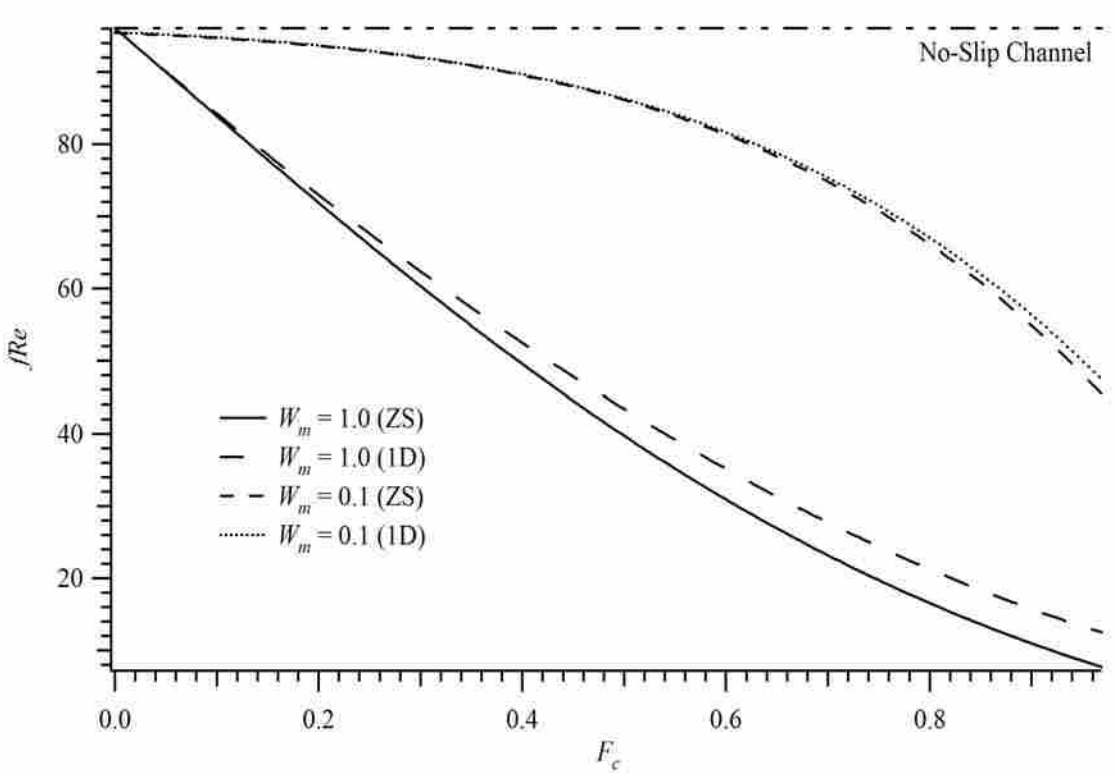

Figure 4-3 Predictions of *fRe* for the one-dimensional cavity model (1D) compared to the zero shear model (ZS) as a function of cavity fraction, for W_m = 0.1 and 1.0, and δ_c = 0.1

Further, the difference between the predicted values of each model is observed to increase with increasing relative module width. For a relative module width of $W_m = 1.0$ and a cavity fraction of $F_c = 0.97$, a 40% difference exists between the predicted values of the two models, whereas for the module width of $W_m = 0.1$, only a 5% difference is observed for the same cavity fraction. This may be attributed to the fact that an increased relative width signifies an increased cavity area and a decreased channel height relative to the increasing width. In such a channel the interfacial boundary condition will have a larger influence on the liquid flow dynamics, and therefore be more sensitive to changes in the boundary conditions.

4.2.1 One-Dimensional Cavity Depth Study

Table 4-2 illustrates the *fRe* predictions obtained in the cavity depth study using the one-dimensional cavity model. Predicted values shown in the table are limited to those for the relative module width values of $W_m = 0.1$ and 1.0, and the cavity fraction values of $F_c = 0.94$ and 0.97. The relative cavity depth was varied from $\delta_c = 0.006$ to 0.1. It is observed from the table that as the cavity depth increases, the predicted *fRe* value is decreased. The data clearly shows that the total frictional resistance of the channel depends significantly on the cavity geometry. From a change in the nondimensional cavity depth from 0.006 to 0.1, a 21% decrease in the *fRe* is observed for the case of $W_m = 0.1$ and $F_c = 0.94$. Additionally, for the case of $W_m = 1.0$ and $F_c = 0.97$, a 73% decrease in *fRe* occurs. As the cavity depth increases the predicted *fRe* value continues to decrease as it approaches the ideal value predicted by the zero shear stress model, which were calculated for the two cases mention above to be 49.72 and 9.34, respectively. Further,

the magnitude that the *fRe* value decreases can be observed to lessen as the cavity depth continues to increase. This suggests that the friction factor-Reynolds number product may become independent of the cavity depth once a specific depth is achieved. However, the extent of this preliminary cavity study is insufficient to accurately specify that required depth.

Table 4-2 Prediction of *fRe* as a function of the relative cavity depth for the cavity fraction values of 0.94 and 0.97

$W_m = 0.1$			$W_m = 1.0$		
δ_c	F_c	*fRe*	δ_c	F_c	*fRe*
0.100	0.94	51.48	0.100	0.94	14.09
0.063	0.94	50.11	0.063	0.94	16.71
0.031	0.94	54.23	0.031	0.94	22.92
0.006	0.94	65.27	0.006	0.94	51.08
0.100	0.97	44.63	0.100	0.97	12.21
0.063	0.97	45.64	0.063	0.97	14.85
0.031	0.97	48.14	0.031	0.97	21.16
0.006	0.97	61.77	0.006	0.97	49.84

4.3 Two-Dimensional Cavity Model

Figure 4-4 illustrates the *fRe* calculations as a function of the cavity fraction for the two-dimensional vapor cavity model (2D) for the relative module width values of W_m = 0.1 and 1.0. Also included in the figure are the *fRe* predictions for the zero shear stress model (ZS). The same conclusions can be made in response to this data as were made for the one-dimensional cavity model. That is, the zero shear stress model over predicts the reduction in the total frictional resistance, since in actuality a non-zero shear stress exists

at the liquid-vapor boundary. Also, the difference between the two models increases as the relative module width increases. This is due again to the fact that the increased relative width also increases the area over which the reduced shear boundary is effective, thus increasing the amount of influence the interfacial boundary has on the liquid flow dynamics.

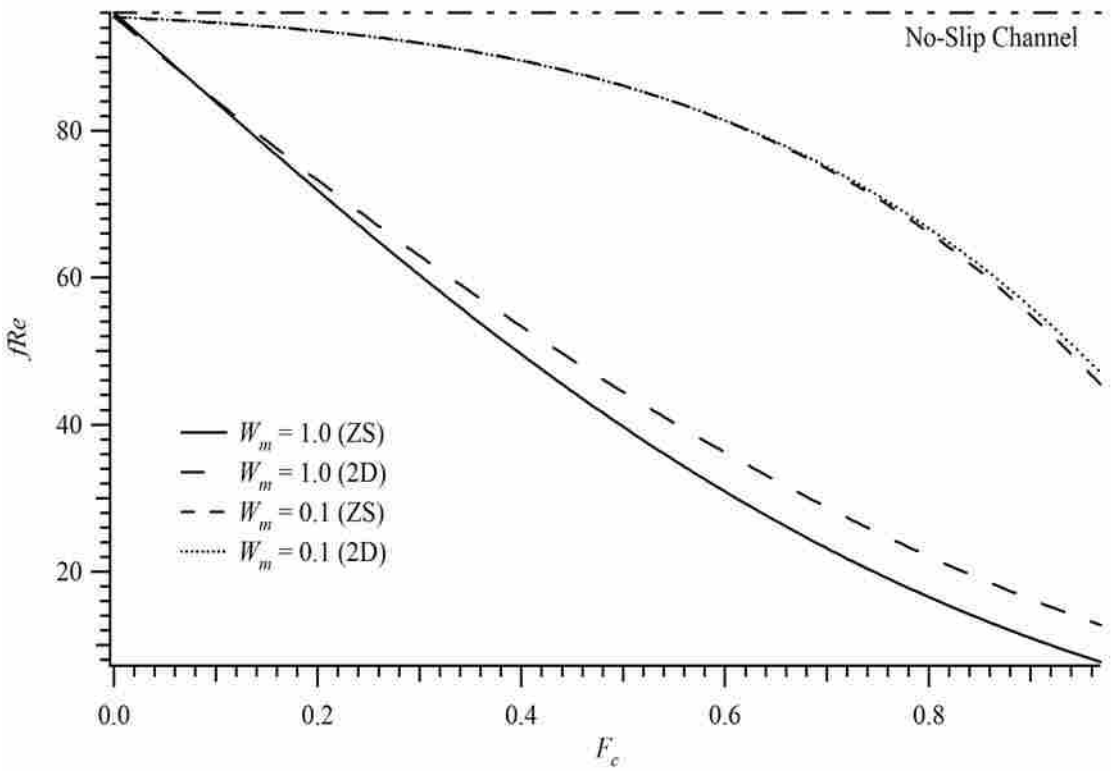

Figure 4-4 Predictions of *fRe* for the two-dimensional model (2D) compared to the zero shear (ZS) values as a function of the cavity fraction, for W_m = 0.1 and 1.0, and δ_c = 0.1

Illustrated in Figure 4-5 are slip length predictions as a function of the cavity fraction for the module widths of W_m = 0.5 and 1.0, and for a dimensionless cavity depth of δ_c = 0.1. Also included in the figure are the slip length values for the zero shear stress model. As expected, for a cavity fraction of F_c = 0 the slip length is seen to approach

zero for each case presented. Just as with the *fRe* predictions displayed in Figure 4-4, λ/W increases as the cavity fraction is increased. Further, when the zero shear stress model is used, λ/W is independent of W_m as is described by Equation 3-12. However, when the vapor cavity solution is coupled to the liquid domain, the slip-length is seen to decrease with increasing relative module width, W_m. For example, at a cavity fraction of $F_c = 0.97$ and a relative width of $W_m = 1.0$ the relative difference between the zero shear stress model and the two-dimensional cavity model predictions is nearly a factor of two.

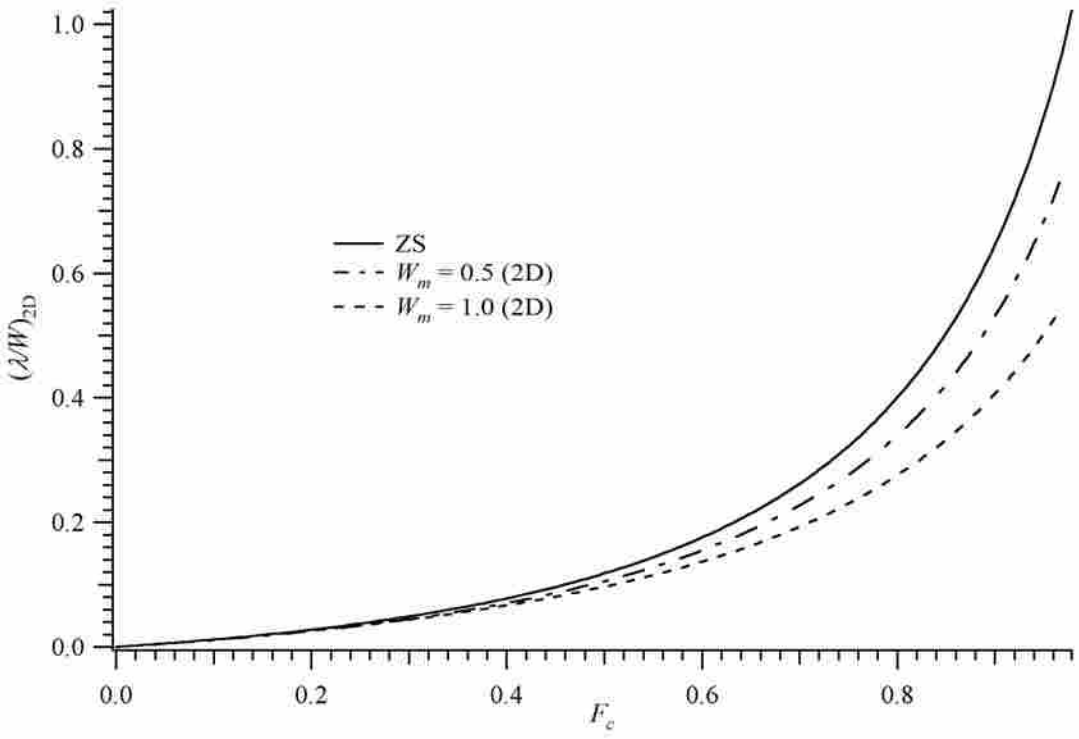

Figure 4-5 Predicted slip length values as a function of the cavity fraction for relative module widths of W_m = 0.5 and 1.0

Although the two-dimensional vapor cavity model is a more accurate depiction of the actual physics of the flow, when compared to Figure 4-3, the two-dimensional cavity

model data presented in Figure 4-4 does not appear significantly different from that obtained using the one-dimensional cavity model. For comparison, Table 4-3 contains predictions of *fRe* for both the one-dimensional and two-dimensional vapor cavity models. Examining the values from the two different models for the same relative module width reveals a very insignificant variation. For a relative module width of W_m = 1.0 and a cavity fraction of F_c = 0.97, only a 2% change occurs from the one-dimensional model to the two-dimensional model. This small difference between the two cavity models is also observed to decrease as the cavity fraction decreases. For the same cavity fraction in the example above but for the relative module width of W_m = 0.1, less than a 1% difference exists between models. This may be accounted for by the fact that as the cavity fraction increases, the variation in the interfacial velocity and shear stress becomes greater and the side effects of the cavity more significant; thus rendering the assumption of an average velocity and shear stress value a less adequate representative of the actual physics.

Table 4-3 Comparison of *fRe* predictions from both the one-dimensional (1D) and two-dimensional (2D) cavity models, for δ_c = 0.1

F_c	*fRe*			
	W_m = 1.0		W_m = 0.1	
	1D	2D	1D	2D
0.50	43.46	43.72	84.93	84.63
0.75	24.06	26.59	70.80	70.44
0.88	17.34	17.56	59.78	59.55
0.94	14.09	14.29	51.50	51.10
0.97	12.21	12.41	44.64	44.06

Further examination of the data presented in Table 4-3 show that the difference in *fRe* predictions between the one and two-dimensional models decreases for decreasing relative module width. This is expected since the liquid-vapor boundary exerts less influence on the liquid domain for smaller relative module widths, and therefore, a more sophisticated model does little to increase the accuracy of the prediction. It is interesting to note however, that the one-dimensional *fRe* calculations are greater than those for the two-dimensional model for the smaller relative module width. This phenomenon occurs for all the lower values of relative module width examined in this study, although it is unclear as to why this occurs. It is possible that the average interfacial shear stress approximation in the one-dimensional cavity model over-predicts the shear stress and thus, a larger *fRe* value is calculated. However, despite the apparent similarity between the one-dimensional and two-dimensional predictions of *fRe*, the two-dimensional vapor cavity model allows for a more complete examination of the fluid flow dynamics that cannot be achieved using the one-dimensional model.

An examination of the velocity profiles helps illustrate the physical phenomenon at the liquid-vapor interface which creates the large decrease in the total frictional resistance in the channel. Nondimensional velocity predictions are illustrated in Figure 4-6 as a function of the normalized transverse coordinate, $\zeta = z/w$, for both the zero shear stress (solid lines) and two-dimensional cavity models (dashed lines). The predictions displayed are for a relative module width of $W_m = 0.25$, a relative cavity depth of $\delta_c = 0.1$, and for the cavity fraction values of $F_c = 0.50$, 0.88, and 0.97. As the velocity profiles show, the no-slip condition holds at the rib, but due to the non-zero shear stress at the liquid-vapor interface, a non-zero velocity exists over the vapor cavity region. This

enhancement of the fluid velocity at the vapor cavity is the source of the enhanced fluid flow. Shown in the figure for each profile is the average liquid velocity prediction obtained from the two-dimensional cavity model. Numerical predictions show an average velocity of $\overline{U}_l = 0.021$ for a no-slip parallel plate channel flow. A quick comparison between this value and those indicated in Figure 4-6 reveals the significant enhancement of the fluid flow in the channel due to the reduced frictional resistance. Further, it is also observed that as the cavity fraction increases, the average normalized liquid velocity increases; this trend is in direct relation to that of the *fRe* value increasing with increased cavity fraction as previously discussed.

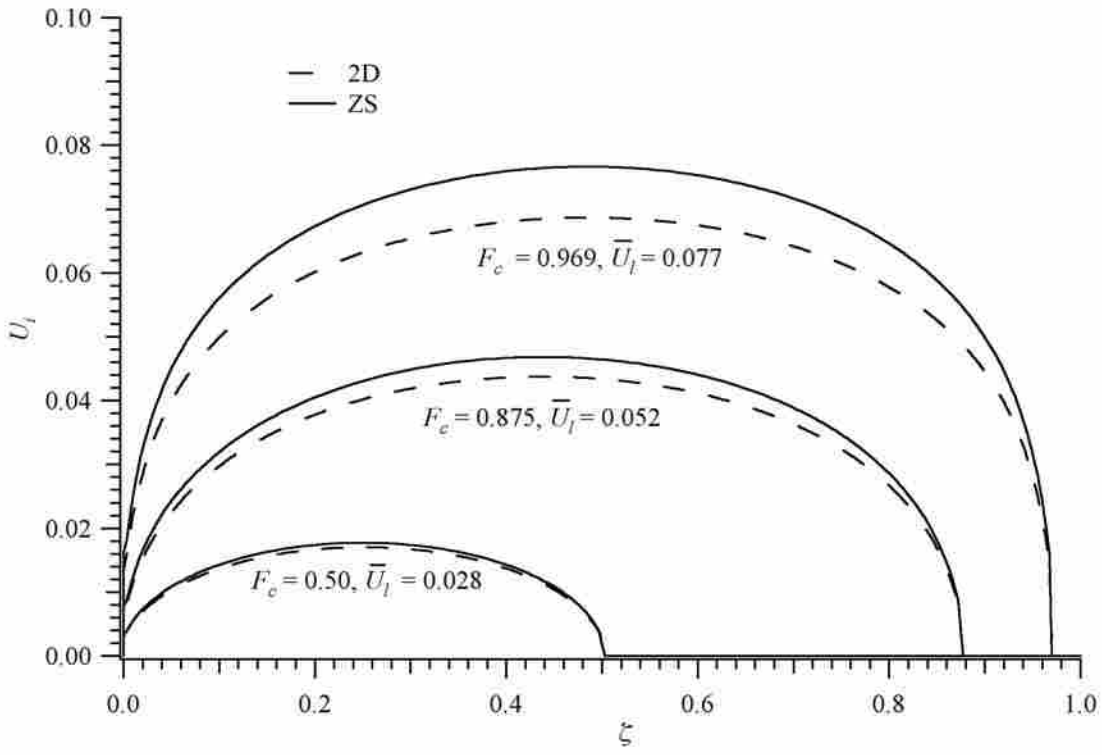

Figure 4-6 Predictions of the normalized velocity at the liquid-vapor interface as a function of $\zeta = z/w$ for a relative module width of $W_m = 0.25$, a relative cavity depth of $\delta_c = 0.1$, and cavity fractions of $F_c = 0.50$, 0.88, and 0.97.

It is also interesting to note from Figure 4-6 the difference between the normalized velocity profiles of both the zero shear stress and two-dimensional cavity models. As is expected, the assumption of a zero shear stress at the liquid-vapor interface allows for the development of a higher average channel velocity. Accounting for the small amount of interfacial shear stress reduces that value from the ideal by accounting for the strong dependence upon the vapor flow dynamics in the cavity. Further, it is observed that the difference between the velocity profiles decreases as the cavity fraction decreases. This indicates that the interfacial shear stress at the cavity approaches zero as the cavity fraction decreases. Only for larger cavities does the shear stress become large enough to have a significant influence on the channel flow.

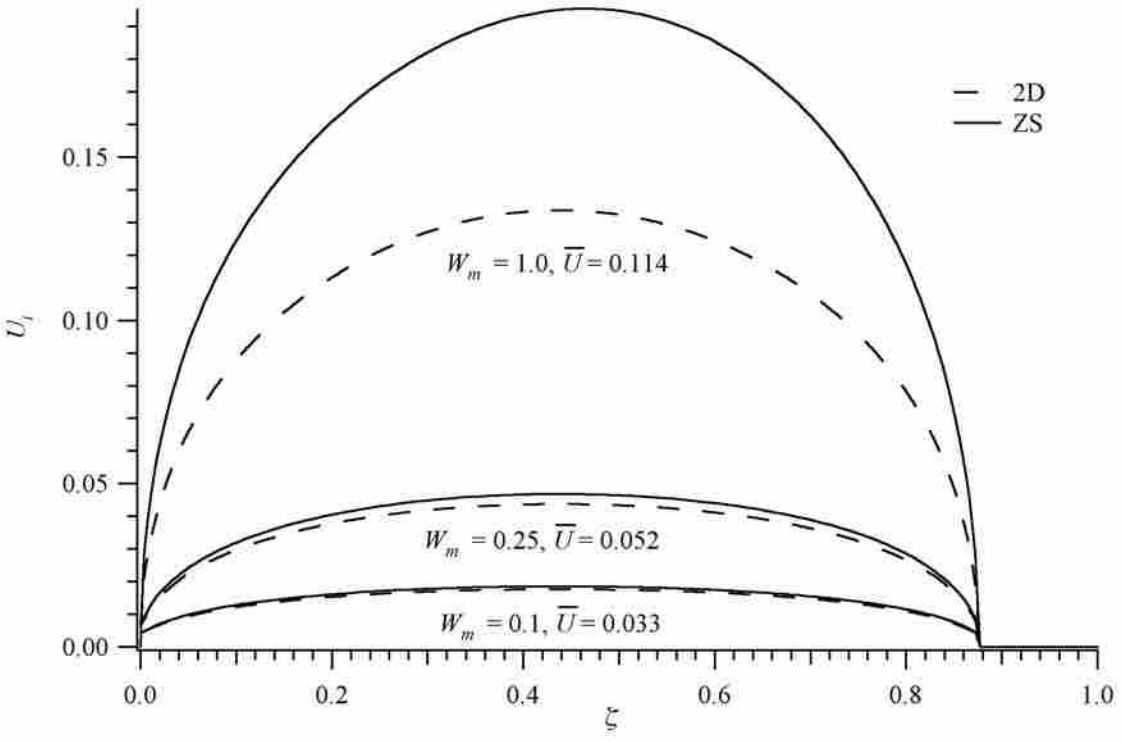

Figure 4-7 Normalized velocity predictions as a function of the normalized transverse coordinate, $\zeta = z/w$ for a cavity fraction of F_c = 0.88, a relative cavity depth of δ_c = 0.1, and for relative module widths of W_m = 0.1, 0.25, 1.0

Figure 4-7 also illustrates nondimensional velocity profiles plotted as a function of the dimensionless transverse coordinate, $\zeta = z/w$, for both the zero shear stress and two-dimensional cavity models. The represented profiles are for a cavity fraction of F_c = 0.88, a relative cavity depth of δ_c = 0.1, and for the relative module widths of W_m = 0.1, 0.25, and 1.0. Again, the average liquid velocity is included for the two-dimensional cavity model predictions. As is expected, the average velocity is observed to increase as the relative module width increases. This increased average velocity in conjunction with an increased module width is the cause of the previously observed dependence of the *fRe* on the relative module with. Since, for a fixed hydraulic diameter, a larger value of the relative module width essentially means a larger cavity in relation to the channel height, the predicted interfacial shear stress has a more significant influence on the channel flow dynamics.

Displayed in Figure 4-8 are nondimensional shear stress predictions as a function of the normalized transverse coordinate $\zeta = z/w$, for the two-dimensional cavity model at $Y = 0$. Included in the figure are predictions of the relative module width of W_m = 0.1 and 0.25, a relative cavity depth of δ_c =0.1, and for cavity fractions of F_c = 0.50, 0.88, and 0.97. As Equation 3-8 indicates, for the laminar flow models, the normalized average shear stress is -1/4. Figure 4-8 illustrates that this holds even as the width of the rib is decreasing with increased cavity fractions. Since the interfacial shear stress is near zero, the shear stress at the rib must increase to maintain the constant average of -1/4. Therefore, as the cavity fraction increases, the maximum shear stress at the rib also increases. It can be observed in the figure that the maximum shear stress for a cavity fraction of F_c = 0.97 is approximately three times that for the F_c = 0.50 case. It can

further be observed that the maximum shear stress occurs at the liquid transitions from the cavity to the rib and vise versa. This sudden change in velocity causes a spike in the shear stress, which is then seen to approach a minimum value at the center of the rib.

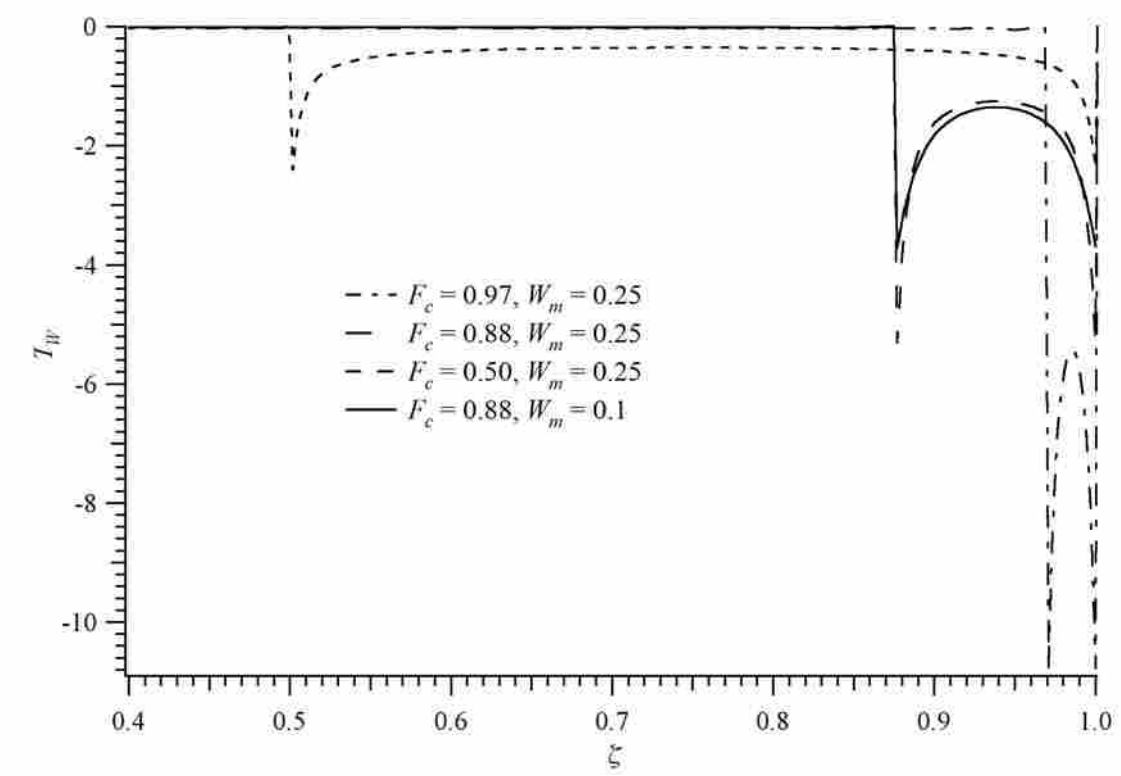

Figure 4-8 Normalized interfacial shear stress profiles as a function of $\zeta = z/w$ for a relative widths of $W_m = 0.1$ and 0.25, a relative cavity depth of $\delta_c = 0.1$, and for cavity fractions of $F_c = 0.5$, 0.88, and 0.97

Displayed in Figure 4-9, are nondimensional liquid velocity profiles as a function of the dimensionless wall-normal coordinate, Y, at various locations in the transverse coordinate, Z, for $W_m = 0.1$, $F_c = 0.88$, and $\delta_c = 0.1$. The inset figure illustrates the relative location of each of the profiles. The locations labeled *a* and *e* represent the center of the vapor cavity and the solid rib, respectively. Satisfying the no-slip condition, the liquid velocity approaches zero at the liquid-solid boundary. However, an increase in

the slip-velocity (non-zero liquid velocity at the wall, $Y = 0$) occurs as one progresses to the vapor cavity center where a maximum value is obtained. Using this velocity data, one could then calculate the weighted average velocity profile for the entire liquid domain.

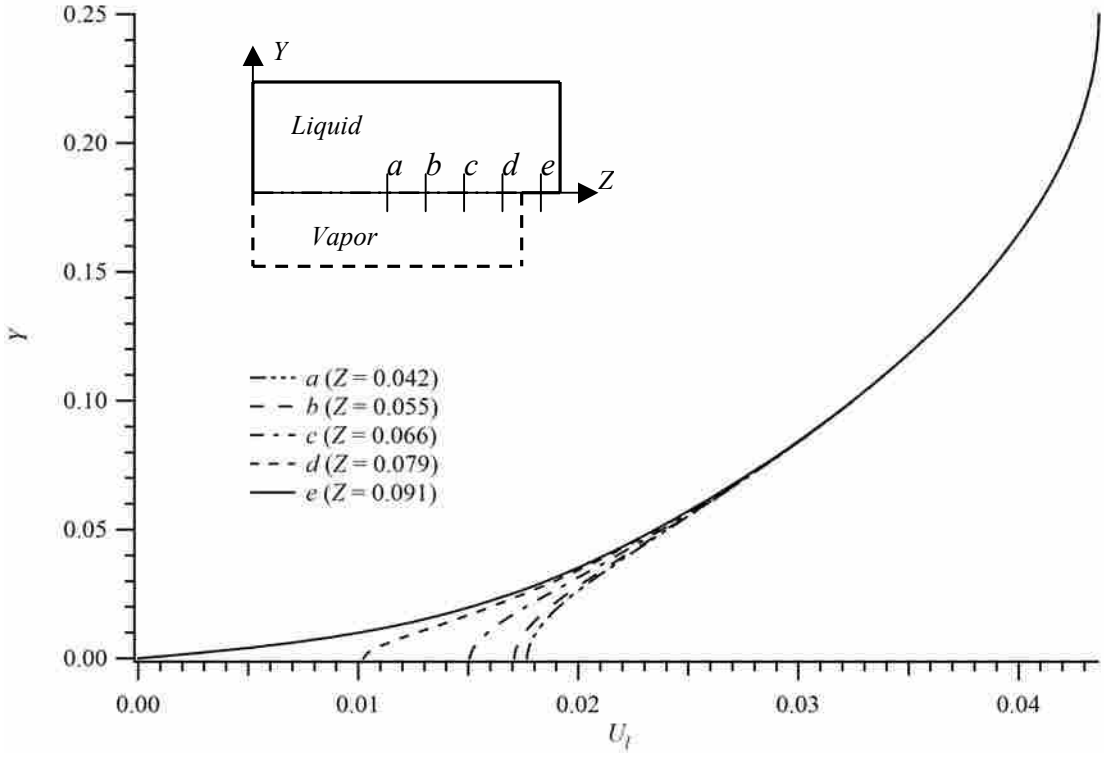

Figure 4-9 Nondimensional liquid velocity profiles as a function of the dimensionless wall-normal coordinate, *Y*, at various location in the transverse coordinate, *Z* for $W_m = 0.1$, $F_c = 0.88$, and $\delta_c = 0.1$ (see inset figure for the profiles relative positions)

Figure 4-10 illustrates three nondimensional weighted average liquid velocity profiles as a function of the wall-normal coordinate for a relative module width $W_m = 0.1$, a relative cavity depth of $\delta_c = 0.1$, and cavity fractions of $F_c = 0.5$, 0.88, and 0.97. It is observed that as the slip velocity increases with increasing cavity fraction, the average and maximum velocities are also increased. It has been stated in previous research as

well as in the current study that it is the existence of the slip velocity, and thus the increased average velocity, that creates the reduced pressure drop through such channels. Essentially, one could obtain a rough estimate of the enhanced flow dynamics of ultrahydrophobic channels by modeling a channel flow with a specified slip boundary condition based on an average slip velocity.

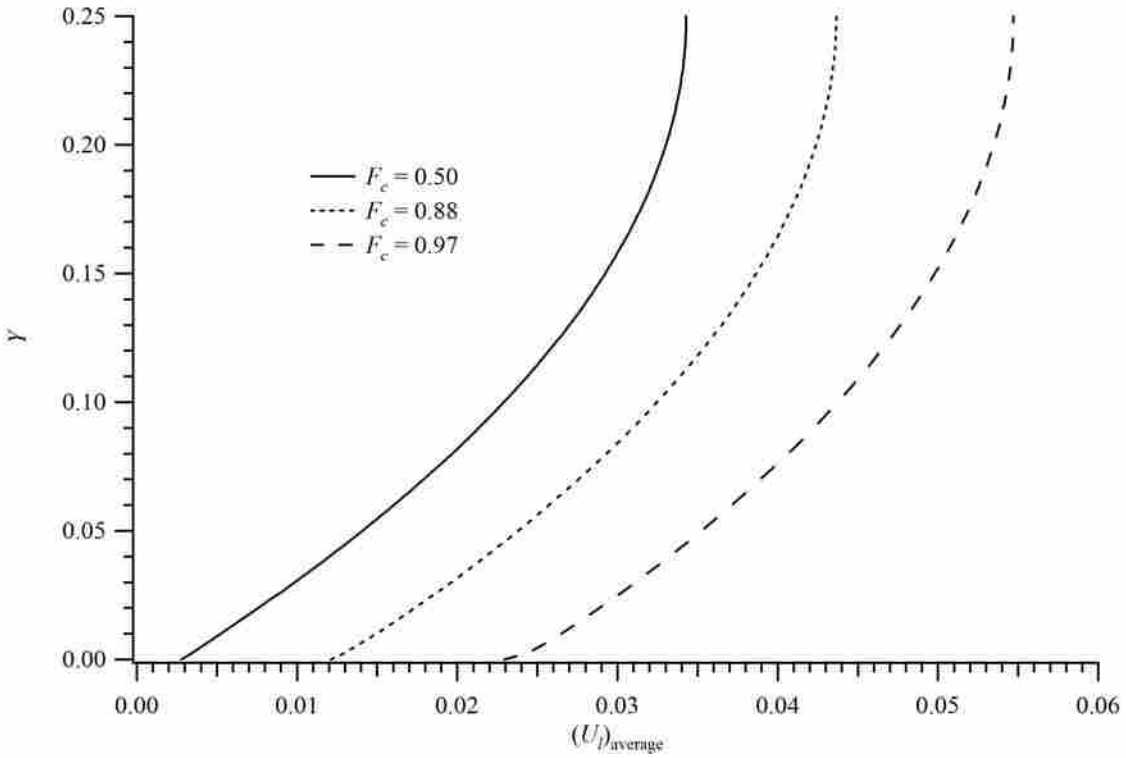

Figure 4-10 Weighted average nondimensional liquid velocity profiles as a function of the dimensionless wall coordinate, *Y*, for cavity fractions of F_c = 0.5, 0.88, and 0.97, and a relative cavity depth of δ_c = 0.1

4.3.1 Two-Dimensional Cavity Depth Study

A more extensive cavity depth study was conducted in conjunction with the two-dimensional vapor cavity model. Shown in Figure 4-11 are *fRe* predictions and in Figure 4-12 λ/W predictions as a function of the relative cavity depth, δ_c, for various values of

the relative module width and the cavity fraction. Also shown in the figures as small dotted lines are *fRe* and relative slip-length predictions for the zero shear stress model. As expected, *fRe* increases to a value of 96 and the effective slip-length decreases to 0 at a relative cavity depth of δ_c = 0 where the laminar no-slip channel flow behavior is approached. The figure also illustrates that the *fRe* predictions decrease as the relative vapor cavity depth increases. Further, as the relative cavity depth is increased the

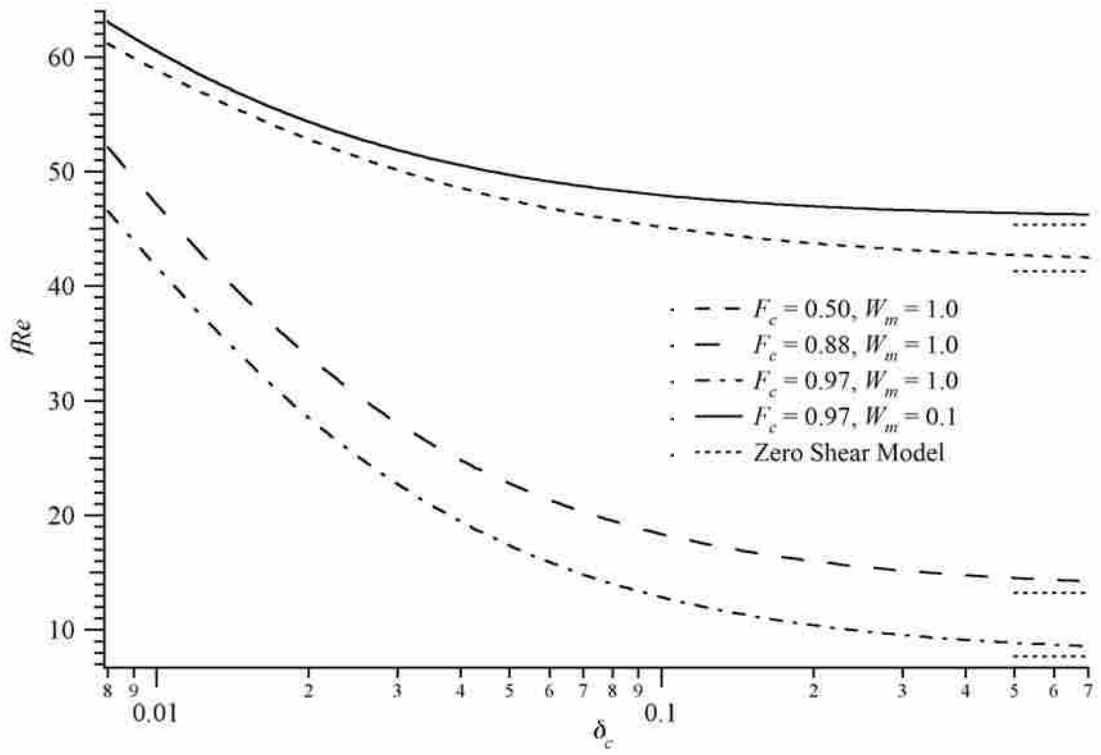

Figure 4-11 Predictions of *fRe* as a function of the relative cavity depth for multiple relative module widths and cavity fractions

magnitudes of *fRe* and λ/W are observed to become independent of the cavity depth, although when this occurs is dependent upon the cavity fraction. Therefore, to optimize the reduction in total frictional resistance or slip-length, the cavity depth should be set so

as to exceed this point. It is also observed for all scenarios that as the cavity depth is increased, the fRe and λ/W predictions approach the value obtained by the zero shear stress model. However, even at large relative cavity depths a small difference between the zero shear stress model and the two-dimensional coupled cavity model exists. In general, the vapor cavity depth has a greater influence on fRe and λ/W at higher values of F_c and W_m. The significant dependence of fRe and λ/W on the vapor cavity depth is further support to the conclusion that the zero shear stress model is inadequate in modeling the flow dynamics.

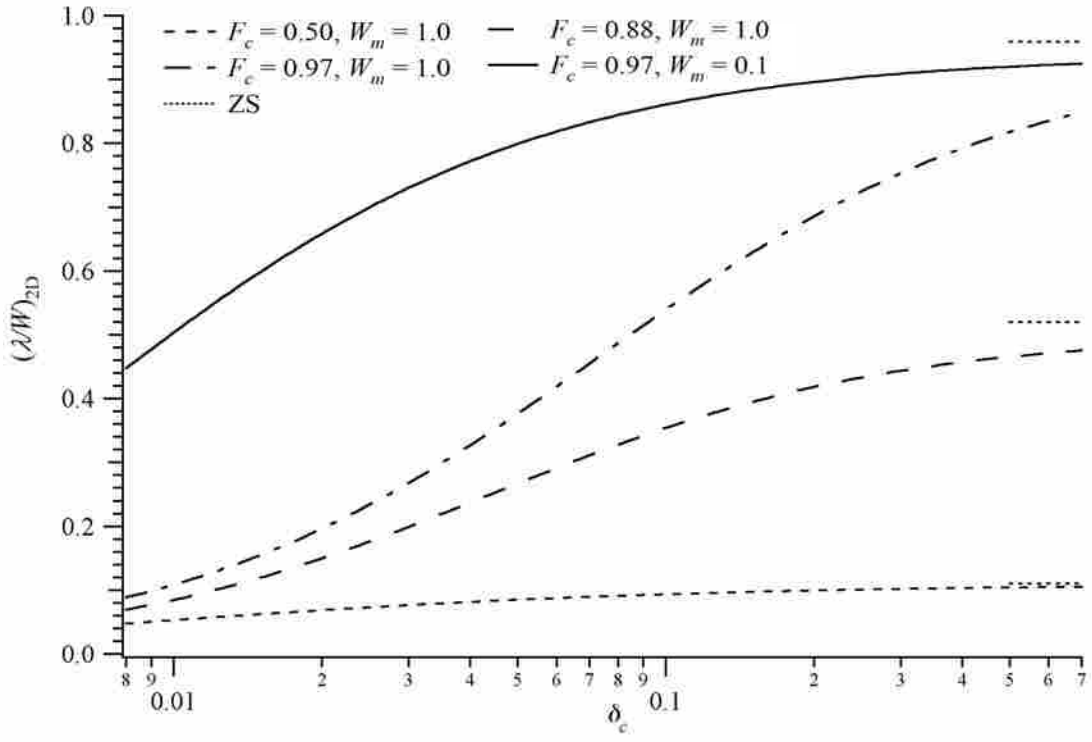

Figure 4-12 Slip-length predictions for the two-dimensional cavity model as a function of the relative cavity depth, δ_c for various cavity fractions and module widths

To illustrate the behavior of the vapor flow in the cavity, a simple code was written in Matlab™ to compute the cavity vapor velocity field using Equation 3-27. This code can be found in Appendix D. Contained in Figure 4-13 are nondimensional vapor velocity profiles as a function of the wall-normal coordinate, $\hat{Y}$, for the cavity fractions F_c = 0.5, 0.75, 0.88, 0.94, and 0.97, a module width of W_m = 0.1 and a relative cavity depth of δ_c = 0.1. Similarly, Figure 4-14 illustrates nondimensional vapor velocity profiles for the relative module widths W_m = 0.1, 0.5, and 1.0, for F_c = 0.97 and δ_c = 0.1

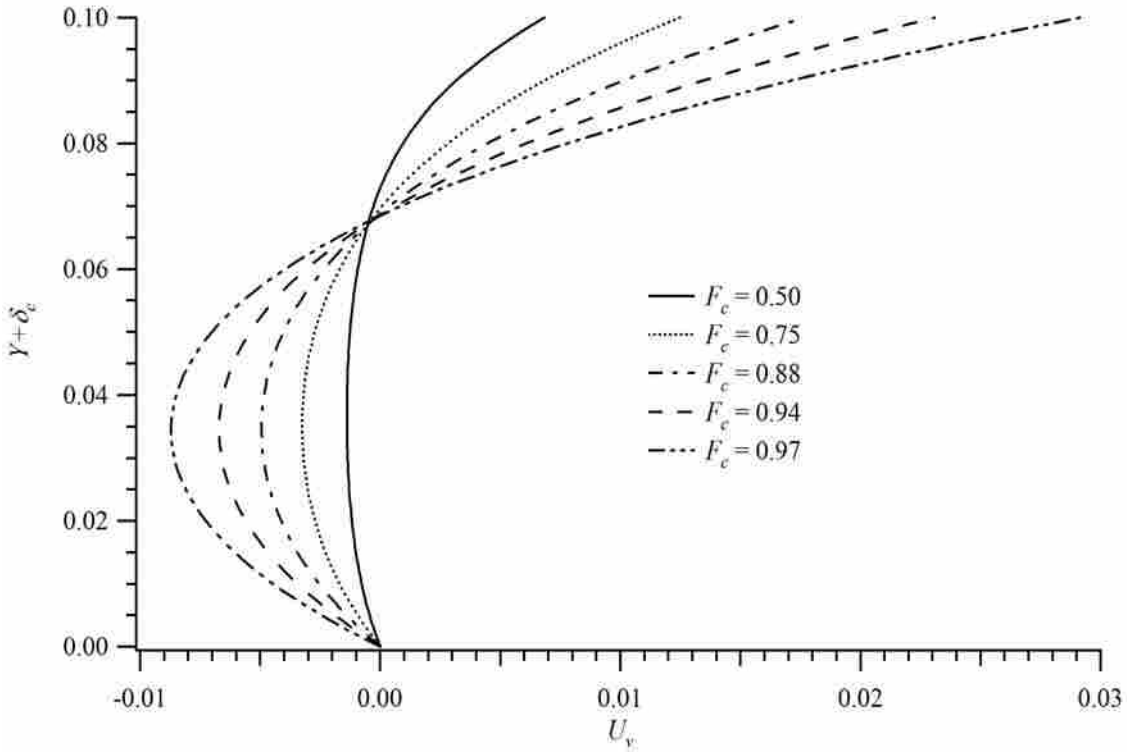

Figure 4-13 Dimensionless vapor velocity profiles at $Z = 0.5W_c$ as a function of the nondimensional wall normal coordinate, $\hat{Y} = Y + \delta_c$, measured from the bottom of the cavity for various cavity fractions and for W_m = 0.1 and δ_c = 0.1

also as a function of the wall-normal coordinate. The cavity wall-normal coordinate is measured from the bottom of the cavity and is defined as $\hat{Y} = Y + \delta_c$. Additionally, each profile in both figures represents the vapor velocity at the transverse centerline (Z = $0.5W_c$ and for $0 \le \hat{Y} \le \delta_c$) for each of the given scenarios. As the cavity fraction and the relative module width increase the interfacial velocity is also seen to increase, creating greater recirculation in the vapor cavity. This is in accordance with the observed trend in the previously presented *fRe* predictions where *fRe* were seen to decrease with increasing F_c and W_m due to the enhanced liquid interfacial velocity.

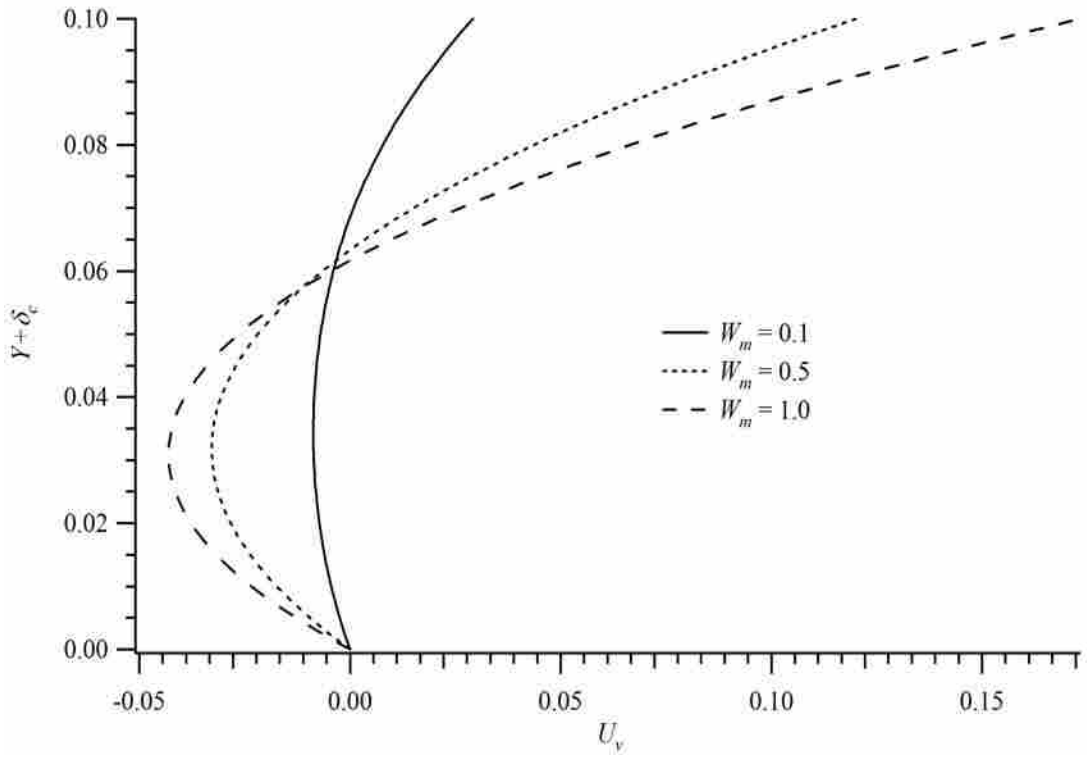

Figure 4-14 Dimensionless vapor velocity profiles as a function of the nondimensional wall normal coordinate, $\hat{Y} = Y + \delta_c$, measured from the bottom of the cavity for various module widths and for F_c = 0.97 and δ_c = 0.1

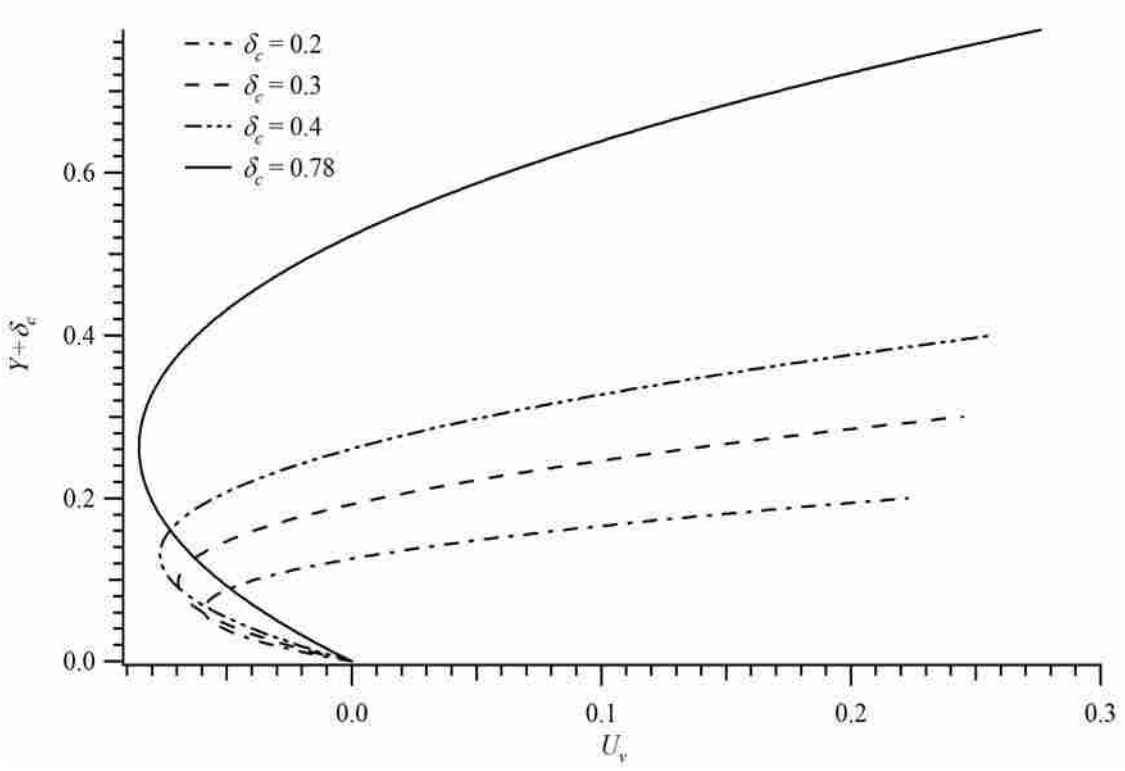

Figure 4-15 Dimensionless vapor velocity profiles as a function of the nondimensional wall-normal vapor cavity coordinate for various relative cavity depths and for W_m = 0.1 and F_c = 0.97

It is further observed in both Figure 4-13 and Figure 4-14 that as the cavity fraction increases the vapor velocity gradient at $\hat{Y} = 0$ increases, causing the shear stress at the vapor-solid boundary to increase. This suggests the possibility that a larger cavity depth could provide the same recirculation vapor velocity while maintaining a smaller magnitude of the near wall velocity gradient and wall shear (this effect can be observed if one were to stretch the figures in the vertical direction). This phenomenon is better illustrated in Figure 4-15. Presented are nondimensional vapor velocity profiles as a function of the normalized wall normal coordinate, $\hat{Y}$. Data is represented for various values of the relative cavity depth at F_c = 0.97 and W_m = 1.0. It is observed that the interface velocity and the recirculation velocity in the vapor cavity both increase as the

cavity depth increases, while simultaneously maintaining a smaller near wall velocity gradient at $\hat{Y} = 0$. A smaller near-wall gradient results in less frictional resistance in the cavity and therefore, less momentum is lost. For this reason greater reductions of the total frictional resistance in the liquid channel occur for increasing values of the cavity depth as shown in the cavity depth study.

4.3.2 Two-Dimensional Cavity Correlation

Results from the coupled cavity models indicate that the friction factor-Reynolds number product depends strongly on the cavity depth, δ_c, in addition to the relative module width, W_m, and the cavity fraction, F_c. The overall behavior is for fRe to decrease

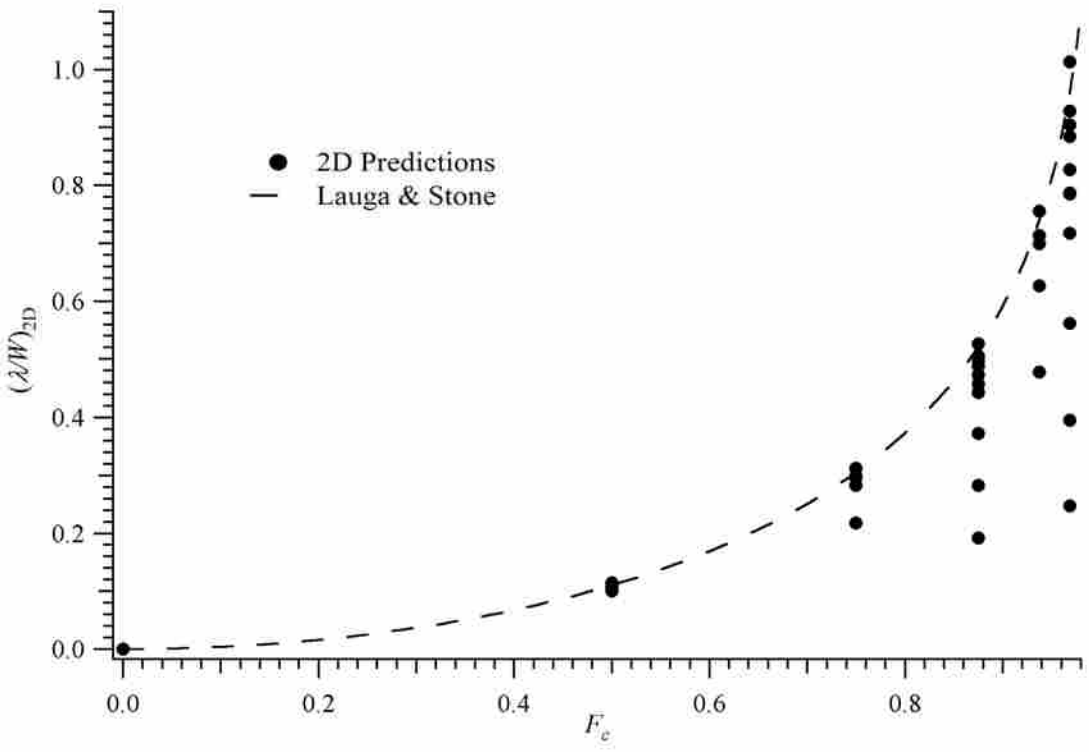

Figure 4-16 Normalized slip length prediction using the two-dimensional cavity model compared to the analytical expression developed my Lauga & Stone, Equation 3-12

with increasing δ_c, W_m, and F_c. The development of an expression that can accurately predict the *fRe* value as a function of all the relevant dimensionless parameters would prove very beneficial, since Equation 3-12 and 3-13 are not adequate for the coupled cavity problem. Figure 4-16 presents the two-dimensional cavity model predictions of the normalized slip length in comparison to the expression developed by Lauga and Stone [26] (Equation 3-12). An examination of the figure reveals an additional dependence beyond the relative module width and the cavity fraction. Analysis of the numerical predictions reveals that this additional dependence can be accounted for by including the depth of the vapor cavity. It was found that the predicted *fRe* shows an exponential dependence on the ratio of cavity depth to height. A regression analysis indicates that Equation 3-12 can be modified to account for the observed dependence on the vapor cavity depth. Doing so provides the following updated correlation for the normalized slip length.

$$\left(\frac{\lambda}{W}\right)_{2D} = \frac{1}{\pi}\ln\left(\frac{1}{\cos\left(F_c\pi/2\right)}\right)\left(1-e^{\frac{-4\delta_c^{2/3}}{W_c}}\right) \qquad \textbf{(4-1)}$$

Combining the above expression with Equation 3-11 results in a predictive correlation based on the observed physics for *fRe* as a function of all the relevant dimensionless parameters.

$$f\,\mathrm{Re}_{2D} = \frac{8}{\left[\frac{1}{\pi}\ln\left(\frac{1}{\cos(F_c\pi/2)}\right)\left(1-e^{\frac{-4\delta_c^{2/3}}{W_c}}\right)W_m + \frac{1}{12}\right]} \qquad \textbf{(4-2)}$$

A comparison between the numerically predicted *fRe* values and those obtained using the above expression is shown in Figure 4-17. In this figure the numerical predictions are shown as dots and the analytical expression as the solid line. As demonstrated by the data, excellent correlation exists between the *fRe* values obtained in the numerical study and those calculated using Equation 4-2.

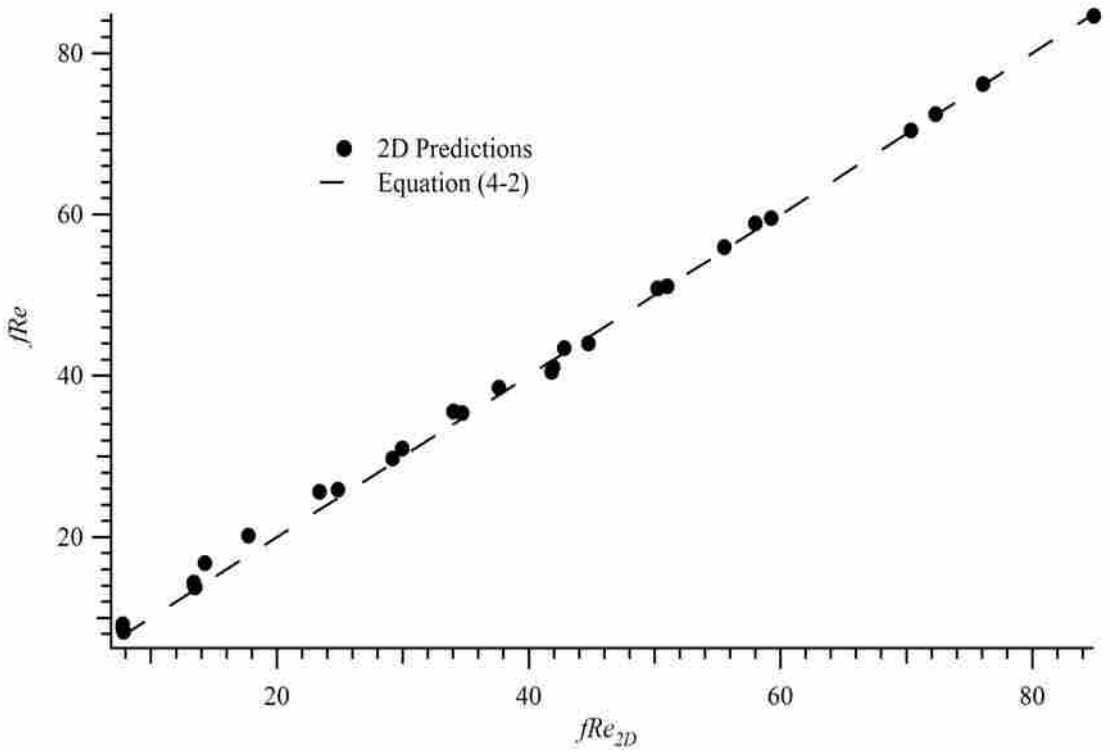

Figure 4-17 Comparison between *fRe* predictions from the two-dimensional cavity model and those obtained using Equation 4-2

4.3.3 Comparison to Experimental Data

A comparison between numerically predicted and experimentally measured values of *fRe* is shown in Figure 4-18, as a function of the cavity fraction, F_c. The experimental measurements provided by Woolford et al. [30] are for relative module width values of W_m = 0.13 and 0.26 and were taken at cavity fraction of $F_c \approx$ 0, 0.48, 0.69, 0.79, 0.84, and 0.91. The numerical predictions illustrated represent relative module width values of W_m = 0.1 and 0.25 and a relative cavity depth of δ_c = 0.1. Both the numerical predictions and the experimental measurements show the same trend and dependence on the cavity fraction. At a cavity fraction of zero, both the model and the experimental work match the classic no-slip channel value of 96. However, as the cavity fraction increases the numerical predictions are observed to predict lower *fRe* values than are measured experimentally. This discrepancy can be attributed to some of the assumptions made in the numerical model. For the numerical two-dimensional cavity model the entrance effects were neglected and the liquid-vapor interface was considered as a flat, each of which would contribute to increasing the total frictional resistance. Further, the liquid channel was modeled as infinitely wide parallel plates, whereas the experimental data was calculated using measurements from a rectangular channel. Therefore, neglecting the side effects of the channel may have also contributed to the observed discrepancy between the numerical predictions and the experimental data.

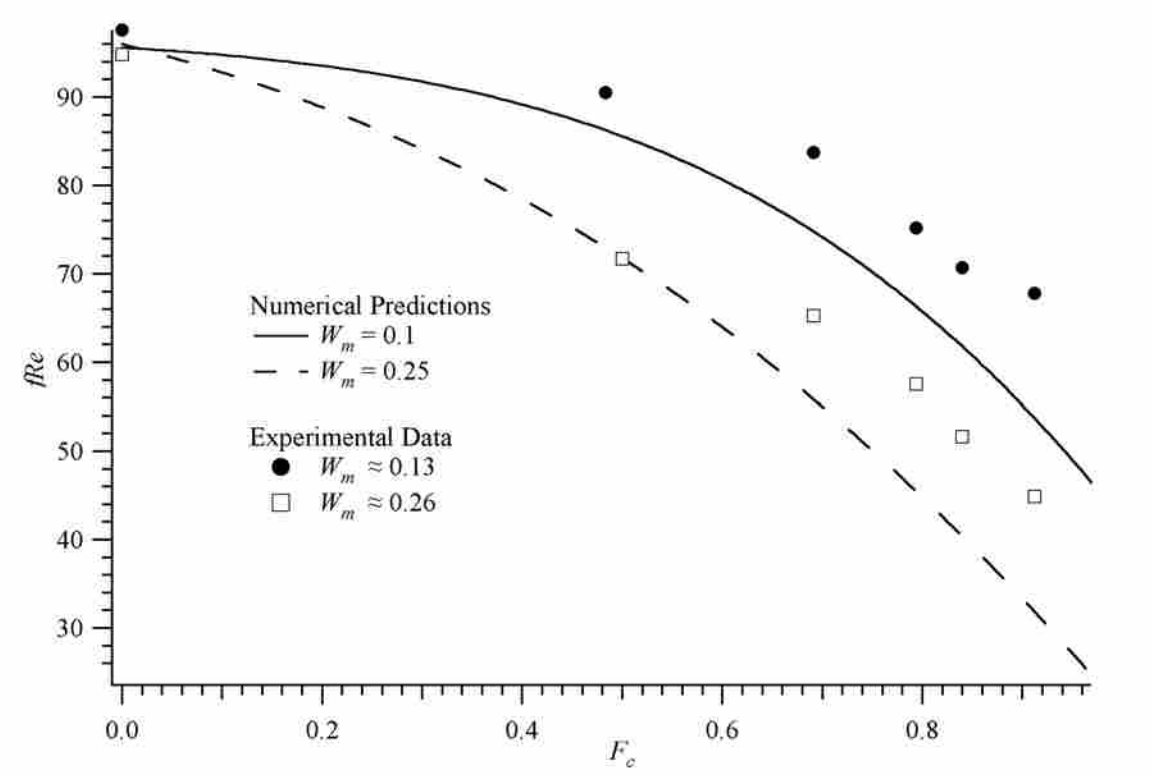

Figure 4-18 Comparison of *fRe* predictions to experimental data obtained from Woolford et al. as a function of the cavity fraction and for the relative module widths of 0.1 and 0.25

5 Turbulent Flow Results

5.1 Model Validation

Contained in Table 5-1 are values of the Darcy friction factor computed in the current numerical study for turbulent smooth-channel flow and the values provided by the Blasius [46], Beavers et al. [48], and Dean [49] correlations. A Reynolds number range from 2,000-10,000 is presented in the table. Good agreement between the values can be seen for Reynolds numbers above 4,000, providing adequate validation for the presented numerical study. The poor agreement for Reynolds numbers below 4,000 can be attributed to the fact that transition is still occurring and is below the suggested range for the presented correlations.

Table 5-1 Darcy friction factor predictions compared to calculated values from published correlations as a function of the Reynolds number

Re	*f*			
	Predicted	**Blasius [46]**	**Beavers et al. [48]**	**Dean [49]**
2,000	0.075	0.052	0.052	0.052
4,000	0.053	0.044	0.042	0.044
6,000	0.044	0.040	0.037	0.039
8,000	0.038	0.037	0.034	0.037
10,000	0.035	0.035	0.032	0.035

In the current study three values of the relative module width were examined, W_m = 0.01, 0.1, and 1.0. For the smallest value of the relative module width it became necessary to increase, from that used for the other values of module width, the number of nodes in the transverse direction to provide for a grid-independent solution. As this was accomplished, while simultaneously maintaining the nearest wall node at approximately $y^+ = 1$ (see Section 3.2), cells with aspect ratios of up to ten were created at the lower boundary ($y = 0$). For assurance of accurate results it is typically recommended that the aspect ratio be kept as close to a value of one as possible. A quick test was employed to verify that these larger aspect ratios did not induce significant error into the W_m = 0.01 solutions. Since the classical no-slip channel solution is not dependent upon the module width, friction factor predictions were computed for the same Reynolds number at all three relative width values. The results of this study are presented in Table 5-2 for a no-slip parallel plate flow at a Reynolds number of Re = 8,000. It can be observed from the table that a 2.6% difference exists between the predicted friction factors from the two higher values to the lowest value of W_m = 0.01. Although it is not understood how varying the cavity fraction may influence this small error, there has been no indication that it has increased significantly.

Table 5-2 Friction factor predictions for the classical no-slip parallel plate channel flow for Re = 8,000 and module widths of W_m = 0.01, 0.1, and 1.0

Re = 8,000	
W_m	f
1.0	0.038
0.1	0.038
0.01	0.039

5.2 Turbulent Flow Results

Illustrated in Figure 5-1 are Darcy friction factor predictions as a function of the Reynolds number for a relative module width of $W_m = 0.1$ and for the cavity fractions of $F_c = 0$, 0.5, 0.75, 0.88, 0.94, and 0.97. The solid line in the figure represents the friction factor predictions for the classical no-slip parallel plate channel flow, and therefore becomes the benchmark from which reductions in the frictional drag may be measured.

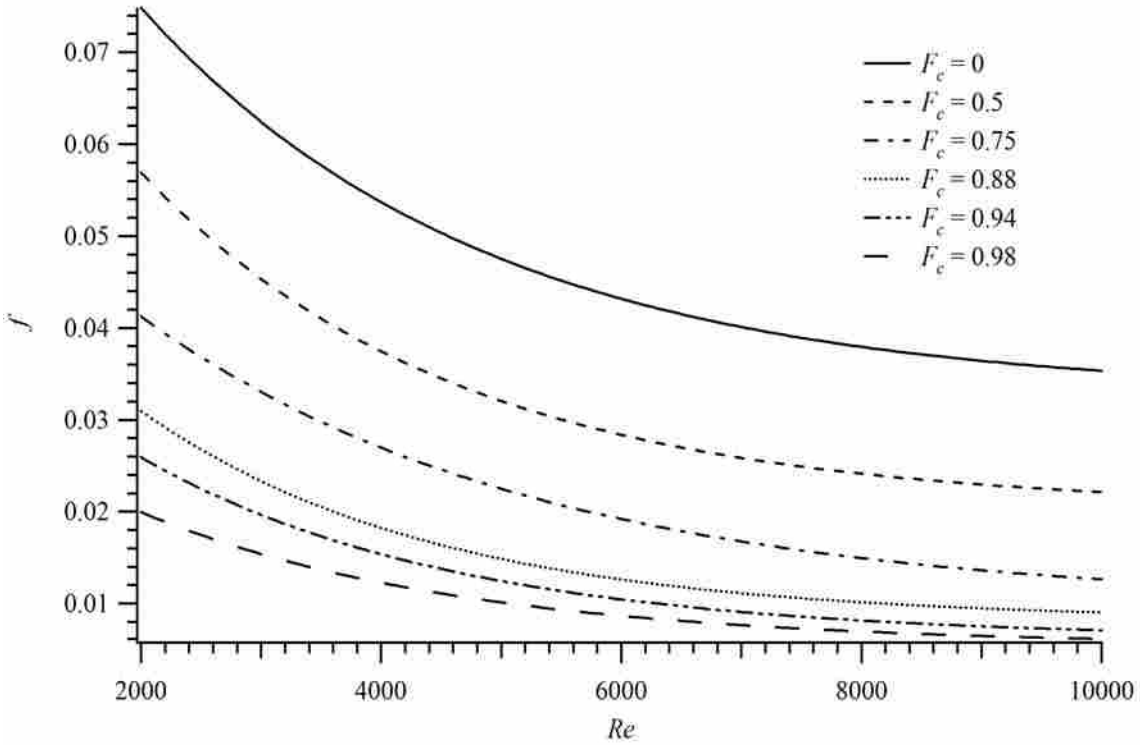

Figure 5-1 Friction factor predictions as a function of Reynolds number for a relative module width of $W_m = 0.1$ and for cavity fractions of $F_c = 0$, 0.5, 0.75, 0.88, 0.94, and 0.97

It is observed from Figure 5-1 that as the Reynolds number increases the friction factor decreases, as expected. However, it can also be observed from the figure that the dependence of the friction factor on the Reynolds number also decreases for increasing

values of the Reynolds number. It can be speculated that very little difference would exist between the predictions given at a Reynolds number of 10,000 to those of a higher Reynolds number. For a cavity fraction of F_c = 0.94 there is a 46% decrease in the friction factor from a Reynolds number of 4,000 to 8,000; whereas only a 13% decrease occurs from 8,000 to 10,000. This leads to the hypothesis that for a given cavity fraction and module width, little advantage may be gained in terms of reducing the frictional resistance beyond a certain Reynolds number. However, further investigation of higher Reynolds numbers would be required before any sure conclusions could be made.

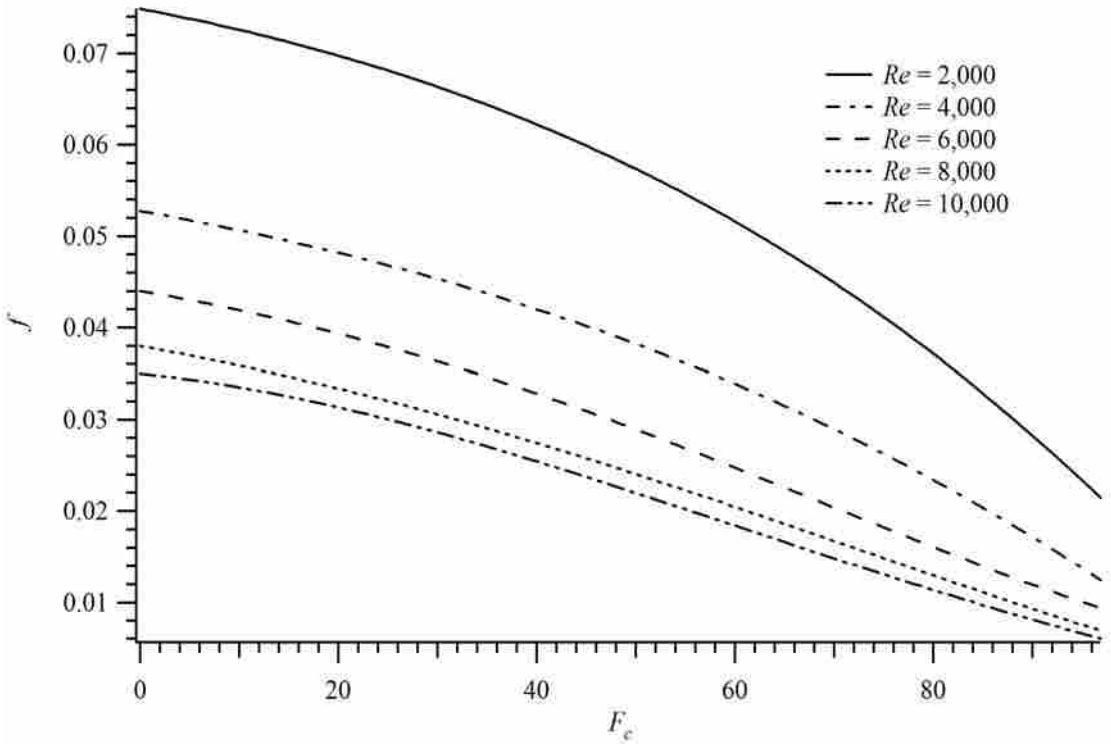

Figure 5-2 Friction factor predictions as a function of the cavity fraction for a relative module width of W_m = 0.1 and for the Reynolds numbers *Re* = 2,000, 4,000, 6,000, 8,000, and 10,000

Figure 5-2 exhibits friction factor predictions as a function of the cavity fraction for the relative module width of W_m = 0.1, at the Reynolds numbers of Re = 2,000, 4,000, 6,000, 8,000, and 10,000. In this figure, a cavity fraction of F_c = 0 represents the classical no-slip parallel plate channel value from which the measurements of drag reduction are to be based. An examination of this figure reveals the same trend that was observed in the laminar flow data. As the cavity fraction increases, the reduction in the total frictional resistance decreases. For turbulent flow data presented, a reduction in frictional resistance is indicated by the reduction in the friction factor predictions. The turbulent flow simulations show reductions of 24% for a cavity fraction of F_c = 0.5 and a relative module width of W_m = 0.1 and of 75% for the same module width but a cavity fraction of F_c = 0.97. As discussed in the previous chapter, this trend in the predictions is due to the increased region of zero shear stress as the cavity fraction increases. As this region of reduced shear stress increases so does the influence it has on the dynamics of the channel flow.

The turbulent flow predictions also show the same dependence on the relative module width as observed for laminar flow. Presented in Figure 5-3 are friction factor calculations as a function of the Reynolds number for a cavity fraction of F_c = 0.88, and for the relative module widths of W_m = 0.01, 0.1, and 1.0. A study of the figure reveals, as expected, that the predicted friction factor decreases with increasing relative module width. At a Reynolds number of 8,000 and a cavity fraction of F_c = 0.88 the turbulent simulations calculate a friction factor of f = 0.027 for a relative width of W_m = 0.01 and f = 0.01 for a relative width of W_m = 0.1, a reduction of 63%. This is a result of the larger module width case having a larger cavity in relation to the channel height in comparison

to that of a smaller module width value, as discussed previously. However, examination of the results also shows that the magnitude of the reduction of frictional drag is much more significant for the lower values of the relative module width. For a cavity fraction of 0.88, from a Reynolds number of Re = 2,000 to 10,000, the magnitude of the friction factor is reduced by 0.029 for a relative width of W_m = 0.01 compared to 0.004 for a width of W_m = 1.0. Although, it is interesting to note that the percent reduction is the same for both of the examples given, at approximately 54%.

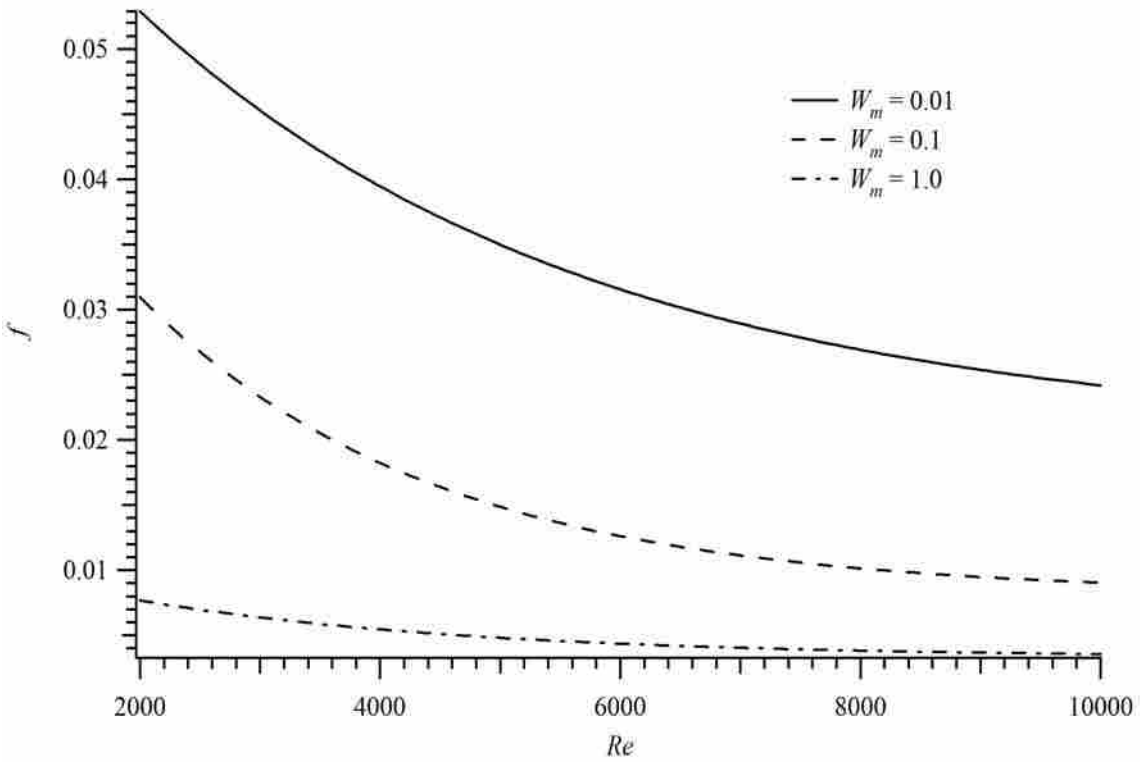

Figure 5-3 Friction factor predictions as a function of the Reynolds number for the cavity fraction of F_c = 0.88 and for the relative module widths of W_m = 0.01, 0.1, 1.0

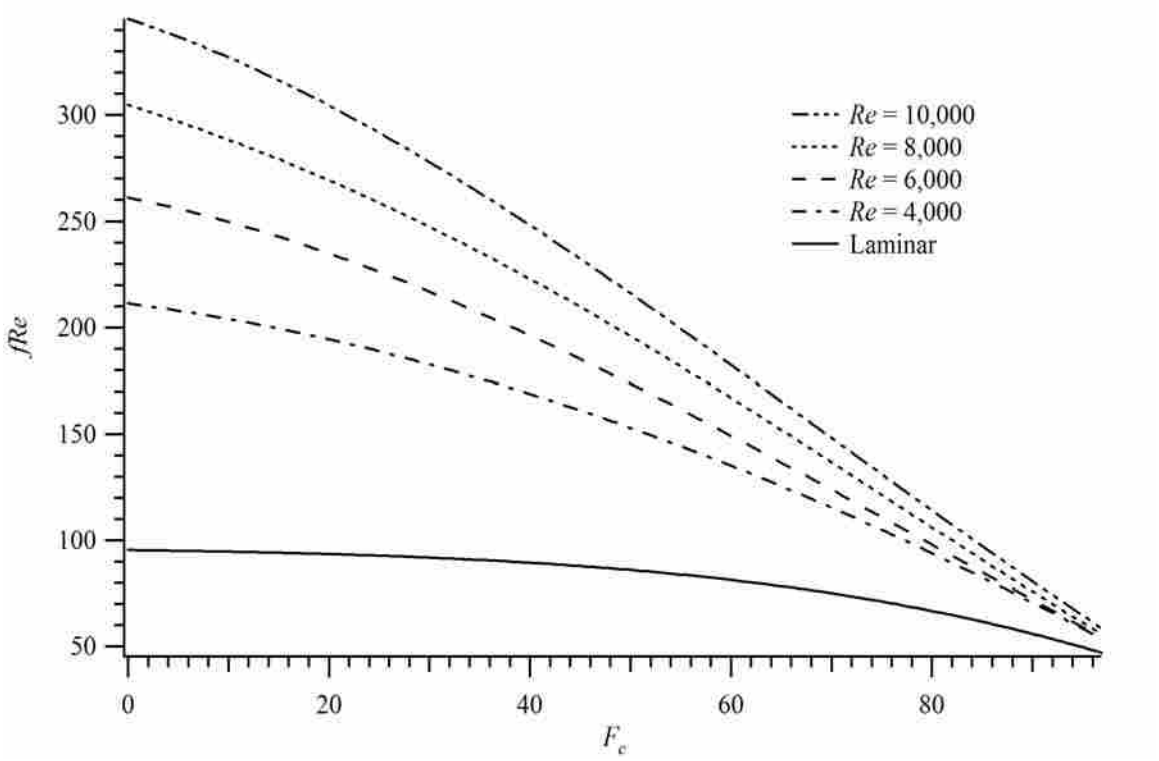

Figure 5-4 Predictions of *fRe* as a function of the cavity fraction for a relative module width of W_m = 0.1 for both turbulent flow, at various Reynolds numbers and for laminar flow

Plotting the predictions from the turbulent flow simulations as a function of the cavity fraction, as in Figure 5-2, also permits a comparison to the laminar flow predictions. Figure 5-4 contains *fRe* calculations as a function of the cavity fraction for a relative module width of W_m = 0.1 and for the Reynolds numbers Re = 4,000, 6,000, 8,000, and 10,000. The solid line in the figure represents the laminar flow predictions which are independent of the Reynolds number. A cavity fraction of F_c = 0 represents the classical no-slip channel flow, where the laminar flow predictions can be seen at the value of 96. Viewing the predictions in this manner illustrates how much greater the reduction in frictional drag occurs for the turbulent channel flow. For a Reynolds number of Re = 10,000 and a relative module width of W_m = 0.1, an 82% reduction is observed

from a cavity fraction of F_c = 0 to 0.97, whereas only a 54% reduction occurs in the laminar flow predictions for the same relative module width. Further, for the relative module width displayed in Figure 5-4, W_m = 0.1, the reduction in the turbulent flow predictions are so large that the value drops below the classical no-slip laminar flow value. For the relative module width displayed in Figure 5-4 at a cavity fraction of F_c = 0.97, the friction factor predictions are in the range of fRe = 41-58 for the given Reynolds number values.

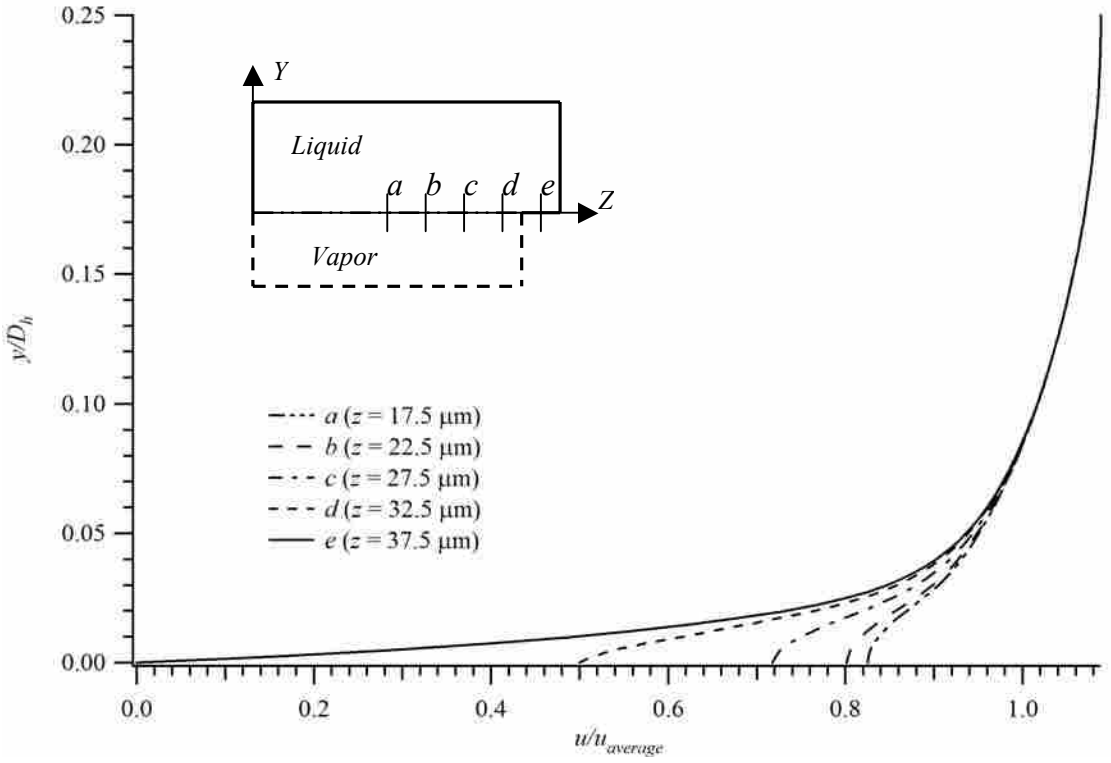

Figure 5-5 Normalized liquid velocity values, $u/u_{average}$, as a function of the dimensionless wall-normal coordinate, $Y=y/D_h$ at various transverse locations for W_m = 0.1, F_c = 0.88, and Re = 10,000

Contained in Figure 5-5 are normalized liquid velocity profiles, $u/u_{average}$, as a function of the normalized wall-normal coordinate, y/D_h. Represented are velocity

predictions for W_m = 0.1, F_c = 0.88, and Re = 10,000. The liquid velocity is normalized by the average velocity for the entire liquid domain, and the wall-normal coordinate by the channel hydraulic diameter. The inset figure illustrates the relative location of each of the profiles. The locations labeled *a* and *e* represent the center of the vapor cavity and the solid rib, respectively. Satisfying the no-slip condition, the liquid velocity approaches zero at the liquid-solid boundary. As with the laminar flow predictions, an increase in the slip-velocity (non-zero liquid velocity at the wall, $Y = 0$) occurs as one progresses to the vapor cavity center where a maximum value is obtained. As expected, the turbulent flow predictions show a larger near wall velocity gradient then that of the laminar flow velocity profiles presented in Figure 4-9. Using the turbulent flow velocity profile data in the same way as done previously with the laminar flow data, one can calculate the weighted average velocity profile for the entire liquid domain. This is illustrated in Figure 5-6, where averaged normalized velocity predictions are plotted as a function of the normalized wall-normal coordinate at cavity fractions of F_c = 0.5, 0.88, and 0.97, for W_m = 0.1 and Re = 10,000. Each line represents an area weighted average velocity for the entire liquid domain at the respective cavity fraction. It is interesting to note that as the slip velocity increases with increasing cavity fraction that the maximum velocity decreases. Since each of these simulations is for the same value of the Reynolds number, they each were specified with the same constant mass flow rate and thus the same average velocity. Therefore, in order to maintain the same average velocity, the maximum velocity must increase to accommodate an increased slip velocity.

Examination of Figure 5-6 allows a rough prediction of the average slip-lengths for the given turbulent flow scenarios. Extending the near-wall velocity gradient to the vertical axis one can obtain a crude estimate of the relative slip-length.

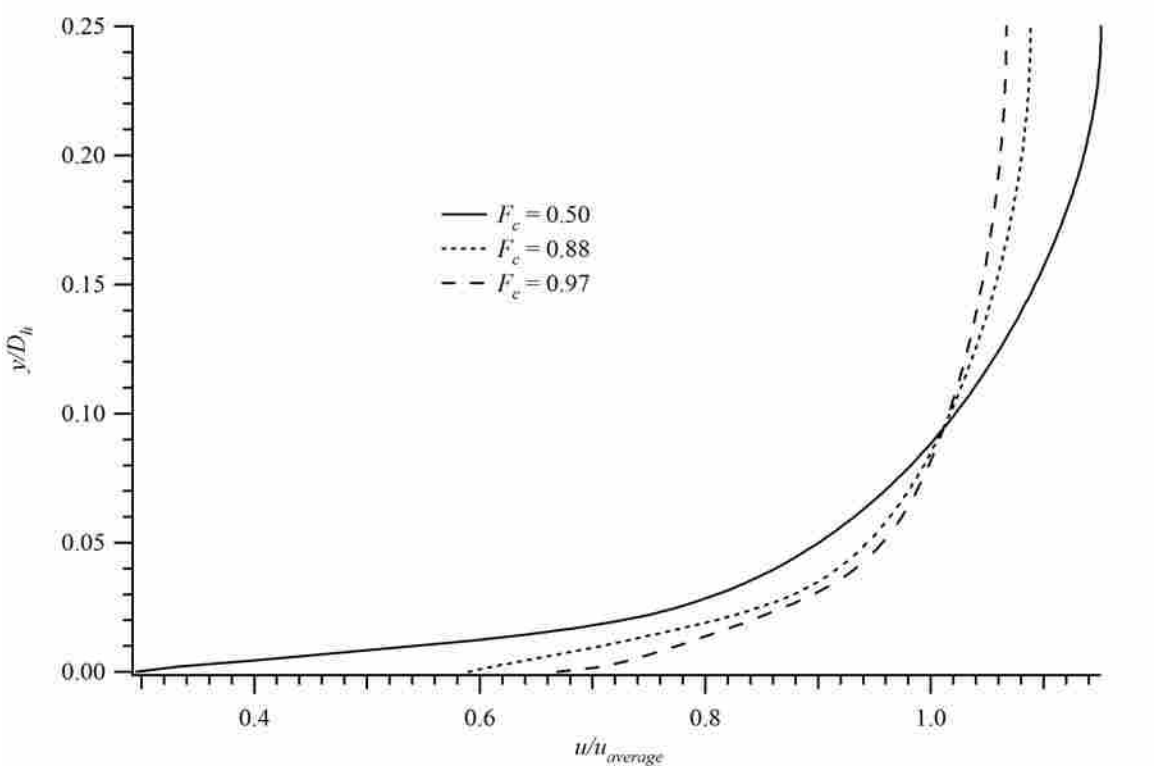

Figure 5-6 Average normalized liquid velocity profiles, $u/u_{average}$, as a function of the dimensionless wall-normal coordinate, $Y=y/D_h$ at F_c = 0.5, 0.88, 0.97, for W_m = 0.1 and Re = 10,000

5.2.1 Turbulent Flow Correlation

As previously observed, the turbulent flow predictions are highly dependent on the Reynolds number. Correlations have been developed previously by researchers to calculate the friction factor as a function of the Reynolds number. Examination of the

numerical data for the no-slip channel flow from the current study reveals the following correlation for the friction factor.

$$f = \frac{3.4}{\sqrt{\mathrm{Re}}} \tag{5-1}$$

It is recognized that this presented correlation demonstrates a substantially different dependence on the Reynolds number than those referenced earlier (Equations 3-51 to 3-53). This is due to the fact that Equation 5-1 was developed for a Reynolds number range of Re = 2,000 to 10,000, which is much lower than the recommended range of the referenced correlations, and thereby results in a different power law dependence. It is also important to note that a Reynolds number of Re = 2,000 is still within the laminar to turbulent flow transition region.

Further analysis of the turbulent flow numerical data revealed the same dependence on the relative module width and cavity fraction for the turbulent flow predictions as was observed for the laminar flow predictions. In addition, an examination of Equation 3-13 shows that for a no-slip channel, F_c = 0, the left hand side of the denominator vanishes and only the constant coefficients 8 and 1/12 remain, which finally reduce to fRe = 96. Based on this observation, it was assumed that to include a Reynolds number dependence, the constants 8 and 1/12 in Equation 3-13 would require modification so that for F_c = 0, the expression would reduce to Equation 5-1. Performing this adaptation reveals the following expression.

$$f = \frac{6}{\mathrm{Re}\left[\frac{1}{\pi}\ln\left(\frac{1}{F_c\pi/2}\right)W_m + \frac{1.82}{\sqrt{\mathrm{Re}}}\right]} \qquad \textbf{(5-2)}$$

The above expression can then be used to predict the friction factor as a function of the relative module width, W_m, the cavity fraction, F_c, and the Reynolds number, Re. Figure 5-7 contains numerical predictions of the friction factor in comparison to the values calculated using Equation 5-2. In the figure the dots indicate the numerically predicted values and the solid line represents the analytical expression. The numerical predictions shown are for a range of relative module widths of W_m = 0.01-1.0, cavity fraction of F_c = 0-0.98, and for the range of Reynolds number Re = 2,000-10,000. It is observed from the figure that the analytical expression fits the trend of the data well. Those data points showing the largest variation from the Equation 5-2 tend to be for Re = 2,000, which as previously stated, is still within the laminar to turbulent flow transitions region. However, the average difference between the numerical and analytical values is approximately 25%. It is therefore recommended that use of Equation 5-2 to predict the friction factor be limited to initial estimates only.

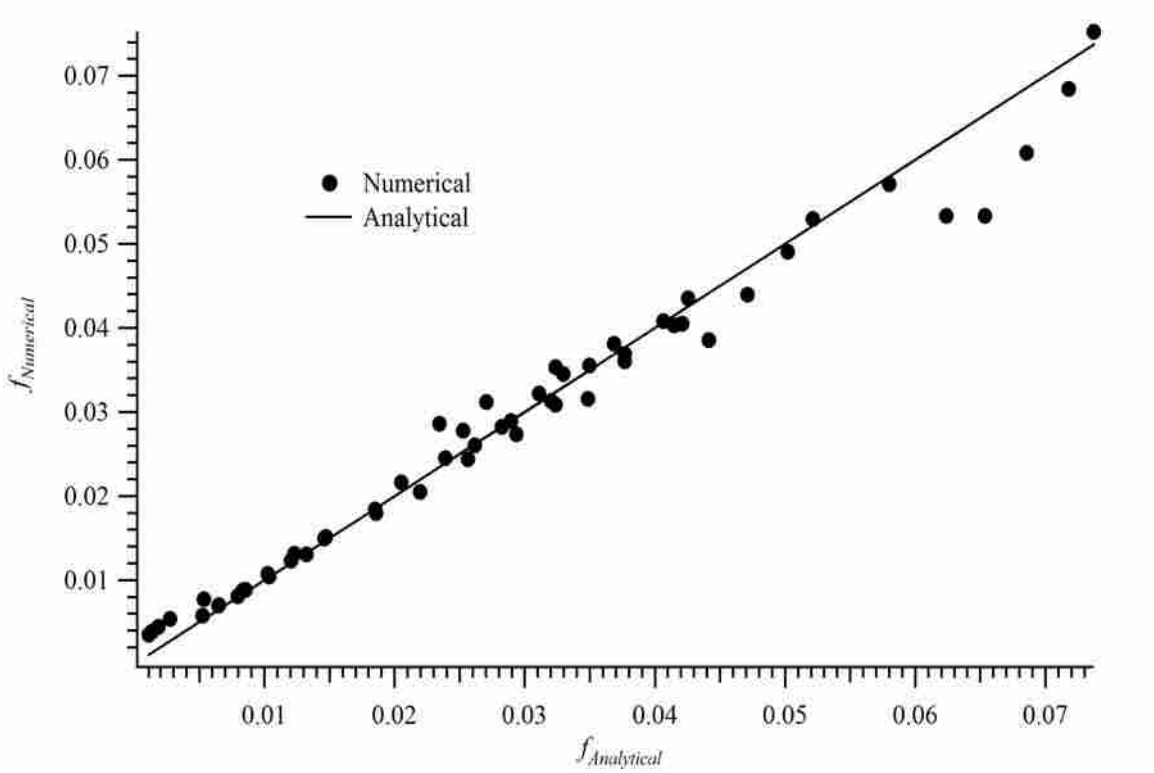

Figure 5-7 Numerical predictions of the friction factor compared to those calculated using Equation 5-2 for the range of module widths W_m = 0.01-1.0, cavity fractions F_c = 0-0.98, and Reynolds numbers Re = 2,000-10,000

6 Conclusions

Due to the increase of application in a number of emerging technologies, a growing amount of research has focused on the reduction of drag in microfluidic transport. A novel approach reported in the recent literature is to fabricate micro-ribs and cavities in the channel wall that are then treated with a hydrophobic coating. Such surfaces have been termed superhydrophobic and the contact area between the flowing liquid and the solid wall is greatly reduced. Further, due to the scale of the microscaled structures, the liquid is unable to wet the cavity and a liquid meniscus is formed between ribs. Reported in this thesis is the numerical study of fully developed laminar and turbulent flow through a parallel plate channel with walls exhibiting micro-ribs and cavities oriented parallel to the flow direction.

Various laminar flow models are implemented to investigate the liquid-vapor interface and to include the effects of the vapor motion in the cavity regions. It was observed that the fRe decreases with increasing W_m and F_c. Reductions in fRe as high as 92% were observed for a relative module width of $W_m = 1.0$ and a cavity fraction of $F_c = 0.97$. The numerical prediction produced using the zero shear stress model were shown to correlate very well with the analytical model developed by Lauga and Stone for the normalized slip length. However, it was concluded that the zero shear stress model is inadequate in terms of accounting for the actual physics at the liquid-vapor interface and

is therefore an idealization. The one and two-dimensional vapor cavity models account for the non-zero interfacial shear stress by modeling the vapor cavity in progressing levels of rigor. These models reveal a significant dependence of *fRe* on the vapor cavity dimensions and therefore more accurately represent the true physics. For the example given earlier, the two-dimensional cavity model shows a reduction of 87% (for a cavity fraction of δ_c = 0.1) as opposed to the 97% reduction given by the zero shear stress model. A cavity depth study was performed where it was observed that *fRe* decreases with increasing δ_c. Further, the dependence of *fRe* was seen to decrease with increasing δ_c, where less than a 2% difference exists from a cavity depth of δ_c = 0.4-0.7. Returning to the example given, if the cavity fraction is increased to a value of δ_c = 0.7, the predicted reduction increases to 91%. Finally, a laminar flow correlation was developed based on the numerical predictions which allows for the prediction of the friction factor-Reynolds number product as a function of the relevant dimensionless parameters, W_m, F_c, and δ_c. Agreement between the numerical and analytical predictions is found to be very good.

In the turbulent flow model the liquid-vapor interface is idealized as a flat interface with a zero shear stress boundary condition. The numerical predictions show the same dependence on both the relative module width and the cavity fraction as observed in the laminar flow models; that is, the frictional resistance decreases with increasing W_m and F_c. It is also shown that the predicted friction factor value for turbulent flow is reduced with increasing Reynolds numbers. For the range of parameters explored, reductions in the friction factor were found to be as high as 90% for a relative module width of W_m = 1.0, a cavity fraction of F_c = 0.88, and at a Reynolds number of *Re*

= 10,000. It was also observed that for the same value of the relative module width and cavity fraction, the turbulent flow results indicated a greater reduction in flow resistance than for the laminar flow. An analytical relationship is also proposed for the turbulent flow regime where the friction factor can be predicted as a function of the relevant dimensionless parameters. Use of the developed analytical expression shows an average error of approximately 29% and is therefore recommended for use only as an initial estimate.

It is recommended that further work should be made to correlate the numerical predictions with the previously published experimental measurements. This could be accomplished by accounting for the developing boundary layer at the channel entrance, as well as for the influence of the side walls of the channel. It is also recommended that the turbulent flow study be continued for higher Reynolds numbers. It is assumed that the 1/2 power law in Equation 5-1 is a result of a low Reynolds number range where transition may be occurring (Re = 2,000-4,000). It is possible that a study including Reynolds number higher than those examined in the current work would reveal a more typical turbulent power law, such as 1/5 or 1/7, and therefore lead to the development of a more accurate predictive correlation. Further, the use of a turbulent model other than a RANS model could lead to a more complete understanding of the influence ultrahydrophobic surfaces may have on turbulent flow dynamics.

7 References

[1] H. A. Stone, A.D. Stroock, and A. Ajdari, "Engineering Flows in Small Devices: Microfluidics Toward a Lab-on-a-Chip," *Annual Review of Fluid Mechanics*, **36**, 381-411 (2004).

[2] V. Singhal, S. Garimella, A. Raman, "Microscale Pumping Technologies for Microchannel Cooling Systems," *Appl. Mech. Rev.*, **57**, 191-221 (2004).

[3] G. Hetsroni, A. Mosyak, E. Pogrebnyak, and L.P. Yarin, "Fluid flow in Micro-Channels," *International Journal of Heat and Mass Transfer*, **48,** 1982-1998 (2005).

[4] X.F. Peng, G.P. Peterson, and B.X. Wang, "Frictional Flow Characteristics of Water Flowing Through Rectangular Microchannels," *Experimental Heat Transfer* **7**, 249-265 (1994).

[5] B.R. Thompson, D. Maynes, and B.W. Webb, "Characterization of the Re-Entrant Developing Flow in a Microtube using MTV,"*Journal of Fluids Engineering,* **127** 1003-1012 (2005).

[6] R. Baviere, F. Ayela, S. Le Person, and M. Favre-Marinet "Experimental Characterization of Water Flow Through Smooth Rectangular Microchannels," *Physics of Fluids,* **17,** 098105 (2005).

[7] J. Judy, D. Maynes, B.W. Webb, "Characterization of Frictional Pressure Drop for Liquid Flows Through Microchannels," *International Journal of Heat and Mass Transfer*, **45,** pp. 3477-3489 (2002).

[8] D. Yu, R. Warrington, R. Barron, and T. Ameel, "Experimental and Theoretical Investigation of Fluid Flow and Heat Transfer in Microtubes," *Proceedings of the 1995 ASME/JSME Thermal Engineering Joint Conference,* Maui, Hawaii, 523-530 (1995).

[9] T. Onda, S. Shibuichi, N. Satoh, and K. Tsujii, "Super-Water-Repellent Fractal Surfaces," *Langmuir*, **12**(9), (1996).

[10] W. Chen, A. Y. Fadeev, M. C. Hsieh, D. Oner, J. Youngblood, and T. J. McCarthy, "Ultrahydrophobic and Ultralyophobic Surfaces: Some Comments and Examples," *Langmuir*, **15**, 3395-3399 (1999).

[11] W. Chen, A. Y. Fadeev, M. C. Hsieh, D. Oner, J. Youngblood, and J. T. McCarthy, "Ultrahydrophobic and Ultralyophobic Surfaces: Some Comments and Examples," *Laungmuir*, **15**, 3395-3399 (1999).

[12] J. Kim and C-J. Kim, "Nanostructured Surfaces for Dramatic Reduction of Flow Resistance in Droplet-Based Microfluidics," *Proceedings of the IEEE MEMS 2002 Conference,* Las Vegas, NV, 479-482 (2002).

[13] Z. Yoshimitsu, A. Nakajima, T. Watanabe, and K. Hashimoto, "Effect of Surface Structure on the Hydrophobicity and Sliding Behavior of Water Droplets," *Langmuir*, **18**, 5818-5822 (2002).

[15] D. Oner and T. J. McCarthy, "Ultrahydrophobic Surfaces. Effects of Topography Length Scales on Wettability," *Langmuir*, **16**, 7777-7782 (2000).

[16] J. Bico, U. Thiele, and D. Quere, "Wetting of Textured Surfaces," *Colloids and Surfaces A*, **206**, 41-46 (2002).

[17] A. Torkkeli, J. Saarilahti, A. Haara, H. Harma, T. Soukka, and P. Tolonen, "Electrostatic Transportaion of Water Droplets on Superhydrophobic Surfaces," *Proceedings of the IEEE MEMS 2001 Conference*, 475-578 (2001).

[18] T. N. Krupenkin, J. A. Taylor, T. M. Schneider, and S. Yang, "From Rolling Ball to Complete Wetting: The Dynamic Tuning of Liquids on Nanostructured Surfaces," *Langmuir*, **20**, 3824-3827 (2004).

[19] K. Watanabe, T. Takayama, S. Ogata, S. Isozaki, "Flow Between Two Coaxial Rotating Cylinders with a Highly Water-Repellent Wall," *AIChE Journal,* **49,** 1956 (2003)

[20] K. Watanabe, Y. Udagawa, and H. Udagawa, "Drag Reduction of Newtonion Fluid in a Circular Pipe with a Highly Water-Repellent Wall," *Journal of Fluid Mechanics*, **381**, 225-238 (1999).

[21] Y. Yong-Sheng, and W. Qing-Ding, "Experimental Study on Physical Mechanism of Drag Reduction of Hydrophobic materials in Laminar Flow," *Chinese Physics Letters*, **23**, 1634-1637 (2006).

[22] J. Ou, B. Perot, J. P. Rothstein, "Laminar Drag Reduction in Microchannels Using Ultrahydrophobic Surfaces," *Physics of Fluids*, **16**, 4635-4643 (2004).

[23] J. Ou and J. P. Rothstein "Direct velocity measurements of the flow past drag-reducing ultrahydrophobic surfaces," *Physics of Fluids* **17**, 103606 (2005).

[24] C. Chang-Hwan, U. Umberto, K. Joonwon, H. Chih-Ming, and K. Chang-Jin, "Effective Slip and Friction Reduction in Nanograted Superhydrophobic Microchannels," *Physics of Fluids*, **18**, 087105 (2006).

[25] J. R. Philip, "Flows Satisfying Mixed No-Slip and No-Shear Condition," *Journal of Applied Mathematics and Physics,* **23,** 353-371 (1972).

[26] E. Lauga and H. Stone, "Effective Slip in Pressure –Driven Stokes Flow," *Journal of Fluid Mechanics,* **489,** 55-77 (2003).

[27] M. Sbragaglia and A. Prosperetti, "A Note on the Effective Slip Properties for Microchannel Flows with Ultrahydrophobic Surfaces," *Physics of Fluids*, **19**, 043603 (2007).

[28] T. Salamon, W. Lee, T. Krupenkin, M. Hodes, P. Kolodner, R. Enright, and A. Salinger, "Numerical Simulation of Fluid Flow in Microchannels with Superhydrophobic Walls," *ASME International Mechanical Engineering Congress and Exposition*, IMECE2005-82641, (Orlando, 2005).

[29] J. Davies, D. Maynes, B. W. Webb, and B. Woolford, 2006, "Laminar Flow in a Microchannel with Super-Hydrophobic Walls Exhibiting Transverse Ribs," *Physics of Fluids*, **18**, pp. 087110 (2006).

[30] B. Woolford, K. Jeffs, D. Maynes, and B. W. Webb, "Laminar Fully-developed Flow in a Microchannel with Patterned Ultrahydrophobic Walls", *Proceeding of Summer Heat Transfer Conference*, HT2005-72726 (ASME, San Fransisco, 2005)

[31] D. Maynes, K. Jeffs, B. Woolford and B. W. Webb, "Laminar Flow in a Microchannel with Hydrophobic Surface Patterned Micro-ribs Oriented Parallel to the Flow Direction", *Physics of Fluid*, *In press* (2007).

[32] S. Gogte, P Vorobieff, R. Truesdell, A. Mammoli, F. van Swol, P. Shah, and C.J. Brinker, "Effective Slip on Textured Superhydrophobic Surfaces," *Physics of Fluids,* **17**, 051701 (2005).

[33] D. C. Tretheway and C. D. Meinhart, "Apparent fluid Slip at Hydrophobic Microchannel Walls," *Physics of Fluids*, **14**(3), L9-12 (2002).

[34] K. Chang-Jin, and C. Chang-Hwan, "Nano-Engineered Low-Friction Surface for Liquid Flow," Mechanical and Aerospace Engineering Department, University of California at Los Angeles.

[35] C. Chang-Hwan, K. Johan, A. Westin, K. Breuer, "Apparent Slip Flows in Hydrophilic and Hydrophobic Microchannels," *Physics of Fluids*, **15**, 2897-2902 (2003).

[36] C. Cottin-Bizonne, J. L. Barrat, L. Bocquet, and E. Charlaix, "Low-Friction Flows of Liquid at Nanopatterned Interfaces," *Nature Materials Letters*, **2**, 237-240 (2003).

[37] C. Bing-Yang, C. Min, and G. Zeng-Yuan, "Liquid Flow in Surface-Nanostructured Channels Studied by Molecular Dynamics Simulation," *Physical Review E*, **74**, 066311 (2006).

[38] F. Sahlin, S. B. Glavatskih, T. Almqvist, and R. Larsson, "Two-Dimensional CFD-Analysis of Micro-Patterned Surfaces in Hydrodynamic Lubrication," *Transactions of the ASME*, **127**, 96-102 (2005).

[39] C. Y. Wang, "Flow Over a Surface with Parallel Grooves," *Physics of Fluids*, **15**(5), 1114-1121 (2003).

[40] K. V. Sharp, and R. J. Adrian, "Transition from Laminar to Turbulent Flow in Liquid Filled Microtubes," *Experiments in Fluids,* **36,** 741-747 (2004).

[41] G. L. Morini, "Laminar-to-Turbulent Flow Transition in Microchannels," *Microscale Thermophysical Engineering*," **8**, 15-30 (2004).

[42] C. Rands, B.W. Webb, and D. Maynes, 2006, "Characterization of Transition to Turbulence in Microchannels", *Internation Journal of Heat and Mass Transfer,* **49**, 2924-2930 (2006).

[43] T. Min and J. Kim, "Effects of Hydrophobic Surface on Skin-Friction Drag," *Physics of Fluids*, **16**, L55-58 (2004).

[44] K. Fukagata, N. Kasagi, and P. Koumoutsakos, "A Theoretical Prediction of Friction Drag Reduction in Turbulent Flow by Superhydrophobic Surfaces," *Physics of Fluids*, **18**, 051703 (2006).

[45] C. Henoch, T. N. Krupenkin, P. Kolodner, J. A. Taylor, M. S. Hodes, A. M. Lyons, C. Peguero, and K. Breuer, "Turbulent Drag Reduction Using Superhydrophobic Surfaces," *AIAA Flow Control Conference*, AIAA2006-3192 (San Fransisco 2006).

[46] H. Blasius, "Das Ahnlichkeitsgesetz bei Reibungsvorgangen in Flussigkeiten", *Forschg. Arb. Ing.-Wes.*, No. 131, Berlin (1913).

[47] O. C. Jones, "An Improvement in the Calculation of Turbulent Friction in Rectangular Ducts", *J. Fluids Eng.* **98**, 173 (1976).

[48] G. S. Beavers, E. M. Sparrow, and J. R. Lloyd, "Low Reynolds Number Flow in Large Aspect Ratio Rectangular Ducts," *J. Basic Eng.*, **93**, 296-299 (1978).

[49] R. B. Dean, "Reynolds Number Dependence of Skin Friction and Other Bulk Flow Variable in Two-Dimensional Rectangular Duct Flow," *Journal of Fluids Engineering*, **100**, 215-223 (1978).

[50] D. C. Wilcox, "Comparison of Two-Equation Turbulence Models for Boundary Layers with Pressure Gradient," *AIAA Journal*, **31**, 1414-1421 (1993).

[51] F. R. Menter, "Two-Equation Eddy-Viscosity Turbulence Models for Engineering Applications," *AIAA Journal*, **32**, 1598-1605 (1994).

[52] F. M. White, *Viscous Fluid Flow 2nd ed*., McGraw-Hill, (1991).

Appendix A. U.D.F. Code for 1-D Vapor Cavity Model

```
#include "udf.h"

DEFINE_PROFILE(interface_shear, thread, index)
{
   real VISCOSITY_RATIO = 0.0181;
   real HEIGHT_RATIO = 5;
   real A[ND_ND];
   real sum = 0;
   real sum_A = 0;
   real u_bar;
   face_t f;


   begin_f_loop(f,thread)
      {
         F_AREA(A,f,thread);
         sum_A += NV_MAG(A);
         sum += F_T(f,thread)*NV_MAG(A);
      }
   end_f_loop(f,thread)

   u_bar = sum/sum_A;

   begin_f_loop(f,thread)
      {
         F_PROFILE(f,thread,index) = -
8*u_bar*HEIGHT_RATIO*VISCOSITY_RATIO;
      }
   end_f_loop(f,thread)
}
```

Appendix B. Analytical Solution of the 2-D Vapor Cavity

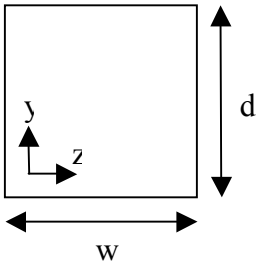

$$\frac{1}{\mu}\frac{dP}{dz} = \frac{\partial^2 u}{\partial y^2} + \frac{\partial^2 u}{\partial z^2}$$

Solution is in the form:

$$u(x,y) = u_1(x,y) + u_2(x,y)$$

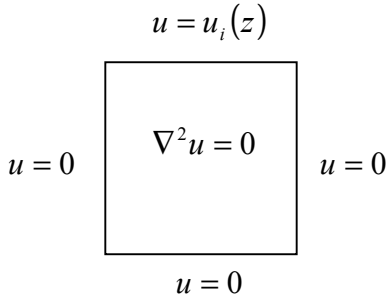

$$u_1(z,y) = \sum_{n=1}^{\infty} B_n \sin\left(\frac{n\pi}{w} z\right) \sinh\left(\frac{n\pi}{w} y\right)$$

$$B_n = \frac{2\int_0^w u_i(z) \sin\left(\frac{n\pi}{w} z\right) dz}{w \sinh\left(\frac{dn\pi}{w}\right)}$$

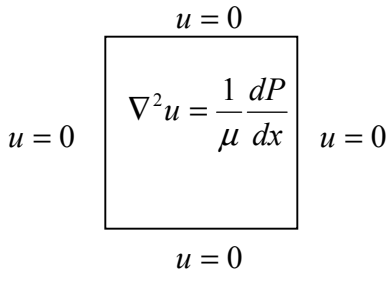

$$u_2(z,y) = \sum_{n=1}^{\infty}\sum_{m=1}^{\infty} A_{n,m} \sin\left(\frac{n\pi}{w} z\right) \sin\left(\frac{m\pi}{h} y\right)$$

$$A_{n,m} = -\left(\frac{1}{\mu_v}\left(\frac{dP}{dx}\right)_v\right) \frac{4(\cos(n\pi)-1)(\cos(m\pi)-1)}{\pi^4 nm\left[\frac{n^2}{w^2} + \frac{m^2}{d^2}\right]}$$

$\left(\frac{dP}{dx}\right)_v$ can be determined by applying the average velocity since

$$\bar{u} = \frac{1}{wd}\int_0^w \int_0^d u(z,y)dzdy = 0$$

Or for the current case

$$\bar{u} = \int_0^w \int_0^d u_1(z,y)dzdy + \int_0^w \int_0^d u_2(z,y)dzdy = 0$$

$$\bar{u} = \int_0^w \int_0^d \sum_{n=1}^{\infty} B_n \sin\left(\frac{n\pi}{w}z\right)\sinh\left(\frac{n\pi}{w}y\right)dzdy + \int_0^w \int_0^d \sum_{n=1}^{\infty}\sum_{m=1}^{\infty} A_{n,m} \sin\left(\frac{n\pi}{w}z\right)\sin\left(\frac{m\pi}{h}y\right)dzdy = 0$$

Evaluating the two double integrals separately:

1) $$\sum_{n=1}^{\infty} B_n \int_0^w \int_0^d \sin\left(\frac{n\pi}{w}z\right)\sinh\left(\frac{n\pi}{w}y\right)dzdy$$

$$\sum_{n=1}^{\infty} B_n \left[\frac{-w}{n\pi}\cos\left(\frac{n\pi}{w}z\right)\right]_0^w \left[\frac{w}{n\pi}\cosh\left(\frac{n\pi}{w}y\right)\right]_0^d$$

$$\sum_{n=1}^{\infty} -B_n \left(\frac{w}{n\pi}\right)^2 (\cos(n\pi)-1)\left(\cosh\left(\frac{dn\pi}{w}\right)-1\right)$$

$$\sum_{n=1}^{\infty}\frac{-2w\int_0^w u_i(z)\sin\left(\frac{n\pi}{w}z\right)dz}{(n\pi)^2\sinh\left(\frac{dn\pi}{w}\right)}\left(\cos(n\pi)-1\right)\left(\cosh\left(\frac{dn\pi}{w}\right)-1\right)$$

2) $$\sum_{n=1}^{\infty}\sum_{m=1}^{\infty}A_{n,m}\int_0^w\int_0^d\sin\left(\frac{n\pi}{w}z\right)\sin\left(\frac{m\pi}{h}y\right)dzdy$$

$$\sum_{n=1}^{\infty}\sum_{m=1}^{\infty}A_{n,m}\left[\frac{-w}{n\pi}\cos\left(\frac{n\pi}{w}z\right)\right]_0^w\left[\frac{-d}{m\pi}\cos\left(\frac{m\pi}{h}y\right)\right]_0^d$$

$$\sum_{n=1}^{\infty}\sum_{m=1}^{\infty}A_{n,m}\left(\frac{wd}{nm\pi^2}\right)\left(\cos(n\pi)-1\right)\left(\cos(m\pi)-1\right)$$

$$\sum_{n=1}^{\infty}\sum_{m=1}^{\infty}-\left(\frac{1}{\mu_v}\left(\frac{dP}{dx}\right)_v\right)\frac{4wd\left(\cos(n\pi)-1\right)^2\left(\cos(m\pi)-1\right)^2}{\pi^6(nm)^2\left[\frac{n^2}{w^2}+\frac{m^2}{d^2}\right]}$$

Thus

$$\bar{u}=\sum_{n=1}^{\infty}\frac{-2w\int_0^w u_i(z)\sin\left(\frac{n\pi}{w}z\right)dz}{(n\pi)^2\sinh\left(\frac{dn\pi}{w}\right)}\left(\cos(n\pi)-1\right)\left(\cosh\left(\frac{dn\pi}{w}\right)-1\right)$$

$$+\left(\frac{dP}{dx}\right)_v\sum_{n=1}^{\infty}\sum_{m=1}^{\infty}\frac{-4wd\left(\cos(n\pi)-1\right)^2\left(\cos(m\pi)-1\right)^2}{\mu\pi^6(nm)^2\left[\frac{n^2}{w^2}+\frac{m^2}{d^2}\right]}=0$$

Solving for $\left(\frac{dP}{dx}\right)_v$ gives:

$$\left(\frac{dP}{dx}\right)_v = \frac{\left[\sum_{n=1}^{\infty} \frac{-2w\int_0^w u_i(x)\sin\left(\frac{n\pi}{w}z\right)dz}{(n\pi)^2\sinh\left(\frac{dn\pi}{w}\right)}\left(\cos(n\pi)-1\right)\left(\cosh\left(\frac{dn\pi}{w}\right)-1\right)\right]}{\left[\sum_{n=1}^{\infty}\sum_{m=1}^{\infty}\frac{-4wd\left(\cos(n\pi)-1\right)^2\left(\cos(m\pi)-1\right)^2}{\mu_v\pi^6(nm)^2\left[\frac{n^2}{w^2}+\frac{m^2}{d^2}\right]}\right]}$$

$$\left(\frac{dP}{dz}\right)_v = -\left(\frac{\mu_v\pi^4}{2d}\right)\frac{\left[\sum_{n=1}^{\infty} \frac{-\int_0^w u_i(z)\sin\left(\frac{n\pi}{w}z\right)dz}{\sinh\left(\frac{dn\pi}{w}\right)}\left(\cos(n\pi)-1\right)\left(\cosh\left(\frac{dn\pi}{w}\right)-1\right)\right]}{\left[\sum_{n=1}^{\infty}\sum_{m=1}^{\infty}\frac{-\left(\cos(n\pi)-1\right)^2\left(\cos(m\pi)-1\right)^2}{m^2\left[\frac{n^2}{w^2}+\frac{m^2}{d^2}\right]}\right]}$$

DIMENSIONLESS FORM

$$Y = \frac{y}{D_h}; \qquad Z = \frac{z}{D_h}; \qquad U = \frac{u}{\left(-\left(\frac{dP}{dz}\right)_l \frac{D_h^2}{\mu_l}\right)}$$

$$U(Z,Y) = U_1(Z,Y) + U_2(Z,Y)$$

$$U_1(Z,Y) = \sum_{n=1}^{\infty} \frac{2\int_0^{W_m} U_i(Z)\sin\left(\frac{n\pi}{W_c}Z\right)dZ}{W_c \sinh\left(\frac{n\pi\delta_c}{W_c}\right)} \sin\left(\frac{n\pi}{W_c}Z\right)\sinh\left(\frac{n\pi}{W_c}Y\right)$$

$$U_2(Z,Y) = \sum_{n=1}^{\infty}\sum_{m=1}^{\infty} \frac{2(\cos(n\pi)-1)(\cos(m\pi)-1)}{nm\delta_c\left[\frac{n^2}{W_c{}^2} + \frac{m^2}{\delta_c{}^2}\right]} \sin\left(\frac{n\pi}{W_c}Z\right)\sin\left(\frac{m\pi}{\delta_c}Y\right)$$

$$* \frac{\left[\sum_{n=1}^{\infty} \frac{-\int_0^{W_m} U_i(Z)\sin\left(\frac{D_h n\pi}{w}Z\right)dZ}{\sinh\left(\frac{n\pi\delta_c}{W_c}\right)} (\cos(n\pi)-1)\left(\cosh\left(\frac{n\pi\delta_c}{W_c}\right)-1\right)\right]}{\left[\sum_{n=1}^{\infty}\sum_{m=1}^{\infty} \frac{-(\cos(n\pi)-1)^2(\cos(m\pi)-1)^2}{m^2\left[\frac{n^2}{W_c{}^2} + \frac{m^2}{\delta_c{}^2}\right]}\right]}$$

DIMENSIONLESS SHEAR STRESS

$$\tau = \mu \frac{du}{dy} \qquad \Rightarrow \qquad \frac{\mu_v \left(-\left(\frac{dP}{dx} \right)_l \frac{D_h^2}{\mu_l} \right)}{D_h} \frac{dU}{dY} \qquad \Rightarrow \qquad \left(\frac{\mu_l}{\mu_l} \right) \left(-\left(\frac{dP}{dx} \right)_l D_h \right) \frac{dU}{dY}$$

$$\Rightarrow \qquad T = \left(\frac{\mu_v}{\mu_l} \right) \left. \frac{dU}{dY} \right|_{Y=\delta_c} \qquad\qquad T_i(Z,Y) = T_1(Z,Y) + T_2(Z,Y)$$

$$T_1(Z,Y) = \left(\frac{\mu_v}{\mu_l} \right) \sum_{n=1}^{\infty} \frac{2n\pi \int_0^{W_c} U_i(Z) \sin\left(\frac{n\pi}{W_c} Z \right) dZ}{{W_c}^2 \sinh\left(\frac{n\pi\delta_c}{W_c} \right)} \cosh\left(\frac{n\pi\delta_c}{W_c} \right) \sin\left(\frac{n\pi}{W_c} Z \right)$$

$$T_2(Z,Y) = \sum_{n=1}^{\infty} \sum_{m=1}^{\infty} \frac{-2\pi(\cos(n\pi)-1)(\cos(m\pi)-1)}{n{\delta_c}^2 \left[\frac{n^2}{{W_c}^2} + \frac{m^2}{{\delta_c}^2} \right]} \cos(m\pi) \sin\left(\frac{n\pi}{W_c} Z \right)$$

$$* \frac{\left[\sum_{n=1}^{\infty} \frac{-\int_0^{W_c} U_i(Z) \sin\left(\frac{n\pi}{W_c} Z \right) dZ}{\sinh\left(\frac{n\pi\delta_c}{W_c} \right)} (\cos(n\pi)-1) \left(\cosh\left(\frac{n\pi\delta_c}{W_c} \right) - 1 \right) \right]}{\left[\sum_{n=1}^{\infty} \sum_{m=1}^{\infty} \frac{-(\cos(n\pi)-1)^2 (\cos(m\pi)-1)^2}{m^2 \left[\frac{n^2}{{W_c}^2} + \frac{m^2}{{\delta_c}^2} \right]} \right]}$$

Appendix C. U.D.F. Code for 2-D Vapor Cavity Model

```
#include "udf.h"

DEFINE_PROFILE(interface_shear, thread, index)
{
   real VISC_RATIO = 0.0181;  /*air viscosity/water viscosity*/
   real cH = 80;        /*H2O channel height*/
   real H_RATIO = 5;          /*channel/cavity heigth ratio*/
   real H_W_RATIO = 1;        /*channel height/cavity width*/
   real C_H_W_RATIO = 0.2;    /*cavity height/cavity width*/
   real CAVITY_HEIGHT = 16;
   real CAVITY_WIDTH = 80;
   real PI = 3.14159265;
   int NMAX=200;              /*Maximum number of terms for sums*/

   real V[200];
   real A[ND_ND];
   real x[ND_ND];
   real z=0;
   real dz=0;
   real T=0;
   real T1=0;
   real T2=0;
   real dP=0;
   real dP1=0;
   real dP2=0;
   real T1old=0;
   real T2old=0;
   real dP1old=0;
   real dP2old=0;
   real R=0;
   real iter=0;
   int icheck=0;
   double dcheck=0;
   face_t f;
   int n=0;
   int m=0;

   /*iter=N_ITER;
   printf("%f\n", iter);
   /*icheck=iter/25;
   dcheck=iter/25.0;
   if(dcheck-icheck!=0) break;*/

   for(n=1;n<NMAX+1;n++)
```

```
   {
      V[n]=0;
   }

   for(n=1; n<NMAX+1; n++)
   {
      begin_f_loop(f,thread)
      {
            F_AREA(A,f,thread);
            dz = NV_MAG(A);

            F_CENTROID(x,f,thread);
            z=x[0];

            V[n] += F_T(f,thread)*sin(2*H_W_RATIO*n*PI*z)*dz;
            /*printf("%f %f\n", V[n], n);*/

      }
      end_f_loop(f,thread)
      /*printf("%f\n", V[n]);*/
   }

   dP=0;
   dP1old=0;
   dP2old=0;
   for(n=1; n<NMAX+1; n++)
   {
      dP1old = dP1;
      dP1 = dP1old+((-V[n]*(cos(n*PI)-1)*(cosh(C_H_W_RATIO*n*PI)-1))
      /(n*n*sinh(C_H_W_RATIO*n*PI)));

      for(m=1; m<NMAX+1; m++)
      {
            dP2old = dP2;
            dP2 = dP2old+(-pow((cos(n*PI)-1),2)*pow((cos(m*PI)-1),2)

/(pow(n*m,2)*(pow(n/CAVITY_WIDTH,2)+pow(m/CAVITY_HEIGHT,2))));

            R=fabs(dP2-dP2old);
            icheck=m/2;
            dcheck=m/2.0;
            if(dcheck-icheck!=0 && R<0.0001) break;
            /*printf("%f\n", dP2);*/
      }
      R=fabs(dP1-dP1old);
      icheck=n/2;
      dcheck=n/2.0;
      if(dcheck-icheck!=0 && R<0.0000001) break;
      /*printf("%f\n", dP1);*/
   }
   dP = dP1/dP2;
   /*printf("\n%f\n", dP);*/

   T=0;
   T1old=0;
   T2old=0;
   begin_f_loop(f,thread)
```

```
   {
      F_CENTROID(x,f,thread);
      z=x[0];

      T1=0;
      T2=0;
      for(n=1; n<NMAX+1; n++)
      {
            T1old = T1;
            T1 = T1old+(pow(H_W_RATIO,2)*8*n*PI*V[n]
                 *sin(2*H_W_RATIO*n*PI*z)*cosh(C_H_W_RATIO*n*PI)
                 /sinh(C_H_W_RATIO*n*PI));

            for(m=1; m<NMAX+1; m++)
            {
                  T2old = T2;
                  T2 = T2old+(pow(H_RATIO,2)*dP*8*PI*(cos(n*PI)-
1)*(cos(m*PI)-1)

*sin(2*H_W_RATIO*n*PI*z)*cos(m*PI)/(n*(pow(n/CAVITY_WIDTH,2)
                       +pow(m/CAVITY_HEIGHT,2))));

                  R=fabs(T2-T2old);
                  icheck=m/2;
                  dcheck=m/2.0;
                  if(dcheck-icheck!=0 && R<0.0000001) break;
                  /*printf("%f\n", T2);*/
            }
            R=fabs(T1-T1old);
            if(R<0.0000001) break;
            /*printf("%f\n", T1);*/
        }
        T = -VISC_RATIO*(T1+T2);
        /*printf("\n%f\n", T);*/

        F_PROFILE(f,thread,index) = T;
    }
    end_f_loop(f,thread)
}
```

Appendix D. Matlab™ Code for Vapor Cavity Velocity Field

```
%Kevin Jeffs
%Thesis: vapor cavity

%clear previous data
clc
close all
clear
format compact

[Z ui] = textread('InterfaceVelocityData.txt');
nZ=length(Z);
for i=1:nZ-1
    dZ(i)=Z(i+1)-Z(i);
    Ui(i)=(ui(i+1)+ui(i))/2;
end

Wm=1.0;     %relative module width
Fc=0.96875;    %cavity fraction
Wc=Fc*Wm;   %demensionless cavity width
dc=0.4;     %dimensionless cavity depth
Dh=160;     %hydraulic diameter
Zcl=Wc/2;
Yhat=0:0.001:dc;
nY=length(Yhat);
n=100;
m=100;

%an
for i=1:n
    for j=1:nZ-1
        int(j)=Ui(j)*sin(i*pi()*Z(j)/Wc)*dZ(j);
    end
    an(i)=sum(int)/sinh(i*pi()*dc/Wc);
end

%Anm and Bnm
for i=1:n
    for j=1:m
        Anm(i,j)=(cos(i*pi())-1)*(cos(j*pi())-1)/(i*j);
        Bnm(i,j)=(i/Wc)^2+(j/dc)^2;
    end
end
```

```
%Phi
for i=1:n
    temp1(i)=an(i)/i^2*(cos(i*pi())-1)*(cosh(i*pi()*dc/Wc)-1);
    for j=1:m
        temp2(i,j)=Anm(i,j)^2/Bnm(i,j);
    end
end
phi=sum(temp1)/sum(sum(temp2));

%Velocity Field
for k=1:nZ
    for l=1:nY
        for i=1:n
            temp1(i)=an(i)*sin(i*pi()*Z(k)/Wc)*sinh(i*pi()*Yhat(l)/Wc);
            for j=1:m
               temp2(i,j)=Anm(i,j)/Bnm(i,j)*sin(i*pi()*Z(k)/Wc)
                  *sin(j*pi()*Yhat(l)/dc);
            end
        end
        temp3(k,l)=sum(temp1);
        temp4(k,l)=sum(sum(temp2));
    end
end
for k=1:nZ
    for l=1:nY
        U(k,l)=(2/Wc)*temp3(k,l)+(2*phi/dc)*temp4(k,l);
    end
end

%Velocity Field at Cavity Center Line (Zcl)
for l=1:nY
    for i=1:n
        temp1(i)=an(i)*sin(i*pi()*Zcl/Wc)*sinh(i*pi()*Yhat(l)/Wc);
        for j=1:m

temp2(i,j)=Anm(i,j)/Bnm(i,j)*sin(i*pi()*Zcl/Wc)*sin(j*pi()*Yhat(l)/dc);
        end
    end
    temp3(l)=sum(temp1);
    temp4(l)=sum(sum(temp2));
end
for l=1:nY
    Ucl(l)=(2/Wc)*temp3(l)+(2*phi/dc)*temp4(l);
end

figure(1)
plot(Ucl,Yhat)
title('Vapor Cavity Centerline Velocity Profile')
xlabel('U_v')
ylabel('Y')
```